Rayleigh-Taylor Instability of a Thin Elastic Solid Loaded by a Shock Wave

Dan-Cornelius Savu



Department of Mechanical Engineering McGill University, Montreal

April 2024

A thesis submitted to McGill University in partial fulfilment of the requirements of the degree of

Master of Science

This thesis is dedicated to my Balkan bro	ther from another mother.	

Declaration

I hereby declare that except where specific reference is made to the work of others, the contents of this thesis are original and have not been submitted in whole or in part for consideration for any other degree or qualification in this, or any other university. This thesis is my own work and contains nothing which is the outcome of work done in collaboration with others, except as specified in the text and Acknowledgements.

Dan-Cornelius Savu Montreal April 2024

Abstract

Growth of instability in a thin elastic solid accelerated by a gasdynamic shock tube is studied experimentally. Elastomers of different thicknesses, initial perturbation wavelengths, and initial perturbation amplitudes are examined—the initial perturbations are sinusoidal. Elastomer materials are used because of their hyperelasticity and very low elastic shear moduli, properties which facilitate examining the phenomenon of interest in a laboratory-scale, low-pressure shock tube. The samples are lightly supported in the shock tube test section to avoid the influence of boundary effects. The gas shock reflects off the sample, causing it to accelerate due to the reflected shock pressure. The dynamics of the sample is recorded using high-speed videography and photonic Doppler velocimetry (PDV) with the PDV configuration tracking the velocity of individual perturbation peaks and troughs of the sample free surface. The experimental results are compared against analytical Rayleigh-Taylor stability boundaries and amplitude growth rates found in the literature. Agreement between experiments and theory is found in that the samples that are predicted by theory to be unstable do experimentally display large perturbation amplitude growth while the samples predicted by theory to be stable experimentally display no significant perturbation amplitude growth.

Sommaire

La croissance de l'instabilité d'un solide élastique mince accéléré par une onde de choc gazeux fut étudiée de façon expérimentale. Des élastomères de modules de rigidité, d'épaisseurs et de perturbations initiales différentes ont été étudiés. Les perturbations initiales furent sinusoïdales et les échantillons élastomériques furent créés à l'aide d'un procédé de coulage faisant usage de moules imprimés en 3D. Les échantillons ont été légèrement soutenus à la fin de l'enceinte avale d'un tube à choc afin de minimiser les effets de bords durant le dénouement des expérimentations. Immédiatement suivant l'impact entre l'échantillon étudié et l'onde de choc gazeux produite par le tube à choc, la production d'une différence de pression à travers l'élastomère permet l'accélération quasi constante de ce dernier pour une durée de temps d'un peu moins d'une milliseconde. L'évolution des perturbations inscrites dans chaque échantillon fut enregistrée à l'aide d'une caméra haute vitesse et la vélocité des crêtes et des creux centraux de chaque échantillon fut mesurée en utilisant la vélocimétrie Doppler photonique. Les résultats expérimentaux ont été comparés avec la théorie de l'instabilité de Rayleigh-Taylor. Les échantillons que la théorie de Rayleigh-Taylor prédisait comme étant instables ont tous démontré des taux de croissance des perturbations significatifs. Les échantillons que la théorie de Rayleigh-Taylor prédisait comme étant stables, c'est-à-dire comme n'ayant pas de taux de croissance des perturbations, ont tous été démontrés stables de façon expérimentale.

Acknowledgements

Although front authored by a single man, this thesis could not have seen the light of day without the help, support, and insight of many.

Chief amongst the supporters stands my thesis advisor, Professor Andrew J. Higgins who provided me throughout my academic journey with an honest mentor-student relationship both in and out of the laboratory. Thanks to him my trek through graduate school was a genuine apprenticeship filled with discoveries and learning experiences, experiences which in turn have equipped me with a robust set of technical, ethical, and even administrative competences that are sure to be of great use throughout the remainder of my life. Thank you Professor for helping little ol' me stretch my horizon beyond the narrow scope of my tenderfoot gaze.

Gratitude is also extended to Professor Jason Loiseau and Professor Oren Petel for their useful input with regards to all manners PDV. Lemuel Santos of General Fusion Inc. is also thanked for assistance with the PDV data processing. Thanks and recognition is likewise forwarded to Abdul Rehman Khan, Saad Kureshi, Alexandre Leboucher, and Yusi Wan for the design and fabrication of the shock tube apparatus used throughout this thesis. Sebastian Rodriguez Rosero is thanked for his work on the diaphragm section of the shock tube which helped facilitate the operation of the device. The work of Hansen Liu during the early stages of this investigation is also acknowledged and much appreciated.

I find myself indebted to Léa Bernard, Joshua Campbell, and Paolo Scaini for their assistance in the laboratory. Ms. Bernard, your relentless optimism and unapologetic directness are what helped sustain my enthusiasm when laboratory days seemed grey. Please never let go of these singularities of yours. I would also like to thank my out-of-laboratory colleagues Khalil Alhandawi, Caileigh Bates, Dylan Caverly, Purui Chen, Gabriel Dubé, Xavier Duchesne, Emmanuel Duplay, Anushka Goyal, John Kokkalis, Mathias N. Larrouturou, Leah

Lavoie, Jana Mouchaimech, Siera Riel, and Arnab Sinha. The chatter, banter, blather, and jabber amongst brothers and sisters in arms may reduce productivity in the here and now, but those remain the fuels that help a soul go the mile.

Works such as the ones undertaken in graduate school require money. I certainly am grateful and feel privileged for the financial support that was provided to me by the Natural Sciences and Engineering Research Council of Canada (NSERC) Discovery Grant "Dynamic Materials Testing for Ultrahigh-Speed Spaceflight," the McGill Summer Undergraduate Research in Engineering program, and Fonds de Recherche du Québec Nature et Technologies (FRQNT).

On a final note of gratitude, it must be mentioned that my undertaking of a graduate degree was more than a little surprising. Only a few decades ago, very few of my family members could barely even dream of attending university much less graduate school. This opportunity and privilege came to me through the sacrifice of my loving parents who crossed an ocean in hopes of providing a better future for the later generations. Thank you, father. Thank you, mother.

Contents

1	Introduction	1
2	2.2.1 Shock Tube Theory	7 12 12 15
3	Manufacturing the Solid Samples	18 20 22 25
4	Shock Loading of Sinusoidally Perturbed Ecoflex 00-30 Samples Theoretical and Experimental Growth Rates Shock Loading Flat Ecoflex 00-30 Samples Shock Loading Sinusoidally Perturbed Stiff Samples	30 34 35 38 41
5	5.1 Summary	45 45 46
Re	erences	47
\mathbf{A}	A.1 Derivation of the Dispersion Relation for RTI in an Elastic Solid	60 60 65 65

Contents	$\mathbf{v}^{\mathbf{j}}$

В	Additional Detailing of the Experimental Methods	72
	B.1 Procedure for the Casting of Elastic Solid Samples	72
	B.2 The PDV Heterodyne Principle	74
	B.3 The Detailed Schematic of the PDV Box	78

List of Figures

1.1	Schematic of the evolution of an RTI unstable, sinusoidally perturbed interface between a heavy fluid laying atop a lighter fluid: (a)–(b) linear growth of the interface amplitude; (b)–(c) nonlinear interface amplitude growth featuring the onset of bubble and spike formation; (c)–(d) onset of turbulent mixing	
1.2	between the two fluid layers	5
2.1	Plots of the RTI stability boundary in the λ - h space for different input parameters: (a) varying the driving pressure difference across the elastic solid;	4.0
2.2	(b) varying the elastic shear modulus of the solid	10
2.3	Plot of the RTI stability boundary in the Δp - h space alongside contour plots of the exponential growth rate, γ in the unstable region. This stability map is produced for $\lambda = 25 \mathrm{mm}$ and $G = 27 \mathrm{kPa}$.	10
2.4	The various gas states 1–5 in an open-ended shock tube	14
2.5	One-dimensional expansion of the gas driving the elastic solid immediately	
	after shock reflection	15
3.1	Top-view schematic of the experimental setup. The high-speed camera recorded a top view of the experiment through the use of a mirror positioned above the	
2.0	elastic solid sample	19
3.2 3.3	Ecoflex 00-30 samples alongside 3D printed molds	$\frac{20}{22}$
3.4	Theoretical shock tube M_s vs p_4 (a) and p_5 vs p_4 (b) plots for helium (dashed)	44
	and shop air (solid) as the driving gases	23

List of Figures viii

3.5	Image capture of pressure data recorded by the Siglent SDS1104X-E oscilloscope following a $p_4 = 42$ psig shot with helium in the driver. The yellow and purple traces represent the data acquired by the first and second pressure transducers, respectively—the first pressure transducer is the first sensor to	
	encounter the shock wave	24
3.6	Schematic of the PDV homodyne setup contained within the McGill PDV box. The left image is a picture of the McGill PDV apparatus including the	
	LeCroy high-bandwidth oscilloscope and the NP Photonics input laser	26
3.7	The sliding window FFT procedure for PDV data analysis	29
4.1	Shock loading of a 1.2-mm-thick Ecoflex 00-30 sample with $\lambda = 25 \text{mm}$ and $a_0 = 0.02\lambda$: (a) provides an enlarged and labeled view of the first snapshot, (b)–(e) show snapshots of the experiment at labeled times, and (f) shows the	
	amplitude growth of the sample obtained using PDV	31
4.2	Shock loading of a 1.2-mm-thick Ecoflex 00-30 sample with $\lambda = 25 \text{mm}$ and $\xi_0 = 0.10\lambda$: (a)–(d) show snapshots of the experiment at labeled times and	
	(e) shows the amplitude growth of the sample obtained using PDV	32
4.3	Shock loading of a 3.1-mm-thick Ecoflex 00-30 sample with $\lambda=25\mathrm{mm}$ and	
	$\xi_0 = 0.02\lambda$: (a)-(d) show snapshots of the experiment at labeled times and	
	(e) shows the amplitude growth of the sample obtained using PDV	33
4.4	Shock loading of a 6.1-mm-thick Ecoflex 00-30 sample with $\lambda = 25 \text{mm}$ and	
	$\xi_0 = 0.10\lambda$: (a)-(d) show snapshots of the experiment at labeled times and	
	(e) shows the amplitude growth of the sample obtained using PDV	33
4.5	Comparison between the curve-fitted experimental growth rate of the 1.2-mm-thi	.ck
	Ecoflex 00-30 sample with $\lambda = 25 \text{mm}$ and $\xi_0 = 0.02 \lambda$ and the theoretical	
	growth of the same sample predicted by RTI	34
4.6	Shock loading of a flat (i.e., no imposed perturbations) 1.7-mm-thick Ecoflex	
	00-30 sample: (a) shows the fiducial ruler used to allow for the calibration of	
	the image pixels; (b)–(e) show snapshots of the experiment at labeled times;	
	(f) plots the theoretical 1D velocity history of this sample alongside the experi-	
	mental velocity history of the sample obtained via PDV; and (g) shows the the-	
	oretical growth rate of the sample as a function of perturbation wavelength—	
	the wavelength for which theory predicts a maximum growth rate is equal to	
	2.10 mm	36
4.7	Shock loading of a flat (i.e., no imposed perturbations) 3.8-mm-thick Ecoflex	
	00-30 sample: (a)-(d) show snapshots of the experiment at labeled times	
	and (e) plots the theoretical 1D velocity history of this sample alongside the	
	experimental velocity history of the sample obtained via PDV	37

List of Figures ix

4.8	Shock loading of a flat (i.e., no imposed perturbations) 6.8-mm-thick Ecoflex	
	00-30 sample: (a)-(d) show snapshots of the experiment at labeled times	
	and (e) plots the theoretical 1D velocity history of this sample alongside the	
	experimental velocity history of the sample obtained via PDV	38
4.9	Shock loading of a 6.2-mm-thick Solaris sample with $\lambda = 12\mathrm{mm}$ and $\xi_0 =$	
	0.10λ : (a)-(d) show snapshots of the experiment at labeled times	39
4.10	Shock loading of a 6.3-mm-thick Sylgard 184 sample with $\lambda = 12\mathrm{mm}$ and	
	$\xi_0 = 0.10\lambda$: (a)-(d) show snapshots of the experiment at labeled times	40
4.11	Shock loading of a 6.4-mm-thick Vytaflex60 sample with $\lambda = 12\mathrm{mm}$ and	
	$\xi_0 = 0.10\lambda$: (a)-(d) show snapshots of the experiment at labeled times	40
4.12	Plot of the experimental data points described in this thesis on their corre-	
	sponding RTI stability map in the Δp -h space: (a) plot of the Ecoflex 00-30	
	data points; (b) plot of the Solaris data point; (c) plot of the Sylgard 184 data	
	point; and (d) plot of the Vytaflex 60 data point	41
112	Buckling stability boundaries plotted using different $\eta = \xi_0/\lambda$ values alongside	11
4.10	the RTI stability boundary for Ecoflex 00-30 with $\lambda = 12 \mathrm{mm}$	42
	the RTI stability boundary for Econex 00-50 with $\lambda = 12$ mm	42
A.1	Schematic of a normal shock wave	65
A.2	A normal shock wave in a laboratory-fixed reference frame (a) and in a shock-	
	fixed frame (b)	68
A.3	A reflected shock wave in a laboratory-fixed reference frame (a) and in a	00
11.0	shock-fixed frame (b)	70
	Shock-hacd frame (b)	10
B.1	The basic PDV heterodyne principle	75
B.2	A detailed schematic (b) of the layout of the photonic components found	
	within the McGill PDV box (a)	78
	\ /	

List of Tables

B.1 Target velocities and beat frequencies for different reference laser wavelengths. 77

Chapter 1

Introduction

Rayleigh-Taylor instability (RTI) is a theory of continuum mechanics that is concerned with the stability at the interface between two or more media of different densities. The classical scenario of a heavier fluid resting on top of a lighter fluid in a gravitational field was first theoretically studied by Lord Rayleigh in 1883 [1] with Benjamin Franklin having apparently made remarks in a letter dated 1762 about the period of oscillation of surface waves at oilwater and water-air interfaces [2]. Nearly a century later, in 1950, Sir Geoffrey Taylor was the first to realize that the classic scenario of a heavy fluid on top of a light fluid was equivalent to that of a light fluid accelerating the heavier fluid [3]. Taylor's seminal paper was followed by the first experimental investigation of the phenomenon produced by both Lewis and Taylor where the experimentally measured instability growth rate agreed remarkably well with the growth rates predicted by theory [4].

The experimental work of Lewis and Taylor demonstrated the evolution of an unstable water-air interface that is now characterized by four stages. Stage 1 occurs when the interface between the two fluids is slightly perturbed from a perfectly flat geometry. This stage is theoretically analyzed using linear perturbation theory where a sinusoidal interfacial perturbation is studied. The evolution of the perturbation amplitude at this stage follows an exponential trend until it equals about 0.1 to 0.4λ , where λ is the initial perturbation wavelength. Stage 2 is characterized by the nonlinear growth of the perturbation, a growth that is now heavily influenced by the density ratio of the two fluids often written out as the nondimensional Atwood number, At. This stage typically lasts until the amplitude of the perturbation has grown to be on the order of λ . Stage 3, where nonlinear interactions

between perturbations of different frequencies occurs, sees the debut of bubble and spikes formations at the interface between the two fluids. Stage 4, the final stage, produces the turbulent mixing of the two original layers through the breakup of the bubbles and spikes structures formed during Stage 3. Figure 1.1 displays the evolution of an RTI unstable interface between two fluids of different densities.

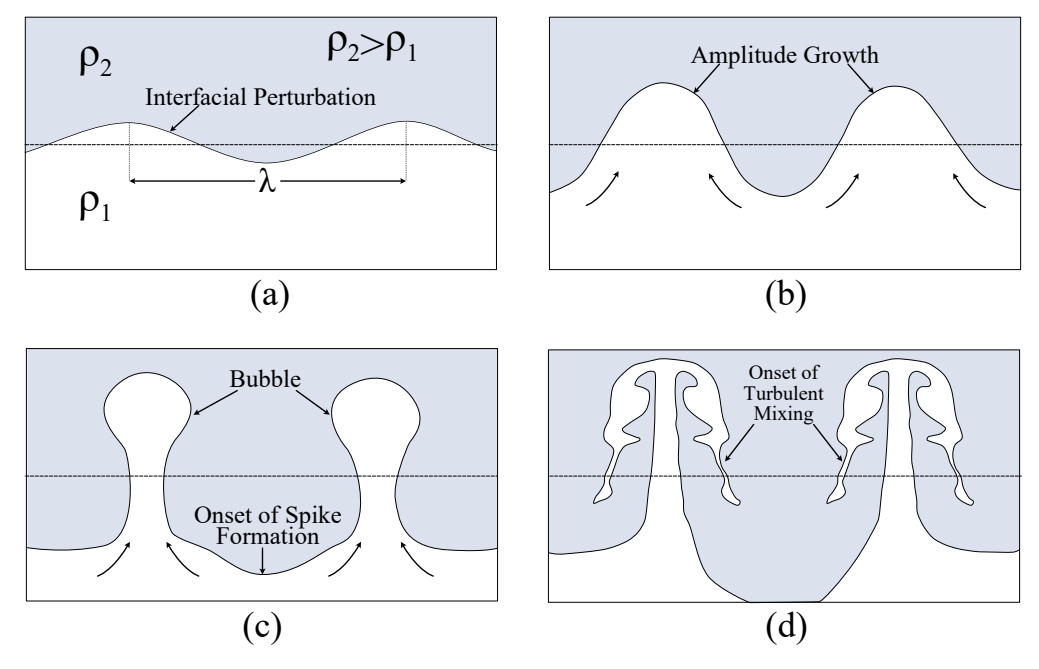


Figure 1.1: Schematic of the evolution of an RTI unstable, sinusoidally perturbed interface between a heavy fluid laying atop a lighter fluid: (a)–(b) linear growth of the interface amplitude; (b)–(c) nonlinear interface amplitude growth featuring the onset of bubble and spike formation; (c)–(d) onset of turbulent mixing between the two fluid layers.

Although the first theoretical studies where undertaken for the inviscid, incompressible scenario with constant acceleration, subsequent theoretical studies of the first, linear stage were done that further generalized the original models by including, for instance, the effect of surface tension and viscosity [5–8], compressibility [9, 10], non-uniform acceleration [11], finite (i.e., non-infinitesimal) perturbation amplitudes [12], magnetic fields [13], and density gradients [14]. The linear model was also extended to interfaces of spherical geometry [15–17]. In a series of studies, Mikaelian also theoretically investigated RTI in stratified media ranging from 3 to an arbitrary number of layers [18–22]. The first reviews of RTI theory were

produced by Chandrasekhar [23] and by Birkhoff [24] with the former primarily focusing on the linear theory while the later also discussing nonlinear solutions.

The modeling of the nonlinear stages of RTI has also been undertaken, with Chang providing the first higher-order (third order, in his case) perturbation expansion [12]. This first attempt at nonlinear theory was subsequently iterated upon by Kiang [25] and Rajappa [26] using singular perturbation methods, and by Nayfeh using the method of multiple time scales [27]. Ott provided the first exact, closed-form nonlinear solution that was valid up to a certain time t^* describing initial sinusoidal perturbations that eventually evolved into a cycloid [28]. All of these nonlinear studies concluded that the evolution of the interface of interest is dependent not only on its initial perturbation wavelength, but also on its initial perturbation amplitude, a dependency not typically found in linear RTI theory. Part of RTI nonlinear theory is also concerned with the analysis of spike and bubble formation. A notable first attempt at modeling RTI bubble dynamics was made by Fermi in which he modeled the initial perturbation as a square wave in the limit where the interfacing fluids are incompressible and have an infinite density ratio [29]. The resulting nonlinear ordinary differential equations (ODEs) yielded predictions for the speed of the evolution of the spikes that were approximately in agreement with experiment, but the predicted motion of the bubble was not in agreement with experiment. Crowley [30] and later Baker and Freeman [31] further iterated upon Fermi's model devising uncoupled ODEs that provide predictions for the motion of the tip of the spike and bubble that better agree with past experimental investigations. Further theoretical investigations into bubble rising dynamics were performed by Davies and Taylor [32] and Layzer [33] who considered the steady state motion of cylindrically symmetric bubbles. Birkhoff and Carter [34] and Garabedian [35] have also formulated rigorous conformal mapping theories of plane bubbles rising between parallel walls.

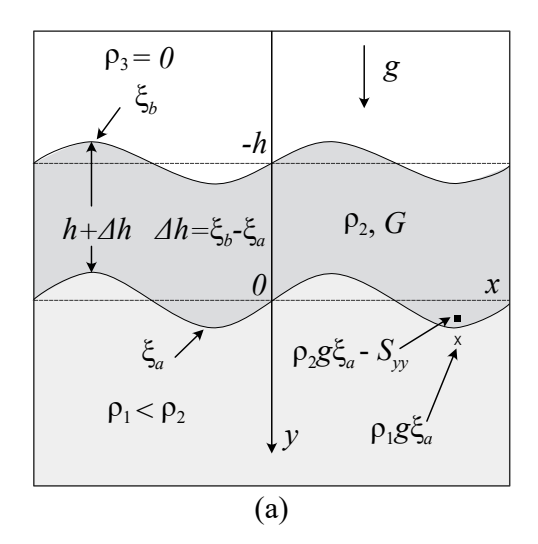
A complete review of the theoretical, numerical, and experimental aspects of Rayleigh-Taylor instability in solely fluid media is beyond the scope of this thesis. The reader is invited to peruse the first published reviews of RTI in fluids by Sharp (1984) [36] and Kull (1991) [37]. For a more up-to-date review of the subject, see the recent (2017) two-part publication by Zhou [38, 39].

Rayliegh-Taylor instability is not confined to the study of interfaces between solely fluids, however. Miles was the first to study RTI in an elastic-plastic solid being accelerated by

a lighter gas using an energy method [40]. White [41] and Ducker [42, 43] subsequently produced theoretical RTI models for elastic-plastic (EP) solids using one-degree-of-freedom energy approaches. A more general, Lagrangian-based, n-degree-of-freedom energy approach was employed to study RTI in a continuous medium of an arbitrary constitutive law by Dienes [44]. Robinson and Swegel generated several RTI theoretical models for elastic-plastic solids using an approximate modal technique (also a one-degree-of-freedom energy model) which they compared to their own numerical simulations of RTI in elastic-plastic solids [45, 46]. Ruden and Bell further iterated upon the models of White and Robinson and Swegel by assuming global energy conservation based on the Prandtl-Reuss equations of elastic-plastic flow [47]. For a succinct summary of the first theoretical inquiries into the problem of RTI in elastic-plastic solids, see the 2005 review paper by Terrones [48]. Unfortunately, likely in part due to modeling oversimplification, none of these energy-based theoretical analyses of the RTI problem in EP solids provided significant agreement with experimental investigations in the area (see immediately below for RTI experiments in solids). In an attempt to generate better agreement between theory and experiment, a series of progressively more complex theoretical studies were done by Piriz et al. for the case of RTI in EP solids by using a conservation of mass and momentum approach instead [49–58] with some of the latter inquiries also studying the effects of viscosity [52, 53], magnetic fields [54, 56], and the formation of spikes and bubbles [58]. Sun et al. also theoretically considered Rayleigh-Taylor instability in solids of spherical [59] and cylindrical [60] geometries. More recently, the theoretical analysis of RTI in viscoelastic solids has also been undertaken [61, 62].

Despite the abundance of theoretical studies, experimental investigations of RTI in solids have historically been comparatively scarce, although there has been a resurgence of interest in this area of research. Rayleigh-Taylor instability in solids has proven to be of relevance in the study of several natural phenomena such as in the geodynamics of the intra-plate deformation of the continental lithosphere [63–66] and in the production of gamma-ray bursts following the accretion of neutron stars [67–69]. The first experimental studies of RTI in solids were performed by Barnes et al. who conducted a series of experiments investigating RTI in sinusoidally perturbed aluminum flat plates accelerated by expanding detonation products [70, 71]. Rayleigh-Taylor instability has also been studied in gelatin of various geometries (planar layer, ring, wedge, etc.) accelerated by pulsed gas pressures [72]. Dimonte et al. investigated RTI in yogurt accelerated by pressurized nitrogen, considering

both two-dimensional (2D) and three-dimensional (3D) perturbations [73]. Polavarapu et al. performed similar experiments in mayonnaise, and, like Dimonte et al., found that 3D perturbations were more stable than 2D perturbations [74]. Rayleigh-Taylor instability has been used of late to experimentally study the mechanical properties of solids subjected to high strain rates in the context of high energy density physics. From the observed RTI growth rates, material properties under conditions of high strain have been inferred in aluminum [75, 76], in copper single crystals [77], in phase transitioning iron [77, 78], in polycrystalline vanadium [76, 79–81], and in tantalum [82, 83] amongst other metals, with some of these studies being performed in part in order to mitigate interfacial instabilities found in inertial confinement fusion capsule implosions [77, 83]. A series of theoretical [84–88] and experimental [84, 86, 87, 89] investigations into the Rayleigh-Taylor instability growth rates of confined soft gels deforming under their own weight have also been undertaken of recent. For instance, hypergravitational Rayleigh-Taylor instability has been studied in hydrogels using a centrifuge setup, with the RTI unstable samples gradually evolving from their initial flat state into a buckled state displaying structured cuvette patterns [89].



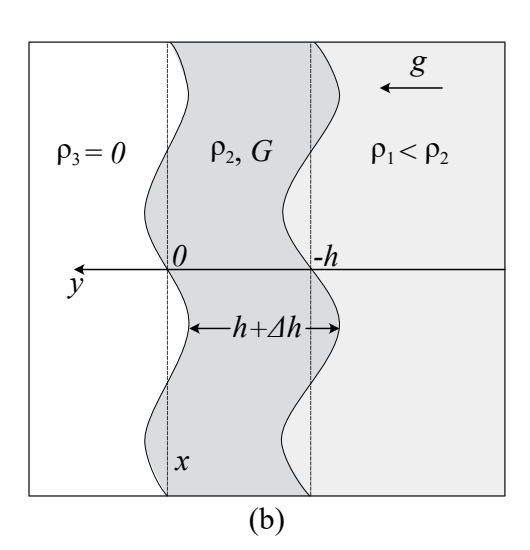


Figure 1.2: Schematic of the RTI problem in an elastic solid of finite thickness with a free surface: (a) the problem as studied in the literature [90–92] with the elastic solid laying atop a lighter fluid in a gravitational field; (b) the equivalent problem of a lighter fluid accelerating a solid of finite thickness—this is the problem most directly experimentally investigated throughout this thesis. Image (a) was adapted from [92] with permission.

While most of these studies have been concerned with the evolution of interfacial instabilities in elastic-plastic materials, theoretical treatments of RTI can be found in the literature that are concerned with instability growth rates in unconfined solids that undergo purely elastic deformation [90–92]. The objective of the present study is the experimental investigation of RTI in just such a scenario where a thin solid with a free surface is accelerated by a lighter medium and only deforms elastically following its initial loading (see Fig. 1.2). To this end, elastomer samples were accelerated using a gasdynamic shock tube. Sinusoidal perturbations were imposed onto the elastomer samples to simulate the presence of interfacial perturbations between the accelerating gas and the accelerated solid, and the data acquisition was performed using high-speed videography and photonic Doppler velocimetry. The evolution of the initial perturbations imposed onto the samples is then compared to the RTI formalism.

Chapter 2

Theoretical Considerations

This chapter discusses the theoretical background supporting the experiments described in this thesis. The first part of this chapter is concerned with the Rayleigh-Taylor instability theory for elastic solids that is experimentally being investigated, while the second part of this chapter describes the gasdynamics theory behind the workings of the shock tube device used to accelerate the elastic solids studied in this thesis. As the experiments in this thesis chiefly pertain to RTI in elastic solids and not to RTI in fluid/fluid interfaces, no extensive discussion of the classic RTI scenario in fluids is provided in this thesis. The reader is redirected to a relatively beginner-friendly presentation of RTI in fluids by Piriz et al. published in the American Journal of Physics [93] which also discusses the effects of surface tension and viscosity upon the stability of a fluid/fluid perturbed interface.

2.1 Rayleigh-Taylor Instability for Elastic Solids

The Raleigh-Taylor instability formalism predicts that, when a light gas medium accelerates a nearly flat solid, any perturbations away from a perfectly flat interface between the light gas and the solid may rapidly grow in size. In particular, assuming the interfacial perturbations to be sinusoidal in nature with a known initial amplitude, ξ_0 , and a known initial wavelength, $\lambda = 2\pi/k$ where k is the angular wavenumber (refer to Fig. 1.2 found at the end of the introductory chapter), the initial stage of the evolution of the perturbation amplitude can

be described by an exponential trend:

$$\xi(t) \propto \xi_0 e^{\gamma t} \sin kx,$$
 (2.1)

where γ , the growth rate of the perturbation amplitude may be either real or complex. In the case of a light gas accelerating an elastic solid of finite thickness, h, the perturbation growth rate can be computed by solving the following dispersion relation [90–92]:

$$\left(\frac{G}{\rho g}\right)^{8} \left\{ \left(\frac{8\pi^{2}}{\lambda^{2}} + \frac{\rho \gamma^{2}}{G}\right)^{4} + \frac{1024\pi^{6}}{\lambda^{6}} \left(\frac{4\pi^{2}}{\lambda^{2}} + \frac{\rho \gamma^{2}}{G}\right) - \left(\frac{4\pi}{\lambda}\right)^{3} \sqrt{\frac{4\pi^{2}}{\lambda^{2}} + \frac{\rho \gamma^{2}}{G}} \left(\frac{8\pi^{2}}{\lambda^{2}} + \frac{\rho \gamma^{2}}{G}\right)^{2} \left[\coth\left(\frac{2\pi h}{\lambda}\right) \coth\left(\sqrt{\frac{4\pi^{2}}{\lambda^{2}} + \frac{\rho \gamma^{2}}{G}}h\right) - \operatorname{csch}\left(\frac{2\pi h}{\lambda}\right) \operatorname{csch}\left(\sqrt{\frac{4\pi^{2}}{\lambda^{2}} + \frac{\rho \gamma^{2}}{G}}h\right) \right] \right\} - \left(\frac{2\pi G^{2} \gamma^{2}}{\lambda \rho^{2} g^{3}}\right)^{2} = 0.$$
(2.2)

In the above equation, ρ and G stand for the density and the shear modulus of the elastic solid, respectively, and g stands for the acceleration imparted to the elastic solid by the light gas medium. The dispersion relation is here shown for the case where the Atwood number, $At \equiv (\rho_2 - \rho_1)/(\rho_2 + \rho_1) = 1$ with ρ_2 and ρ_1 being the densities of the heavy and light media, respectively. This is because, throughout this thesis, it is always assumed that $\rho_2 \gg \rho_1$. For this reason, in this thesis $\rho_2 = \rho$. It can be shown that a unique positive root for γ is obtained from Eq. (2.2) for any input parameter values where the surface perturbations of the elastic solid are unstable [90–92]. Appendix A.1 contains a derivation of the dispersion relation Eq. (2.2) from the conservation of mass and momentum equations.

From the dispersion relation Eq. (2.2) an analytical stability boundary for the elastic solid can be derived by letting $\gamma = 0$ in Eq. (2.2):

$$\frac{\rho g h}{G} = \frac{2\pi h}{\lambda_{\rm c}} \left[1 - \left(\frac{2\pi h}{\lambda_{\rm c} \sinh \frac{2\pi h}{\lambda_{\rm c}}} \right)^2 \right]^{1/2},\tag{2.3}$$

where the λ_c stands for the *RTI cutoff wavelength*, the wavelength above which the configuration studied in Fig. (1.2) becomes unstable.

The acceleration, g, in this thesis is generated through the use of a shock tube where Δp is the pressure difference across the elastic solid following reflected shock loading which are related via Newton's Second Law:

$$g = \frac{\Delta p}{\rho h}. (2.4)$$

Combining Eqs.(2.3) and (2.4) allows a form of the RTI stability boundary to be obtained that is not depended upon the density of the elastic solid:

$$\frac{\Delta p}{G} = \frac{2\pi h}{\lambda_{\rm c}} \left[1 - \left(\frac{2\pi h}{\lambda_{\rm c} \sinh \frac{2\pi h}{\lambda_{\rm c}}} \right)^2 \right]^{1/2}.$$
 (2.5)

Although Eq. (2.5) is transcendental in the cutoff wavelength, λ_c , it can still be plotted in the λ_c -h space numerically using, for instance, Mathematica's ContourPlot function which plots only the (λ_c, h) pairs that satisfy the equality of Eq. (2.5) in a given parameter space. Figure 2.1 plots Eq. (2.5) in the space delimited by $0 \text{ mm} \le h \le 12 \text{ mm}$ and by $0 \text{ mm} \le \lambda \le 60 \text{ mm}$. These bounds are set by the dimensions of the shock tube apparatus and by the sample manufacturing process (see Chapter 3) which restrain the solid sample dimensions to a 140 mm × 140 mm square. For such a 140 mm × 140 mm square sample, a sinusoidal perturbation with a $\lambda_c = 60 \text{ mm}$ would correspond to the presence of approximately two ripples at the interface between the elastic solid and the accelerating gas.

Figure 2.1a plots three stability boundaries for a solid sample with an elastic shear modulus value of 27 kPa. Each stability boundary represents a different value for the applied Δp . As indicated by Fig. 2.1a, increasing Δp while holding everything else constant increases the size of the instability regime of the configuration—the unstable regime lies above the stability boundary. Similarly, Fig. 2.1b plots the stability for three different elastic shear moduli, $G = 620 \,\mathrm{kPa}$, $G = 120 \,\mathrm{kPa}$, and $G = 27 \,\mathrm{kPa^1}$ with $\Delta p = 5$ bar. Increasing the value of G has the opposite effect to that of increasing the value of Δp , that is, increasing the value of G reduces the size of the instability region.

¹These are the elastic shear modulus values reported in the literature for the silicone elastomers Sylgard 184, Solaris, and Ecoflex 00-30, respectively [94].

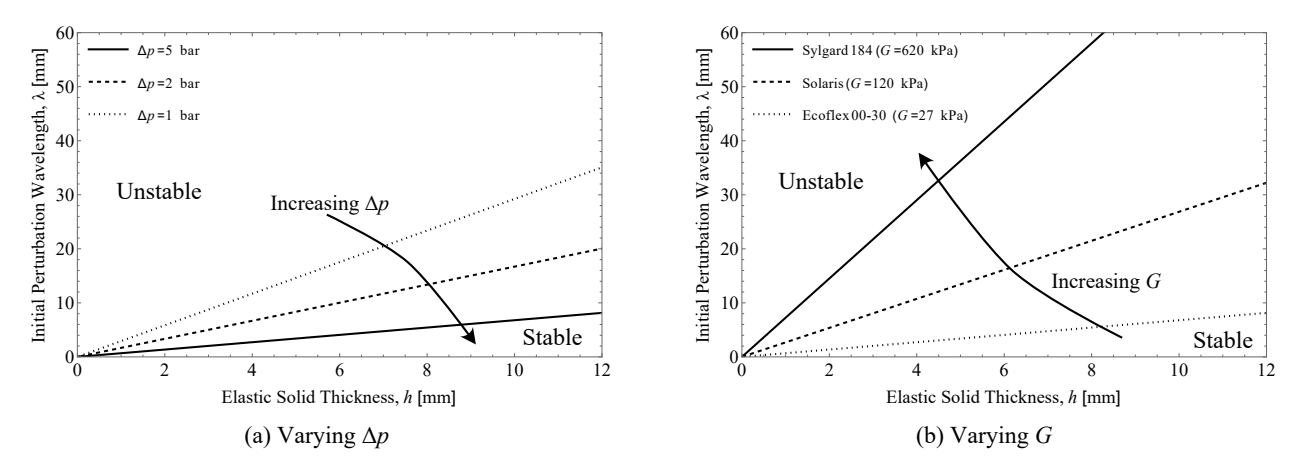


Figure 2.1: Plots of the RTI stability boundary in the λ -h space for different input parameters: (a) varying the driving pressure difference across the elastic solid; (b) varying the elastic shear modulus of the solid.

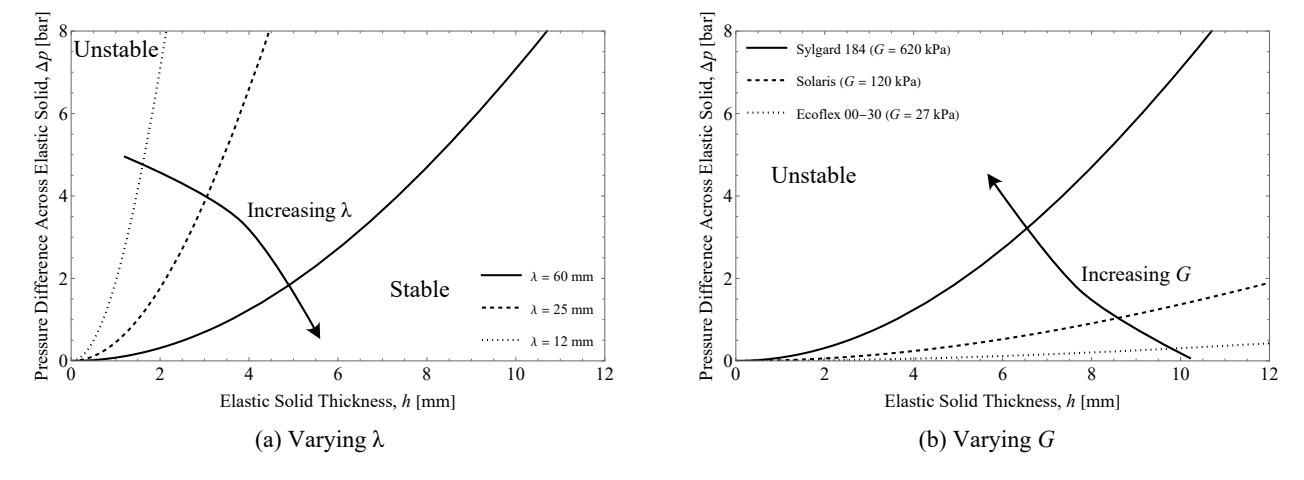


Figure 2.2: Plots of the RTI stability boundary in the Δp -h space for different input parameters: (a) varying the initial perturbation wavelength, λ , of the elastic/fluid interface; (b) varying the elastic shear modulus of the solid.

Figure 2.2 plots the stability boundary in the Δp -h space where 0 bar $\leq \Delta p \leq 8$ bar—these plots can be obtained by isolating Δp in the LHS of Eq. (2.5). The upper limit of 8 bar was determined to be a pressure difference that can safely be applied onto the solid in a laboratory setting. Figure 2.2a plots the stability of a solid with $G=620\,\mathrm{kPa}$ for three different initial perturbation wavelength, λ , of the elastic/fluid interface. Figure 2.2a shows that increasing the size of the initial perturbation wavelengths increases the size of

the instability region. Figure 2.2b plots the stability boundary for the same three different elastic shear moduli, $G = 620\,\mathrm{kPa}$, $G = 120\,\mathrm{kPa}$, and $G = 27\,\mathrm{kPa}$ with $\lambda = 60\,\mathrm{mm}$ held constant. As seen in Fig. 2.2b, increasing the value of G reduces the size of the instability region. It is further noted that the stability boundary Eq. (2.5) appears to linearly relate the elastic solid thickness, h, to the initial perturbation wavelength, λ of the solid/fluid interface while the stability boundary appears to behave like a higher-order polynomial in the Δp -h space.

Alongside the plot of the RTI stability boundary, the dispersion relation Eq. (2.2) can be numerically solved to obtain predictive values for the exponential growth rate, γ . Figure 2.3 is an example of such a stability map generated for the parameters $\lambda=25\,\mathrm{mm}$ and $G=27\,\mathrm{kPa}$. Figure 2.3 indicates that increasing the value of Δp as well as decreasing the value of h both increase the rate of amplitude growth, γ .

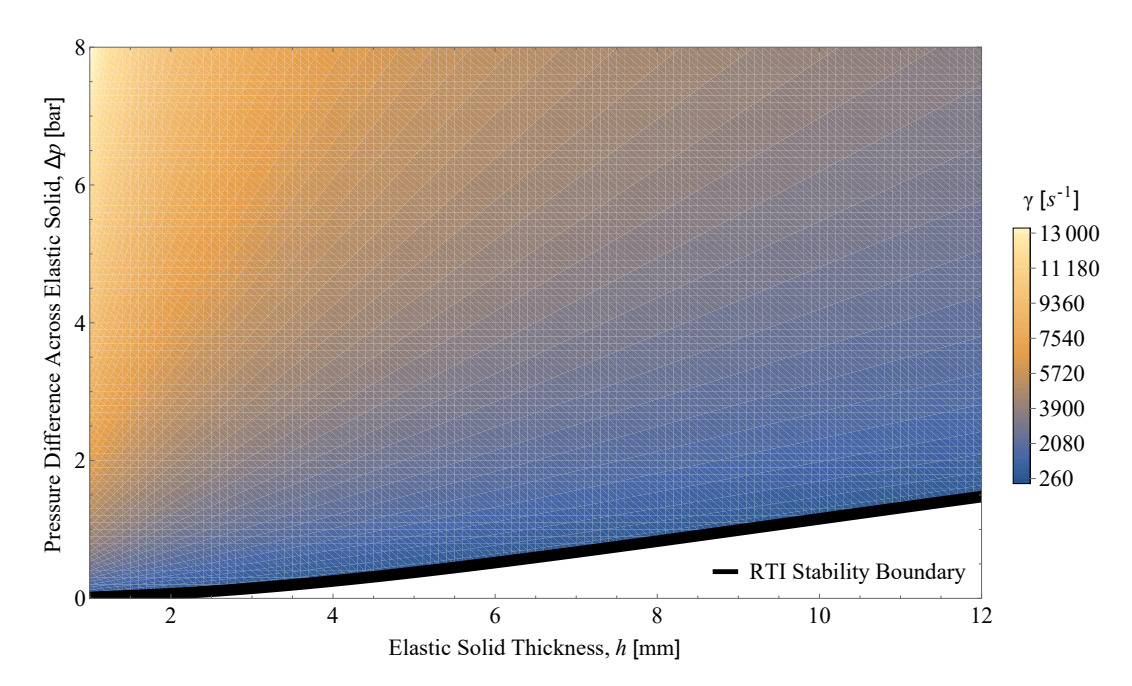


Figure 2.3: Plot of the RTI stability boundary in the Δp -h space alongside contour plots of the exponential growth rate, γ in the unstable region. This stability map is produced for $\lambda = 25 \, \mathrm{mm}$ and $G = 27 \, \mathrm{kPa}$.

The information held in Figs. 2.2 to 2.3 is crucial in order to determine the input parameter values that will most easily allow for the recording of RTI in an accelerated elastic solid with a free surface. This is because shock experiments typically last on the order of no more

than a few milliseconds allowing for only a small time lapse during which RTI may be observed. Choosing a material with the right modulus and the right driving pressure as guided by Eqs.(2.2) and (2.5) will help ensure that RTI interfacial behavior can be experimentally recorded.

2.2 Shock Tube Gasdynamics

To quantify the acceleration of the elastic solid the pressures exerted on both sides of the solid following the initial shock reflection must be established. This section is written in two parts. The first part establishes the shock tube relations necessary to theoretically predict the driving pressures immediately after the elastic solid was shock loaded. The second part derives a method for predicting the velocity history of the elastic solid as the driving gas is expanding following the shock loading of the solid.

2.2.1 Shock Tube Theory

As previously mentioned, the acceleration of the elastic solid, $g = \Delta p/\rho h$, is provided by a shock tube facility. The following discussion uses Fig 2.4 as a reference for all the gas regions being considered during the operation of a shock tube. In the experimental scenario presented in this thesis, a shock tube of uniform cross-section contains a diaphragm separating a high-pressure gas $(Region\ 4)$ from a low-pressure gas $(Region\ 1)^2$. After the rupturing of the diaphragm, the contact surface between the high-pressure and the low-pressure gases pushes a shock wave into the low-pressure section of the tube. $(Region\ 3)$ and $(Region\ 2)$ are the gas regions immediately before and after the contact surface, respectively. As the high-pressure gas is expanded into the low-pressure section of the shock tube, expansion waves (also known as rarefaction waves) form to carry the information of the expansion to the yet undisturbed parts of the high-pressure gas. Once the shock wave hits a solid surface (in this case the surface of one of the elastic solids studied in this thesis), the shock reflects off the surface, leaving behind a pressurized gas at rest with respect to the surface $(Region\ 5)$. Figure 2.4 plots the static pressure in the various regions of interest as a function of axial position, x, along the shock tube at a given time $t = t_1$.

²Throughout this thesis, the shock tube is taken as open ended and thus the pressure in region 1 equals the ambient pressure, that is, $p_1 = p_{amb}$.

After the shock wave reflects off the elastic solid, the pressure difference across the solid sample is instantaneously increased causing its acceleration. To first order, the pressure difference across the solid sample can be expressed as the difference between the gas pressure following the shock reflection, p_5 , and the ambient pressure, p_1 , that is, $\Delta p = p_5 - p_1$. Using 1D gasdynamics theory, p_5 can be related to p_1 as follows [95]

$$p_5 = \left[\frac{2\kappa_1 M_{\rm s}^2 - (\kappa_1 - 1)}{\kappa_1 + 1}\right] \left[\frac{-2(\kappa_1 - 1) + M_{\rm s}^2(3\kappa_1 - 1)}{2 + M_{\rm s}^2(\kappa_1 - 1)}\right] p_1,\tag{2.6}$$

where M_s is the Mach number of the shock wave and κ_1 is the specific heat ratio of the gas initially found in the shock tube driven section (the low-pressure gas throughout this thesis is always ambient air, so $\kappa_1 = 1.4$). Using a single pressure sensor placed somewhere along the driven section of the shock tube, the pressure of the gas immediately behind the propagating shock wave, p_2 , can be measured. The measured p_2 value can then be used to compute the Mach number of the shock wave through the following relation [95]:

$$\frac{p_2}{p_1} = 1 + \frac{2\kappa_1}{\kappa_1 + 1} \left(M_s^2 - 1 \right). \tag{2.7}$$

Using two pressure sensors located a known distance apart, the Mach number of the shock can be experimentally measured: the temporal distance between the two p_2 pressure readings of each sensor can be used to find the speed with which the shock wave traveled the distance between the two pressure sensors.

Knowing the shock wave Mach number, M_s , p_1 , and κ_1 , p_5 can be solved for using Eq. (2.6). The shock Mack number can also be solved for numerically using an equation relating the driving gas pressure, p_4 , to p_1 [95]:

$$\frac{p_4}{p_1} = \left[1 + \frac{2\kappa_1}{\kappa_1 + 1} \left(M_s^2 - 1\right)\right] \left[\frac{1}{1 - \frac{\kappa_4 - 1}{\kappa_1 + 1} \frac{c_1}{c_4} \left(M_s - \frac{1}{M_s}\right)}\right]^{\frac{2\kappa_4}{\kappa_4 - 1}},$$
(2.8)

where κ_4 is the specific heat ratio of the driving gas, and c_1 and c_4 are the speeds of sound in the driven and driving shock tube sections, respectively. Because p_4 is set right before diaphragm rupture, M_s can numerically be solved for in the above equation, allowing for yet another means of computing the value of p_5 .

Appendix A.2 derives the shock tube relations (2.6)–(2.8) from first principles starting with the 1D conservation equations of gasdynamics.

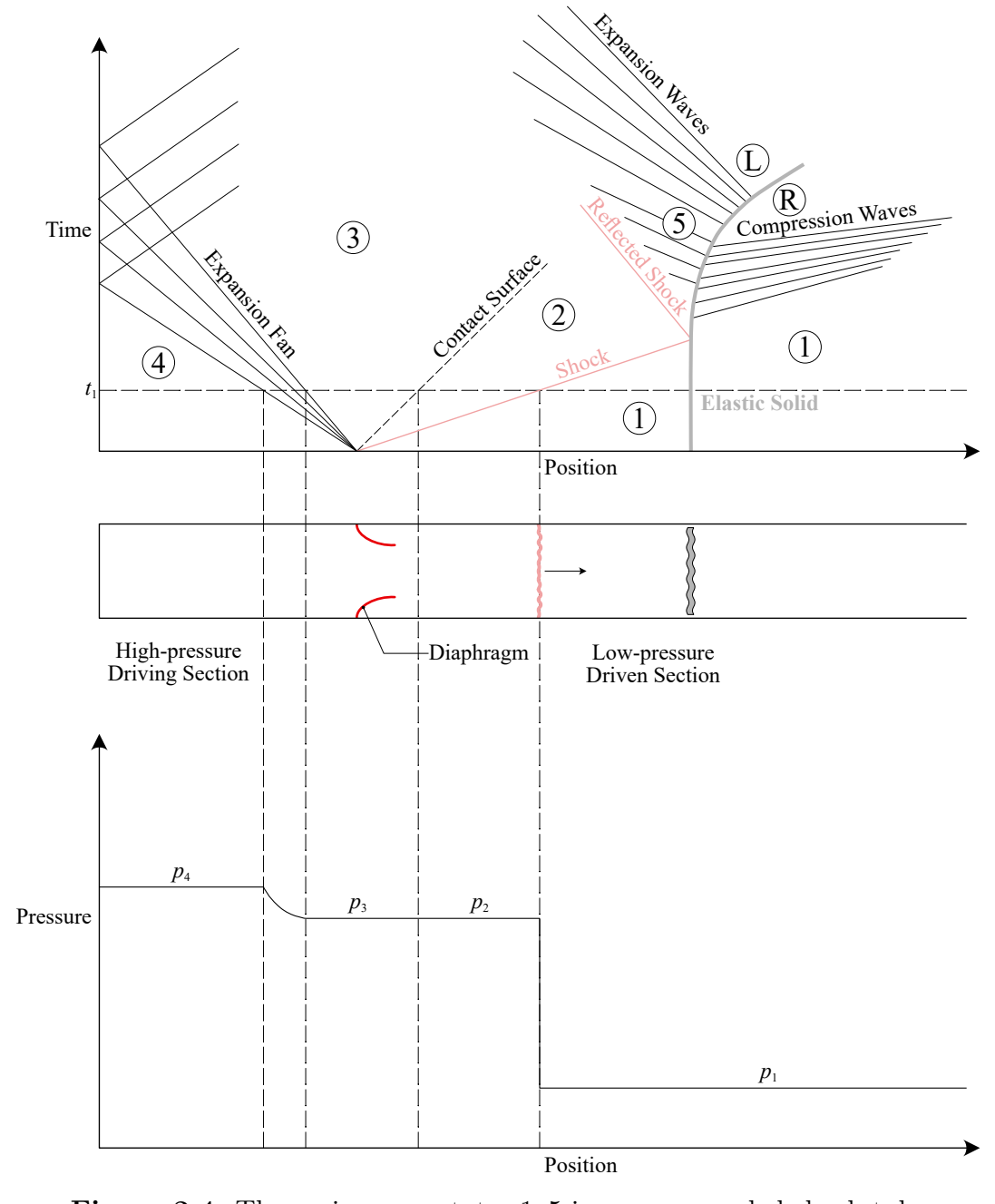


Figure 2.4: The various gas states 1–5 in an open-ended shock tube.

2.2.2 Shock-Induced Acceleration of the Elastic Solid

While the pressure difference across the elastic solid can be considered to first order as equal to $p_5 - p_1$ (recall that the shock tube is open-ended so $p_1 = p_{amb}$), a better approximation can be obtained by modeling the elastic solid/shock wave interaction as a 1D piston driving a projectile. What follows is a paraphrasing and adaption of the treatment of Higgins for the expansion of propellant gas in a conventional gun following projectile release [96].

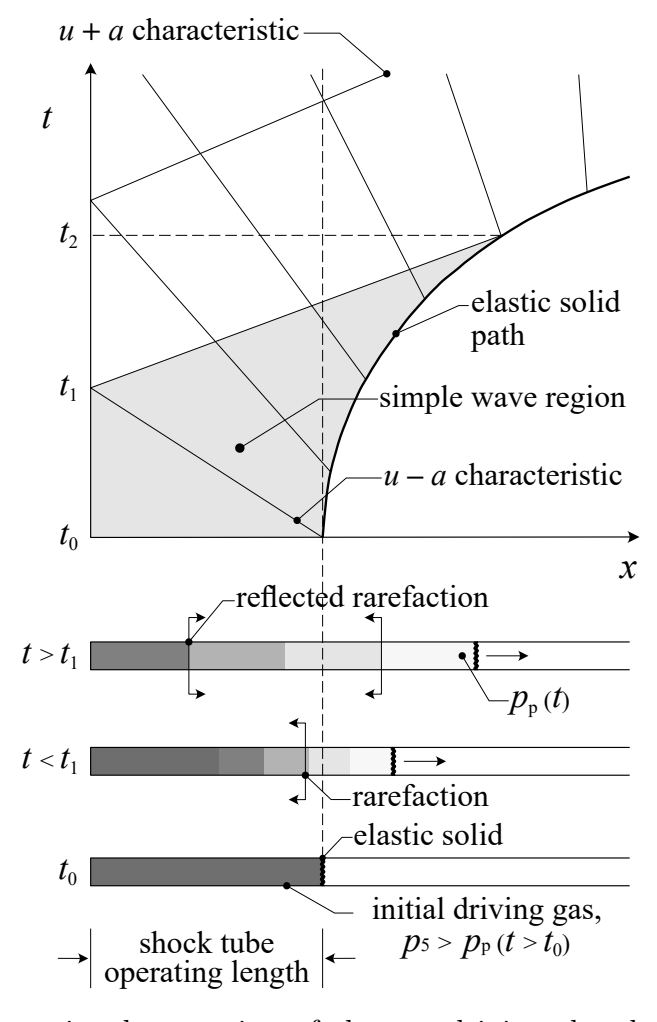


Figure 2.5: One-dimensional expansion of the gas driving the elastic solid immediately after shock reflection. Image adapted from [96] with permission.

Immediately following shock reflection, the elastic solid moving forward generates expansion waves that propagate back into the shock tube, expanding the gas in region 5

and lowering the pressure that is accelerating the solid. The first characteristic expansion wave propagating backwards at time t_0 following shock reflection travels with a speed $u(x,t) - c(x,t) = -c_5$ where u(x,t) and c(x,t) are the velocity and the speed of sound of the gases found within the shock tube. The first expansion wave eventually reflects off the shock tube end wall at a time t_1 after which it will propagate back towards the accelerated elastic solid, potentially reflecting off the solid surface at some time t_2 . All forward moving, u(x,t) + c(x,t) characteristics reaching the accelerating elastic solid in the $t_2 - t_0$ time span will cause an expansion of the gas in region 5. The region bounded by the first reflected characteristic reaching the solid at time t_2 is called the *simple wave region* (see Fig. 2.5) by Higgins as this region is unaffected by reflected waves.

Recall that the Riemann invariant along a u(x,t) + c(x,t) characteristic is $u + 2c/(\kappa - 1)$ and so a relationship between the state in region 5 immediately following shock reflection and the state in the same gas at later times can be obtained:

$$u(t) + \frac{2c(t)}{\kappa - 1} = \frac{2c_5}{\kappa - 1} \tag{2.9}$$

The spatial dependency of u(t) and c(t) have been dropped in the above equation as region 5 is taken to be occupied by the same gas undergoing 1D flow. Since the gas velocity at the base of the elastic solid must match the velocity of the solid itself, that is, since $u(t) = v_s(t)$, then rearranging the above equation further yields that

$$\frac{c_{(t)}}{c_5} = 1 - \frac{(\kappa - 1)}{2} \frac{v_{s}(t)}{c_5} \tag{2.10}$$

Assuming the expansion process to be isentropic, the original pressure in region 5, p_5 , and the pressure at later times during the expansion process, $p_p(t)$, can be related using the isentropic equation

$$\frac{p_{\rm p}(t)}{p_5} = \left(\frac{c(t)}{c_5}\right)^{\frac{2\kappa}{\kappa-1}}.\tag{2.11}$$

Substituting Eq. (2.11) into Eq. (2.10), the pressure driving the elastic solid can be expressed as a function of the original speed of sound in region 5, c_5 , and of the velocity of the elastic solid, $v_s(t)$:

$$p_{\rm p}(t) = \left[1 - \frac{(\kappa_5 - 1)}{2} \frac{v_{\rm s}(t)}{c_5}\right]^{\frac{2\kappa_5}{\kappa_5 - 1}} p_5 \tag{2.12}$$

Now writing the pressure difference accelerating the elastic solid as $\Delta p(t) = p_{\rm p}(t) - p_{\rm 1}$, substituting the expression for $p_{\rm p}(t)$ from the above Eq. (2.4) into Newton's Second Law for the elastic solid yields the following nonlinear differential equation

$$g = \dot{v}_{s}(t) = \frac{\left[1 - \frac{(\kappa_{5} - 1)}{2} \frac{v_{s}(t)}{c_{5}}\right]^{\frac{2\kappa_{5}}{\kappa_{5} - 1}} p_{5} - p_{1}}{\rho h}.$$
 (2.13)

The above equation can be numerically integrated to obtain a theoretical velocity history of the elastic solid sample, $v_s(t)$, provided that the values for p_1 and p_5 are known.

Chapter 3

Experimental Methods

To perform the RTI experiments, elastomeric solid samples were manufactured by means of a casting method using 3D printed molds. A casting process was used as it allowed for the sample surface to be sinusoidally perturbed. The solid samples were lightly attached in a style similar to a shower curtain to the end of a shock tube made out of square aluminum sections using four to five standard sewing needles. The samples were lightly attached in order to minimize the influence of boundary effects such as the tensioning of the samples which is known to help stabilize Rayleigh-Taylor instabilities. Two pressure transducers were positioned at the end of the shock tube to measure the strength of the shock wave produced and to trigger data acquisition. When the shock wave impacts and subsequently reflects off the elastic solid surface, a pressure difference is created across the sample which generates the acceleration required to study RTI.

A high-speed video camera (typically the Shimadzu HPV-X2 but sometimes also the Photron SA5) recording at a frame rate between 50 000 fps and 200 000 fps was used to obtain video recordings of the samples following the initial shock reflection. The high-speed video camera was always fitted with a Nikon 80–200mm f/2.8 AF-D ED Macro lens whose f-stop was typically set to 5.6, the sharpest f-stop of the lens. The velocity histories of two central peak/trough pairs were recorded using photonic doppler velocimetry with each PDV channel being configured in a standard homodyne setup. Figure 3.1 shows an infographic of the experimental setup.

What follows is a more detailed description of three important aspects of the experimental methodology: the first section of this chapter describes the manufacturing of the solid

samples; the second section describes the shock tube apparatus in greater detail; and the third section of this chapter describes the PDV apparatus and the PDV data acquisition process.

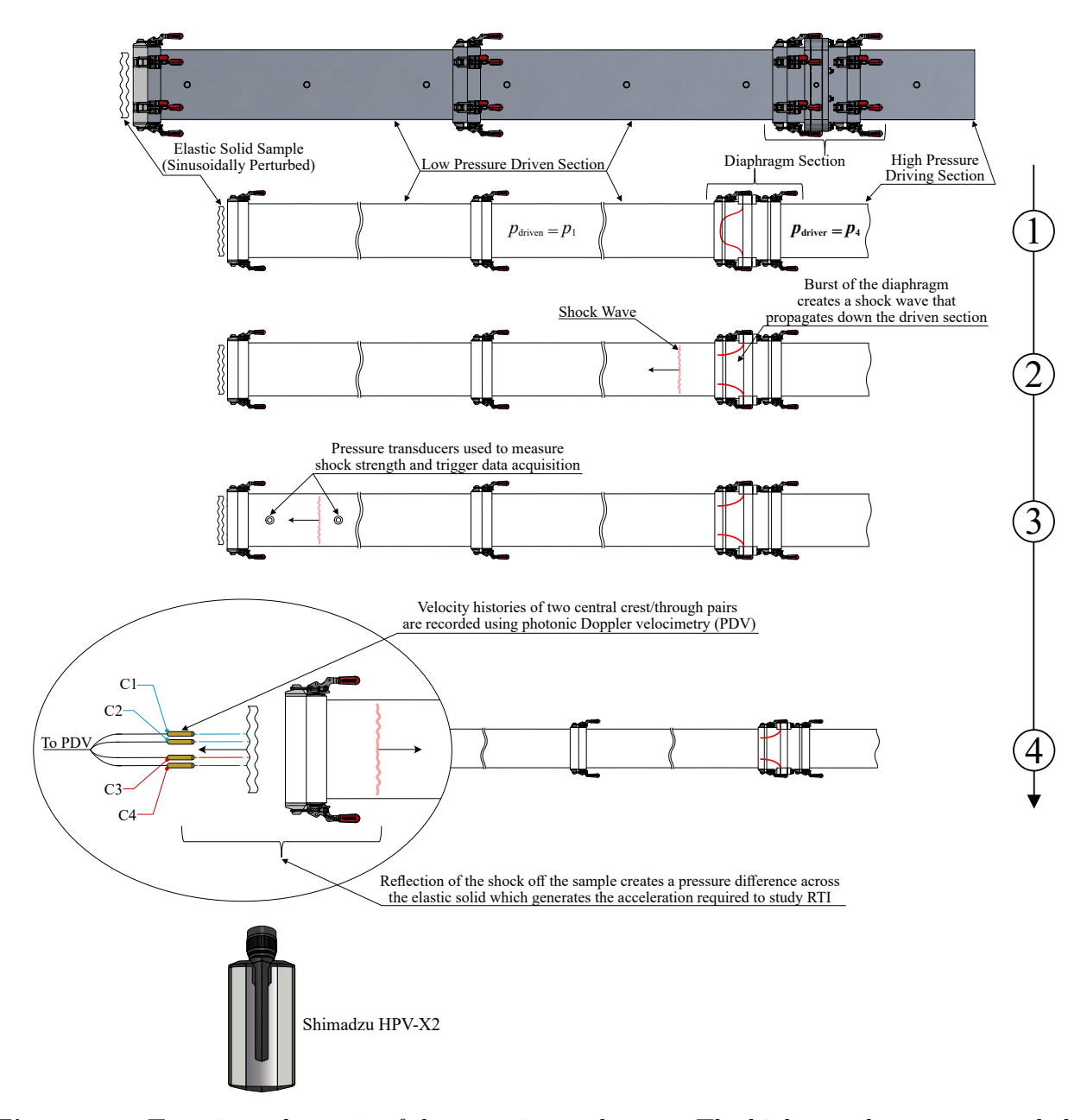


Figure 3.1: Top-view schematic of the experimental setup. The high-speed camera recorded a top view of the experiment through the use of a mirror positioned above the elastic solid sample.

3.1 Manufacturing the Solid Samples

The vast majority of the elastic solid samples tested were manufactured using a relatively novel silicone elastomer named Ecoflex 00-30 made by Smooth-On Inc. [97]. This material is typically used to make face masks and prosthetics owing to its skin-safe and skin-like properties which make the material highly flexible and highly tear resistant with storage shear modulus values reported in the literature of about 27 kPa [94]. Although the Ecoflex material is nominally transparent, the product can be colored using silicone-based coloring pigments such as Smooth-On's Silc Pig which can further help with the experimental data acquisition—coloring the samples white, for instance, provides higher quality imagery during monochromatic video recordings. Using molds 3D printed, this relatively inexpensive material was cast into 140 mm × 140 mm sinusoidally perturbed samples of known thickness, h, initial perturbation amplitude, a_0 , and initial perturbation wavelength, λ . The Ecoflex 00-30 material has a 4-hour curing time, and, thanks to the recent advancements in additive manufacturing, modern benchtop 3D printers like the Bambu Lab X1 Carbon can readily print the molds used in the casting process in less than 15 hours, allowing for the rapid production of test samples. Figure 3.2 displays a few of the used 3D printed molds alongside some Ecoflex 00-30 samples.

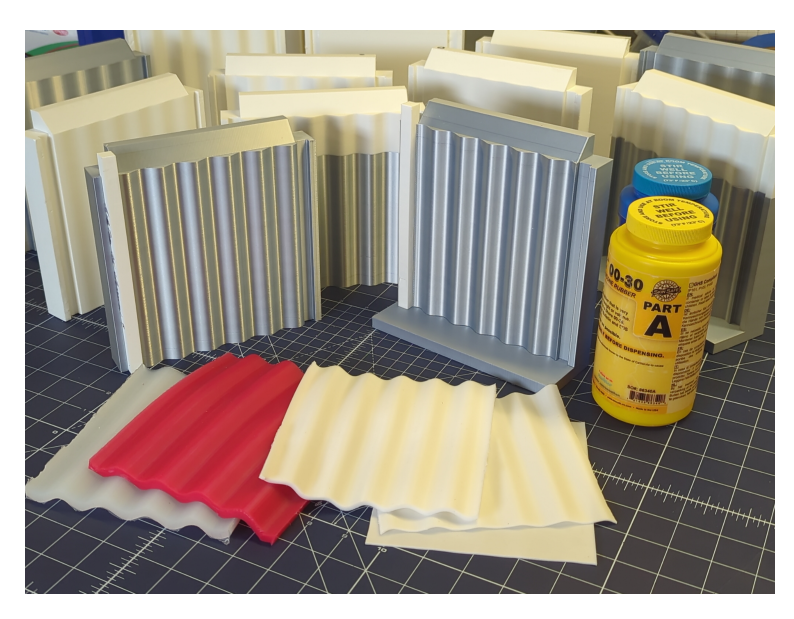


Figure 3.2: Ecoflex 00-30 samples alongside 3D printed molds.

The 3D printed molds consisted of 4 parts: two blocks with the sinusoidal perturbations of a chosen amplitude and wavelength designed onto their mating surfaces and two rectangular keys that, when positioned in their pairing slots located at the edges of the mating blocks, allowed for the alignment of the casting blocks and dictated the thickness of the solid sample to be casted. This key-slot design was chosen to help eliminate the need for the 3D printing of molds for samples of different thicknesses. Instead of having to 3D print new sinusoidal blocks when the manufacturing of a sample of different thickness was required, the alignment keys were swapped instead for keys of different thicknesses. This design choice reduced 3D printing material cost and decreased sample manufacturing down time. The molds were typically 3D printed using polylactic acid (PLA) as this material is one of the least expensive 3D printing materials and is also relatively easy to print with, not requiring special nozzles, printer enclosures, etc., although other materials such as acrylonitrile butadiene styrene (ABS) was also infrequently used to manufacture the molds. In the case of PLA, after multiple trialand-error attempts, the 3D printing settings that offered the most robust, long-lasting molds while keeping the 3D printing time to a minimum are itemized below. Note that the 0.12 mm Fine Bambu Lab X1 Carbon printing profile was used as a basis for the 3D printing settings, so the printing parameters indicated here are only the settings that were changed from the default Fine profile:

- The infill density was set to 10 % to minimize 3D printing material use and build time.
- To compensate for the sparse infill density, 3 wall loops were used alongside 8 and 6 top and bottom shell layers, respectively. The 8 top layers help avoid the warping of the top layer surfaces that typically occurs when sparse infill density is used.
- The 3D printing seam for each large block was set along one of the back edges. Otherwise, the sinusoidal surfaces of the mold blocks would typically contain indents as a result of the random distribution of the layer seams.
- The order of the wall construction was changed to outer/inner/infill as testing indicated that this order resulted in a smoother surface finish for the sinusoidal surfaces of the mold.

Appendix B.1 describes a detailed procedure for the casting process of the solid samples. The casting procedure can also be used to produce solid samples out of materials other than Ecoflex 00-30 albeit sometimes with different mixing ratios between the base polymer and curing agents. Other materials silicone elastomer materials such as Smooth-On's Solaris and Dow Corning's Sylgard 184 have also been manufactured using this casting procedure. Urethane samples have also been produced using this method.

3.2 The Shock Tube Apparatus

The low-cost shock tube was constructed using three 4-feet-long extruded aluminum channels with 5-inch \times 5-inch internal cross-section dimensions. Figure 3.3 shows a labeled 3D render of the shock tube apparatus. Two of the three aluminum channels made up the low-pressure driven section. The third aluminum channel made up the high-pressure driving section. The assembly of the three sections featured a modular design employing Destaco 323-type clamps. Eight Destaco clamps were used per section joint with the clamps being screwed onto the section end flanges through the use of 8-mm-long M4 \times 0.7 mm black-oxide screws. For additional sealing at the section jointures, oil-resistant Buna-N o-rings with a 7-inch outer diameter and a 1/8-inch width were placed in-between the mating aluminum channel end flanges. The diaphragm section connecting the low-pressure and high-pressure sections was further reinforced via the addition of twelve 2 1/4-in-long 1/4–20 alloy steel socket head cap bolts.

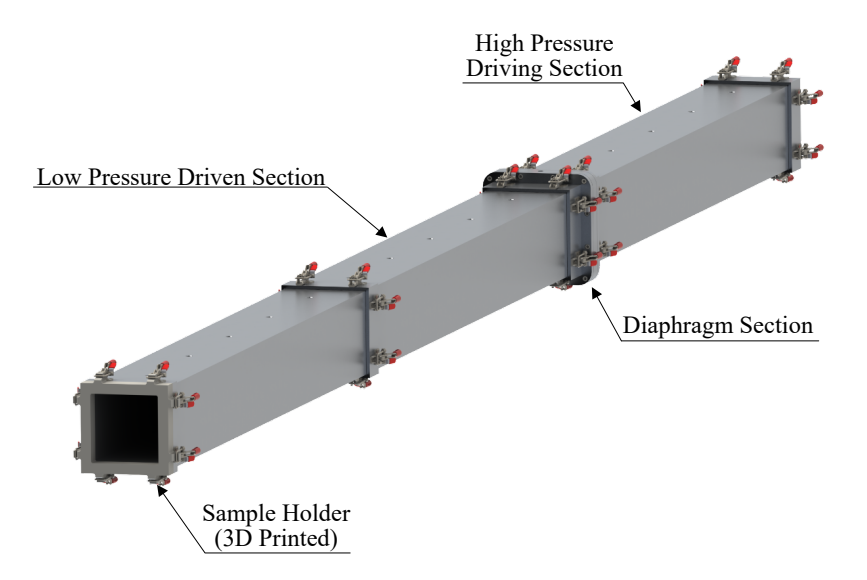


Figure 3.3: Labeled 3D render of the shock tube used throughout this thesis.

The diaphragms used were laser cut out of Mylar polyester film made by DuPont Teijin Films. The cut Mylar diaphragms nominally were of either 0.5, 1.0, or 2.0 thou in thickness (1 thou = 0.001 in and a thou is also sometimes called a mil), but the diaphragms were often stacked together to produce effective diaphragms of different thicknesses. The shock tube low-pressure section was always left open-ended. The low-pressure section open-end was also equipped with a 3D printed flange meant to lightly hold the elastic samples prior to their shock loading. The elastic solids were attached to the 3D printed end flange via either four or five standard stainless steel sewing needles that were epoxied to the sample holder.

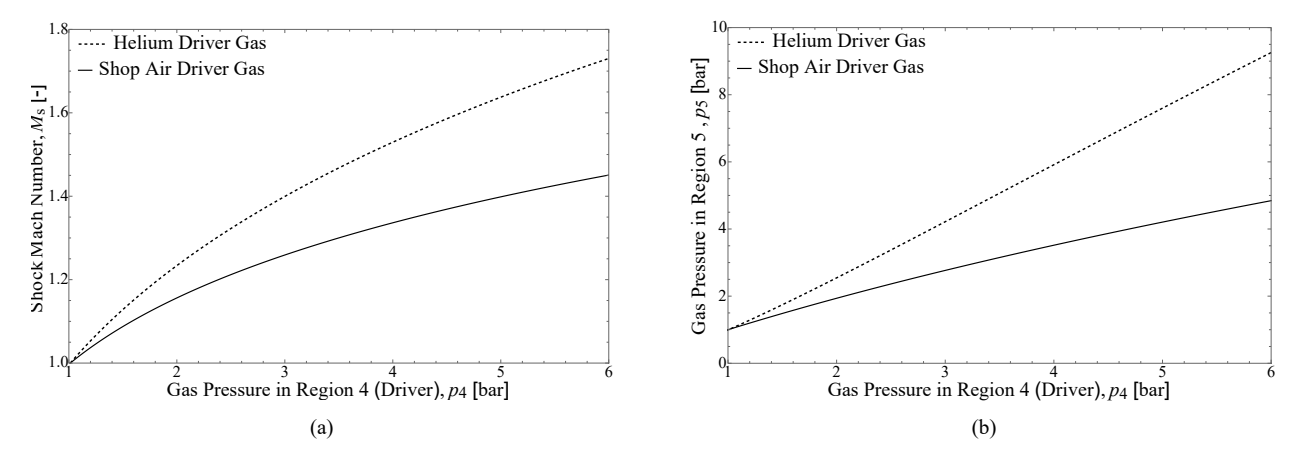


Figure 3.4: Theoretical shock tube M_s vs p_4 (a) and p_5 vs p_4 (b) plots for helium (dashed) and shop air (solid) as the driving gases.

The shock tube diaphragm section is equipped with an inlet through which pressurized gas can be deposited in the driver section. The inlet is equipped with 1/4-inch 316 stainless steel Swagelok tubbing components alongside an SSI Technologies, LLC digital pressure gauge (Model MGA-300-A-9V-R) in a manner allowing for both the pressurizing and vacuuming of the driver section. Although unnecessary when pressurized shop air is used as the driver gas, vacuuming was used to empty the driver section prior to the insertion of pressurized helium gas into the driver section. Helium was also used as a driver gas as it can produce stronger shock waves owing to its lighter mass relative to shop air. From in-laboratory testing, it was found that the shock tube driver section can safely sustain up to 60 psig of pressure which is the imperial equivalent of 6 bar of absolute pressure. Using 5.17 bar of absolute pressure as the maximum value for the driver pressure, p_4 , Fig. 3.4 plots the shock Mach number, M_s , and the pressure behind the shock immediately after reflecting off the solid sample, p_5 , as a

function of the driver pressure for both helium and shop air acting as the driver gas. The graphs in Fig. 3.4 were obtained by numerically solving Eqs. (2.6) and (2.8) in tandem as outline in Section 2.2. The specific heat ratio, γ_4 and speed of sound c_4 in the driver section were taken as $\kappa_4 = 1.4$ and $c_4 = 343 \,\text{m/s}$ for shop air, and $\kappa_4 = 1.667$ and $c_4 = 1008 \,\text{m/s}$ for helium.

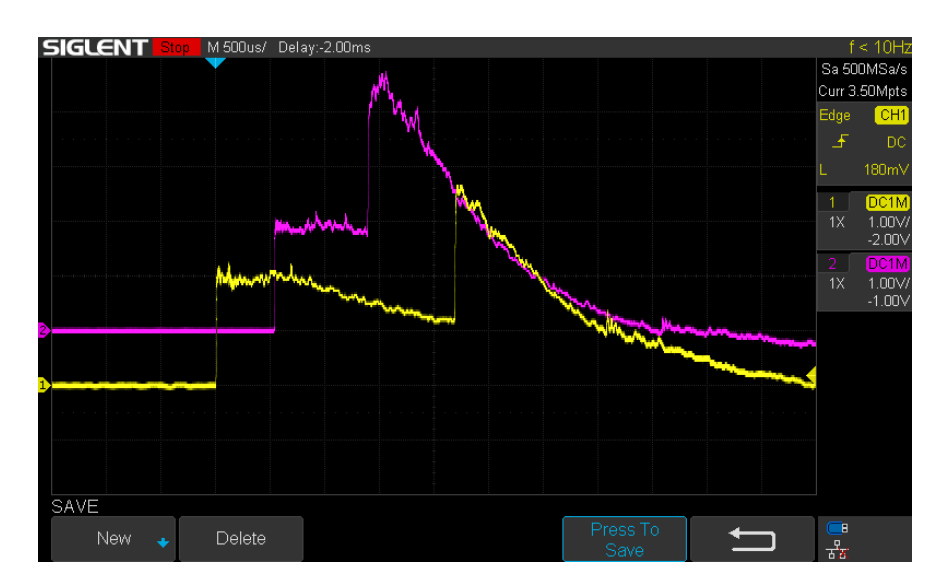


Figure 3.5: Image capture of pressure data recorded by the Siglent SDS1104X-E oscilloscope following a $p_4 = 42$ psig shot with helium in the driver. The yellow and purple traces represent the data acquired by the first and second pressure transducers, respectively—the first pressure transducer is the first sensor to encounter the shock wave.

The pressure immediately behind the generated shock wave, p_2 , following shock reflection off the elastic solid, p_5 , and the shock Mach number, M_s were also experimentally determined using two piezoelectric pressure transducers (Model 113B28, PCB Piezotronics Inc.) located at the open-end of the shock tube. The pressure transducer data was recorded using a Siglent SDS1104X-E digital oscilloscope. Figure 3.5 shows an image capture of the pressure data recorded by the Siglent oscilloscope for an experiment where the driver section was pressurized to 42 psig using helium gas. The data acquisition was triggered off the first pressure trace (the yellow trace in Fig. 3.5). The first pressure trace was produced by the transducer that first encountered the shock wave. Because the distance between the two transducers was always equal to 26.2 cm, the shock wave would typically take about a millisecond to travel from one transducer to the next so the time base was always set to 500 µs per division. The

vertical voltage scale varied between 200 mV per division for low driver pressure shots (shots which used less than $p_4 \leq 32$ psig with shop air), 500 mV per division for medium driver pressure shots (shots which used 32 psig $\leq p_4 \leq 42$ psig with shop air), and 1 V per division for high driver pressure shots (shots using helium as the driver gas with $p_4 \geq 42$ psig). The voltages were translated into pressure readings through knowledge of the fact that each pressure transducer had a sensitivity of 100 mV per psi while also noting that the sensors measure changes in pressure and not absolute pressure. The first peak of each pressure trace represents p_2 , and the second peak represents p_5 . The speed of the shock wave can be computed by dividing the set distance between transducers of 26.2 cm by the temporal distance between the first pressure peaks in each trace, and so M_s can also be experimentally inferred. Additional oscilloscope setup parameters such as trigger type, trigger level, sampling rate, etc. can be read off the oscilloscope image capture displayed in Fig. 3.5.

3.3 Photonic Doppler Velocimetry

Photonic Doppler velocimetry records velocity histories through the beat frequency obtained by the so-called heterodyning of two laser signals: a reference signal of a known frequency, the retroreflector path in Fig. 3.6, and a twice Doppler shifted target signal, the probe path in Fig. 3.6. The target velocity, $v_{\rm t}(t)$ can be related to the known laser frequency f_0 and to the measured beat frequency $f_{\rm b}$ through the relation shown below

$$f_{\rm b} = \frac{2v_{\rm t}(t)}{c^*} f_0,$$
 (3.1)

where c^* is the speed of light in vacuum. For an input laser frequency $f_0 = 193 \,\text{THz}$ (which is the equivalent of an input laser wavelength of 1550 nm), Eq. (3.1) becomes

$$v_{\rm t}(t) = 0.775 f_{\rm b} \left(\frac{\rm m/s}{\rm MHz}\right). \tag{3.2}$$

Appendix B.2 provides a derivation of Eq. (3.1) from first principles while also containing a more extensive discussion on the relationship between the system bandwidth of the PDV and the maximum target velocity that can be reliably measured.

Since its first formal establishment in the mid 2000s as a tool for recording velocity histories in shock physics experiments [98], the PDV apparatus scheme has seen different

iterations emerge, each with its own advantages and disadvantages. For the sake of brevity, this thesis will focus on the PDV geometry shown in Fig. 3.6, the original homodyne PDV geometry proposed by Strand et al. [98], which was the PDV configuration used in all four channels of the McGill PDV system during the recording of the experiments described in this thesis. The PDV apparatus consists of three main components: a high-power laser, a three-port circulator, and a digitizer.

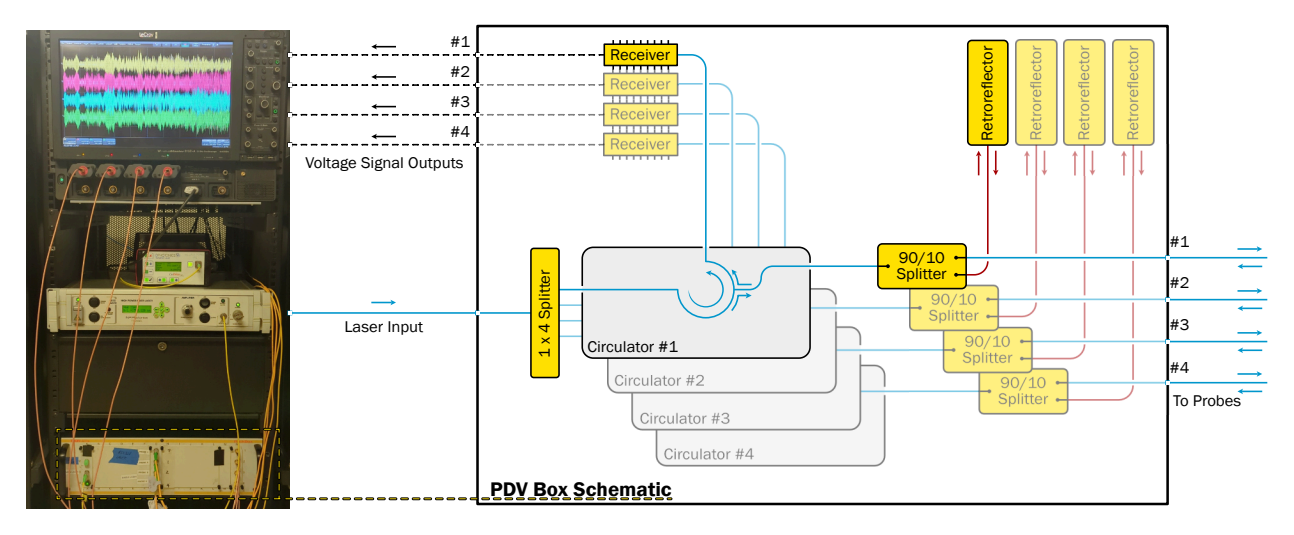


Figure 3.6: Schematic of the PDV homodyne setup contained within the McGill PDV box. The left image is a picture of the McGill PDV apparatus including the LeCroy high-bandwidth oscilloscope and the NP Photonics input laser.

The PDV system makes use of a high-power (power output on the order of watts) CW fiber laser. The specific fiber laser used at the McGill shock tube facility is a NP Photonics The Rock high-power laser with a maximum power output of 5 W when operating at 1550 nm. Fiber lasers make use of rare-earth element doped optical fibers as their active medium [99]. The optical resonator in fiber lasers are typically two fiber Bragg gratings (FBG) spliced at the ends of the active medium fiber. Continuous wave lasers are preferred in transient single shot experiments as such lasers do not require a trigger mechanism to ensure that experiment data is adequately recorded: the CW laser is instead simply turned on a few minutes before the experiment to allow the laser output to stabilize. Fiber lasers also have narrow linewidths—the NP Photonics fiber laser has a 3 kHz linewidth—which is necessary for the proper working of the heterodyne recording technique [98, 100–102]. That such high-power lasers are used for velocity data acquisition in shock experiments stems in part

from the fact that the reflective quality of the surface whose velocity is being measured can drastically change throughout the shock experiment and so what was originally a specular reflector may become a diffuse reflector which can drastically reduce return signal power. The use of high-power lasers also allows for the splitting of the signal in multiple channels.

At the core of the PDV apparatus stands a (typically 3-port) fiber circulator. Through the use of fiber isolators, light entering port 1 may exit at port 2, light entering port 2 may exit at port 3, and light entering port 3 may exit at port 1, while the propagation of light in any other direction (say, from port 2 to port 1, for example) is highly inefficient. To allow for the mixing of the reference and Doppler-shifted signals, a 90:10 fused fiber coupler is installed between the 2nd circulator port and the PDV probe. The 1×2 fiber coupler splits the reference signal into two sending 10% of its input power to a retroreflector and the remaining 90% to the PDV probe. The retroreflector (a passive component) reflects 99% of the light incident upon itself. The reflected light is then mixed with the Doppler-shifted light returning from the probe by the 1×2 splitter. The mixed light is then sent back into the circulator port 2 and exits the circulator port 3 to find its way to the photodetector. The system is entirely fiber coupled (except for the receiver-digitizer connection), with the use of $9/125^1$ single mode fibers and Thorlabs FC/APC fiber connectors.

A 4-channel LeCroy WaveMaster 813Zi-A real-time oscilloscope is used as a digitizer. This oscilloscope has a 13 GHz bandwidth and has a sampling rate of $40\,\mathrm{GS/s}$. Given the sampling rate of the oscilloscope, the Nyquist theorem indicates that a beat signal of a maximum frequency of $20\,\mathrm{GHz}$ may be recorded. A $20\,\mathrm{GHz}$ beating frequency corresponds to a specimen velocity of about $15\,500\,\mathrm{m/s}$. Given the large sampling rate of this oscilloscope, standard Bayonet Neill-Concelman (BNC) connections cannot be used as their bandwidth of $4\,\mathrm{GHz}$ is too low, constituting a severe bottleneck. SubMiniature version K (SMK) connectors are used instead with a $46\,\mathrm{GHz}$ bandwidth and a $50\,\Omega$ characteristic impedance, thereby removing the coaxial connection as the bandwidth bottleneck.

Because of the 4-channel design of the LeCroy oscilloscope, the PDV system is also setup with a 4-channel geometry. Given the circulator power rating of 300 mW, the fiber laser is set to output 800 mW such that when its signal is split in four channels the laser power per

 $^{^{1}}$ The 9/125 specification of an optical fiber indicates the core diameter in microns (here 9 µm) and the cladding outer diameter (here 125 µm). In the C-band operation bandwidth range of 1530–1570 nm, 9/125 fibers act as single mode fibers while higher core diameter fibers like 50/125 fibers act as multimode fibers.

²With a reference signal wavelength of 1550 nm

channel becomes $200 \,\mathrm{mW}$. The Doppler shifted signal power returning from the probe is typically in the $0.01 \,\mathrm{mW}$ to $1 \,\mathrm{mW}$ range. Probe performance is characterized by the return loss (RL) of the sent power, P_{s} , to the received power, P_{r} [101, 102]:

$$RL \equiv 10 \log_{10} \left(\frac{P_{\rm s}}{P_{\rm r}} \right) \tag{3.3}$$

Typical return losses range from $10\,\mathrm{dB}$ to $40\,\mathrm{dB}$ for focusing probes and $20\,\mathrm{dB}$ to $60\,\mathrm{dB}$ for collimating probes (focusing probes are used for specular targets and collimating probes for diffuse targets) [101, 102]. The return losses range of the shock tube facility PDV collimating probes is 23– $43\,\mathrm{dB}$. The MITEQ PIN optical detectors (PN:DR-125G-A-FA) used have a maximum power rating of $10\,\mathrm{mW}$ and so the reference signal reflected back by the retroreflector is further reduced to $2\,\mathrm{mW}$ when reentering the 1×2 splitter in order to ensure that the photodetector maximum rating is not exceeded. This is especially important during shock physics experiments as the nature of the transient acceleration phase may change the specimen reflectivity which sometimes causes the power of the reflected signal to briefly drastically increase. The MITEQ PIN photodetector has a responsivity of $0.9000\,\mathrm{A/W}$ and is integrated with a low noise amplifier (LNA). The photodetector has a bandwidth of $12.5\,\mathrm{GHz}$, which constitutes the bottleneck bandwidth of the system.

Figure 3.6 also contains a picture of the full PDV system setup inside a roll-around box. The 1×4 splitter, the circulator, the attenuators, power meters, and detectors are all contained within the bottom chassis, on the top of which are the NP Photonics fiber laser, and the LeCroy oscilloscope. A second, tunable laser is found between the main fiber laser and the oscilloscope and is used for frequency-shifted PDV configurations, a configuration not used during the recording of the experiments found in this thesis—see Ref. [101] for a comprehensive description of the various PDV configuration available to record velocity histories during shock experiments. A schematic attempting to provide as accurate a placement of the various components as is possible in order to ease the modification of the PDV configuration of a given channel if ever deemed necessary can be found in Appendix B.3.

The voltage signal recorded by the real-time oscilloscope can be converted into a velocity time history $(v_t \text{ vs } t)$ plot in either of two ways. The first method uses the individual fringes (the crests and troughs) of the voltage signal to directly infer the displacement of the target

surface at a given time. This first, brute force method is very computationally demanding and typically inaccurate at high target velocities where the voltage signal becomes too noisy for the individual fringes to be analyzed [98]. Instead, for most experiments, PDV data analysis is performed using a sliding window Fast Fourier Transform (FFT) [98, 100–102]. When using the FFT method of analysis, the recorded voltage signal is first divided into short, overlapping temporal segments. Each of the temporal segments is analyzed using a FFT algorithm to determine the frequency spectrum of the segment. The dominant frequency is determined to be the beat frequency of the segment from which the target velocity during the temporal segment can be obtained. Figure 3.7 provides a visual overview of the FFT method of data analysis. When the FFT method is employed correctly, the PDV can provide velocity time histories of the target surface with velocity uncertainty lower than $\sim 1\%$ [98, 100–102].

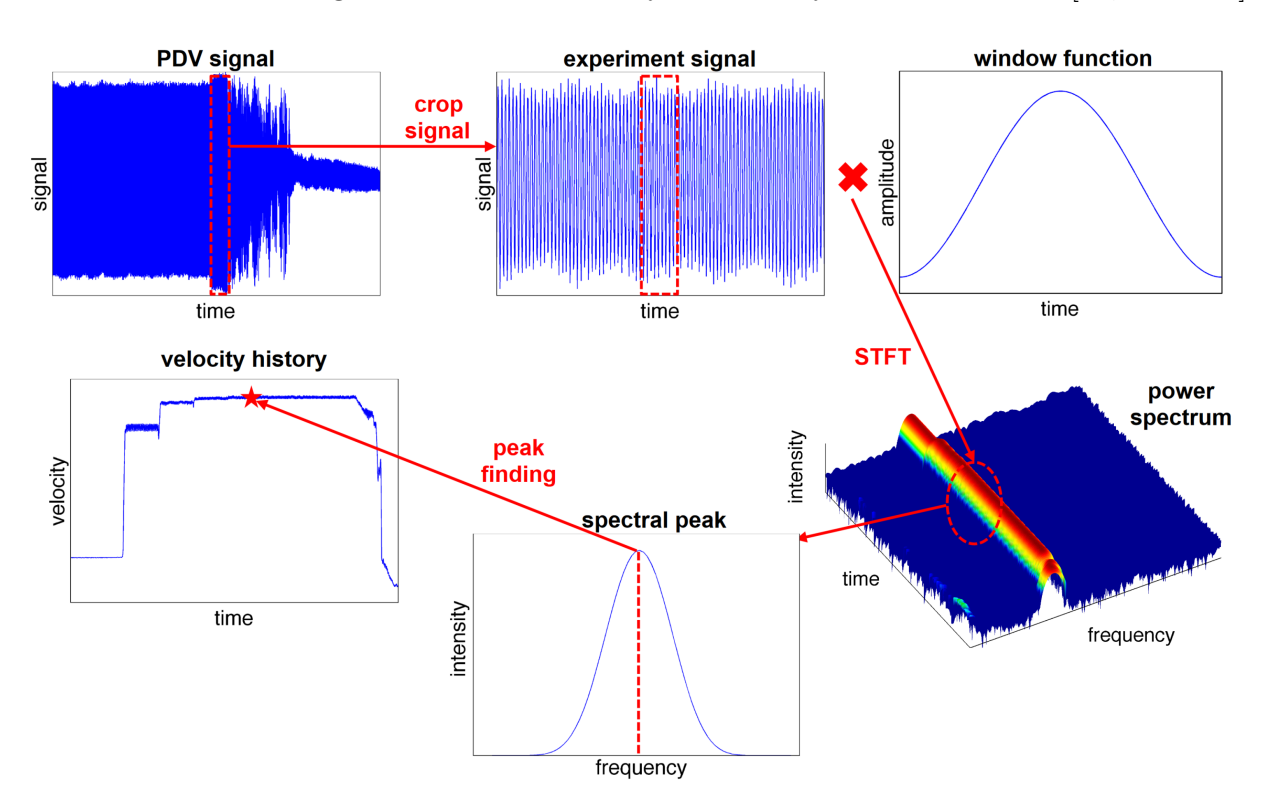


Figure 3.7: The sliding window FFT procedure for PDV data analysis. Image taken from [100] with permission.

Chapter 4

Results and Discussion

This chapter is divided into two parts. The first part, spanning the first four sections of this chapter, presents a sample of the experimental results obtained. The second part, contained in the last section of this chapter, discusses the results obtained while providing suggestions for future improvements of the experimental methods employed.

4.1 Shock Loading of Sinusoidally Perturbed Ecoflex 00-30 Samples

What follows is the description of four representative experiments. Each sample described in this section was loaded using a 1.47 Mach shock in ambient air which, using standard 1D shock tube relations [95], generates a theoretical driving pressure difference of 4.08 bar, which was experimentally verified using piezoelectric pressure sensors. The distance between the starting position of each sample and the PDV probes, that is, the total distance traveled by a sample was always of 34 mm. This distance was chosen as it was the largest distance that reliably allows for the PDV collimators to be aimed at their respective crests and/or troughs for the entire distance traveled by the sample. Each sinusoidally perturbed sample discussed in this section had an initial perturbation wavelength equal to 25 mm.

Figure 4.1 shows the result from the shock loading of a 1.2-mm-thick sample with an initial perturbation amplitude equal to 2% of the initial perturbation wavelength (i.e., $\xi_0 = 0.02\lambda$). Figures 4.1b–e provide snapshots of the experiment at the indicated times, and Fig. 4.1f plots the experimental amplitude growth of the two crest/trough pairs monitored using PDV. The

experimental amplitude growth plot was obtained first by integrating the velocity spectrograms recorded by the PDV probes to obtain the displacement of the monitored crests and troughs, following which the amplitude growth was computed by taking the halved difference between the paired crest and trough, that is, Amplitude Growth $(t) = (x_{\text{crest}}(t) - x_{\text{trough}}(t))/2$. More on PDV data processing and how velocity histories (and subsequently displacements) are extracted from spectrogram readings can be found in Section 3.3 of this thesis as well as in Refs. [98, 100, 101]. Figure 4.1f displays appreciably exponential trends for both crest/trough pairs with the total duration of the experiment being of 530 µs. Of note is the appearance of additional protrusions on the surface of the sample seen in Figs. 4.1d–e.

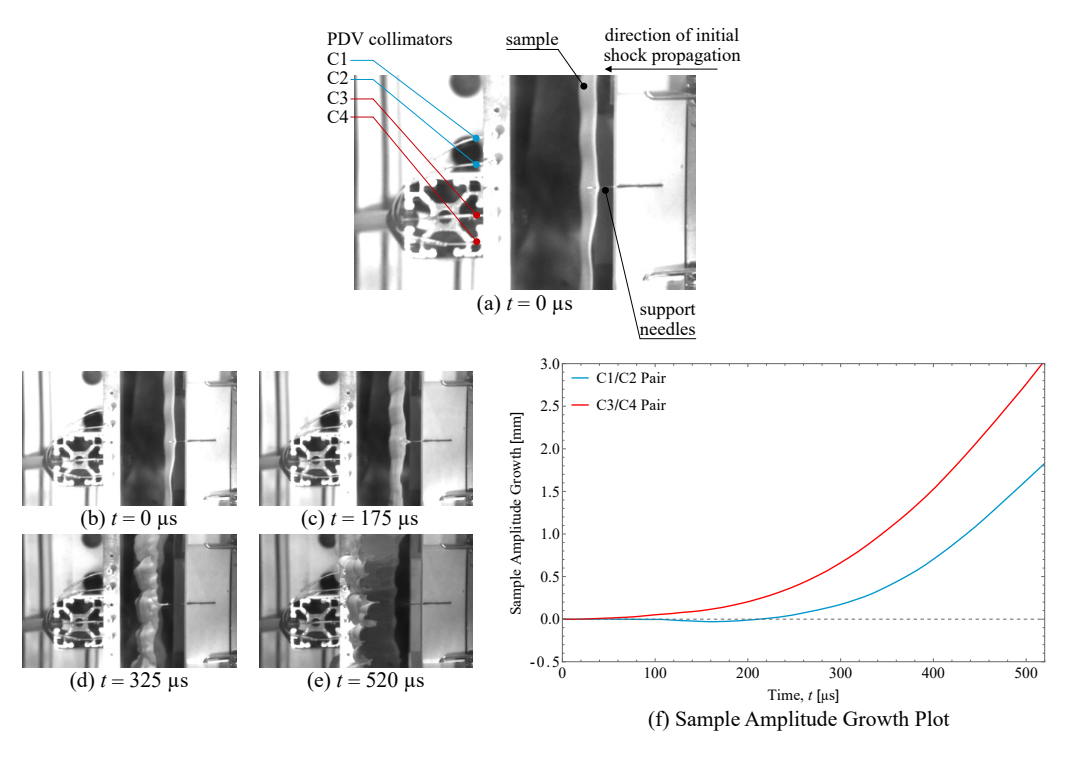


Figure 4.1: Shock loading of a 1.2-mm-thick Ecoflex 00-30 sample with $\lambda = 25 \,\mathrm{mm}$ and $a_0 = 0.02\lambda$: (a) provides an enlarged and labeled view of the first snapshot, (b)–(e) show snapshots of the experiment at labeled times, and (f) shows the amplitude growth of the sample obtained using PDV.

Figure 4.2 shows the result of the shock loading of a 1.2-mm-thick sample with a relatively larger initial perturbation amplitude equal to 10% of the initial perturbation wavelength (i.e., $\xi_0 = 0.1\lambda$). The total duration of this experiment was of 550 µs, and Fig. 4.2e displays an amplitude growth trend that differs from that of an exponential with the amplitude

growth seemingly reaching a plateau towards the end of the experiment. This sample with a relatively larger perturbation amplitude also appears to experience a cusping or pinching of its troughs which is most readily seen in Figs. 4.2c–d. It is suspected that as the initial perturbation amplitude of a sample is increased, the troughs of the sample start acting as imploding semi-cylinders following shock loading, generating additional buckling modes of failure. This sample also saw the appearance of protrusions on its surface (Figs. 4.2c–d).

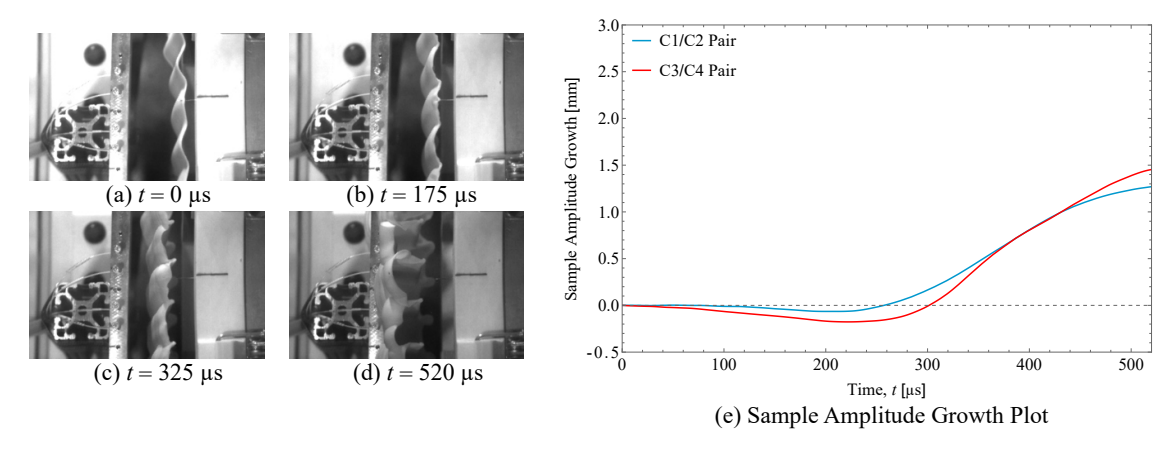


Figure 4.2: Shock loading of a 1.2-mm-thick Ecoflex 00-30 sample with $\lambda = 25 \,\mathrm{mm}$ and $\xi_0 = 0.10\lambda$: (a)–(d) show snapshots of the experiment at labeled times and (e) shows the amplitude growth of the sample obtained using PDV.

The shock loading of a 3.1-mm-thick sample whose initial perturbation amplitude was $\xi_0 = 0.02\lambda$ is shown in Fig. 4.3. While the amplitude growth trends described in Fig. 4.3e appear exponential, the total duration of this experiment was of 934 µs with the total amplitude growth being significantly smaller than that of the 1.2-mm-thick sample with $\xi_0 = 0.02\lambda$. This indicates that the thicker 3.1 mm sample experienced a slower perturbation growth rate. This thicker sample displayed no emergence of protrusions on its surface.

A 6.1-mm-thick Ecoflex 00-30 sample with an initial perturbation amplitude $\xi_0 = 0.10\lambda$ is shown in Fig. 4.4. The duration of this experiment was of 1045 µs, although the final amplitude growth of this 6.1-mm-thick sample displayed by Fig. 4.4e was significantly larger than that of the 3.1-mm-thick sample previously discussed. Of note is the prominent presence of the cusping of the sample troughs as seen in Figs. 4.4c–d. This thicker sample also displayed no emergence of protrusions on its surface.

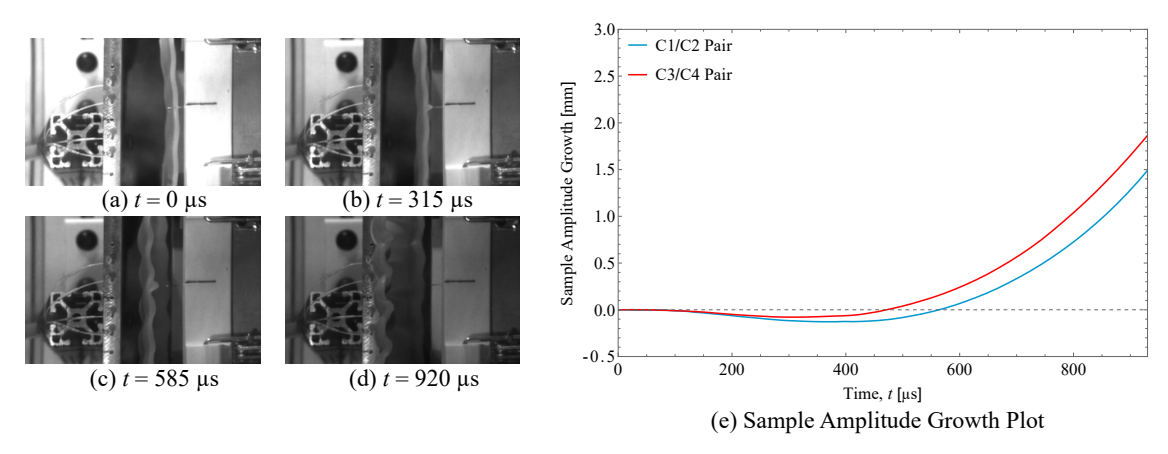


Figure 4.3: Shock loading of a 3.1-mm-thick Ecoflex 00-30 sample with $\lambda = 25 \,\mathrm{mm}$ and $\xi_0 = 0.02\lambda$: (a)–(d) show snapshots of the experiment at labeled times and (e) shows the amplitude growth of the sample obtained using PDV.

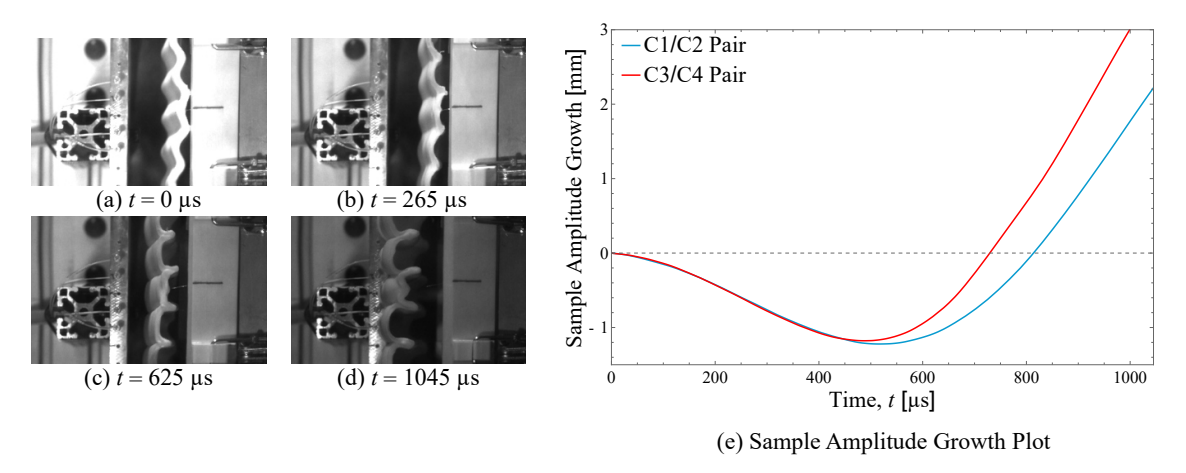


Figure 4.4: Shock loading of a 6.1-mm-thick Ecoflex 00-30 sample with $\lambda = 25 \,\mathrm{mm}$ and $\xi_0 = 0.10\lambda$: (a)–(d) show snapshots of the experiment at labeled times and (e) shows the amplitude growth of the sample obtained using PDV.

4.2 Theoretical and Experimental Growth Rates

A curve fitting of the amplitude growth trend experienced by the 1.2-mm-thick sample with $\xi_0 = 0.02\lambda$ lamb is shown in Fig. 4.5. The exponential curve fitting yields an experimental growth rate equal to $9421\,\mathrm{s}^{-1}$. Numerically solving Eq. (2.2) for the growth rate, γ , using $h = 1.2\,\mathrm{mm}$ and the Ecoflex 00-30 material properties $G = 27\,\mathrm{kPa}$ and $\rho = 1070\,\mathrm{kg/m^3}$ [94, 97], the theoretical growth predicted by RTI for this sample is found to equal $8713\,\mathrm{s}^{-1}$. While similar agreement between theory and experiment was found for the 3.1-mm-thick sample, no such agreement was obtained for the 1.2-mm-thick and 6.1-mm-thick samples with $\xi_0 = 0.1\lambda$ because their amplitude growth trend significantly differed from exponential behavior.

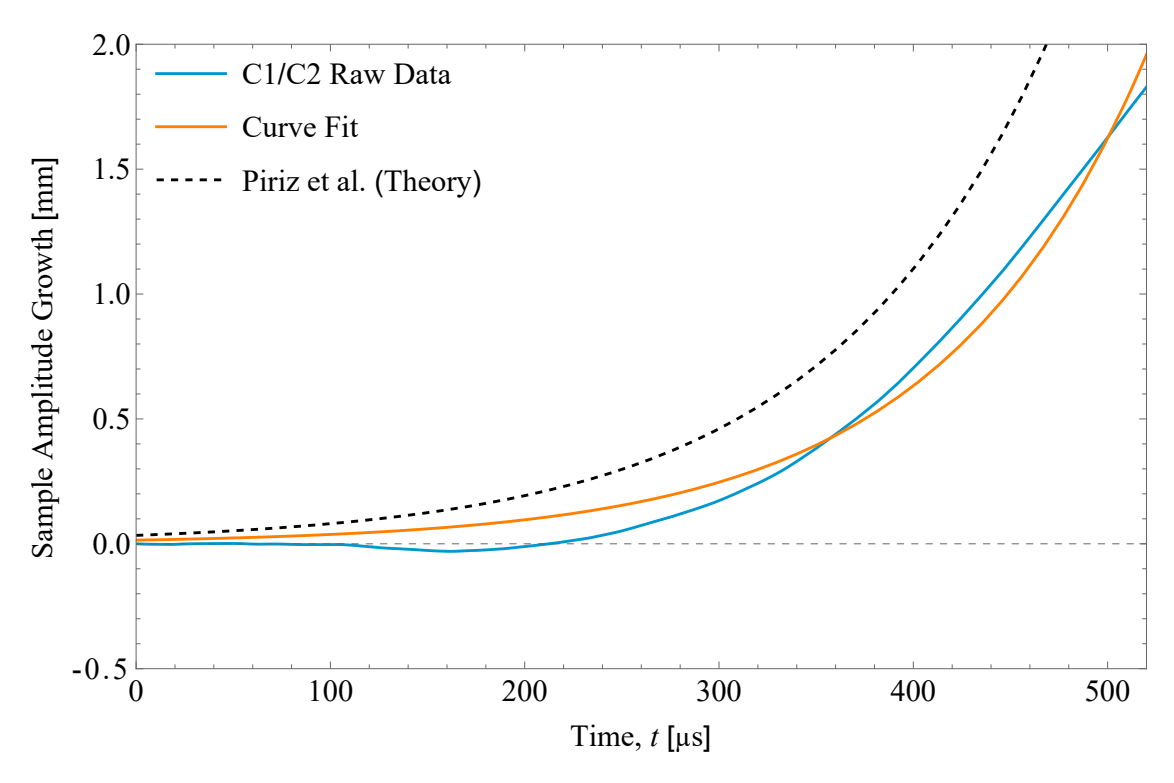
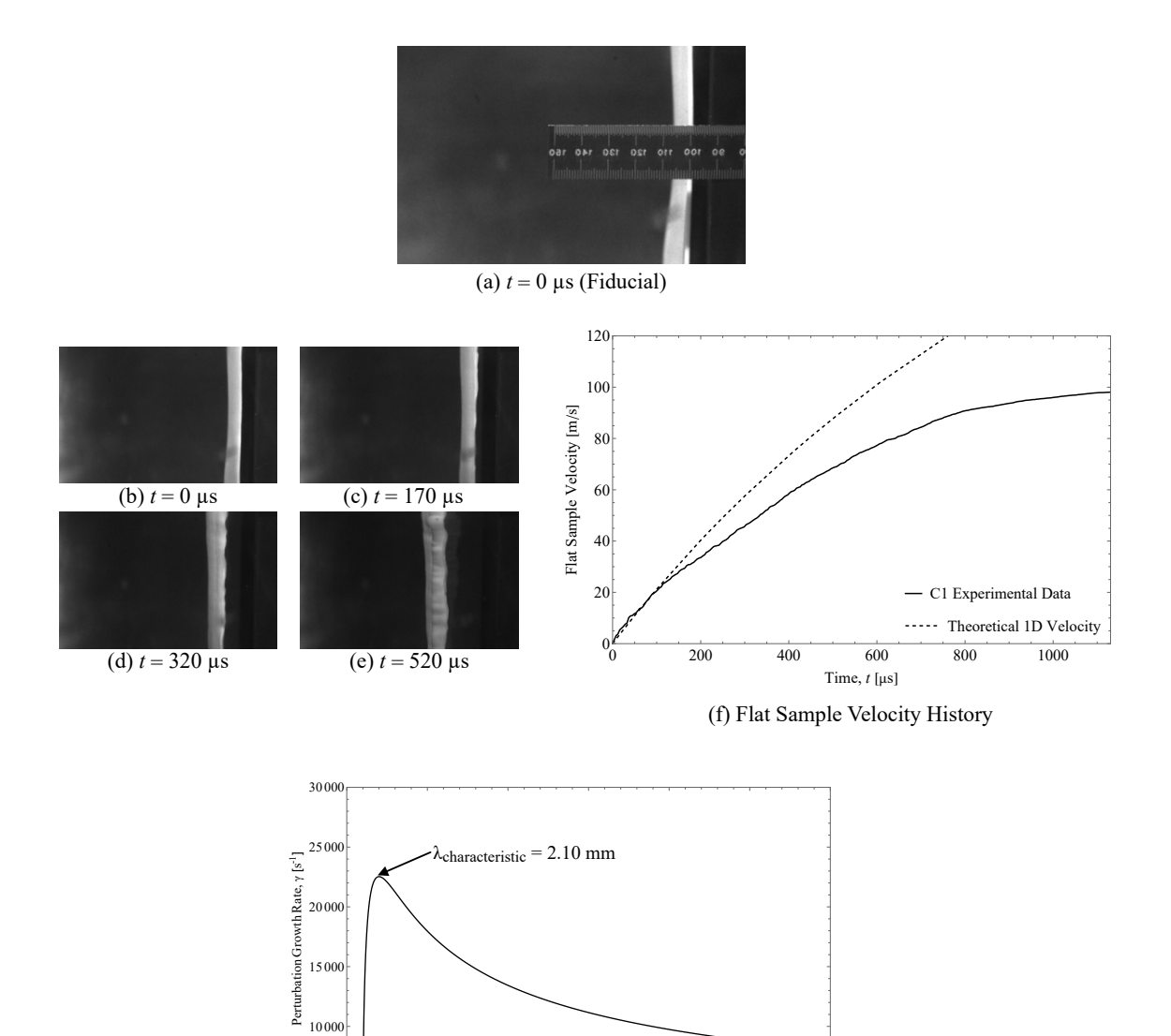


Figure 4.5: Comparison between the curve-fitted experimental growth rate of the 1.2-mm-thick Ecoflex 00-30 sample with $\lambda = 25 \,\mathrm{mm}$ and $\xi_0 = 0.02\lambda$ and the theoretical growth of the same sample predicted by RTI.

4.3 Shock Loading Flat Ecoflex 00-30 Samples

To further investigate the appearance of protrusions on the surface of the thinner sinusoidally perturbed samples, flat samples of different thicknesses were also shock loaded. As the samples were flat, only one PDV probe was used to record the bulk velocity history of each sample. The initial distance between the PDV probe and the samples studied was set to 120 mm as this was found to be the largest distance over which the PDV laser light can reliably provide velocity history readings. Although the flat sample experiments consequently end up lasting longer than the previously discussed experiments, the snap shots of each flat sample below are shown for similar times to the ones displayed for the sinusoidally perturbed samples. This is to allow for a more appropriate visual comparison between the flat samples and the sinusoidally perturbed samples.

Figures 4.6b—e display snapshots of the shock loading of a representative 1.7-mm-thick flat sample loaded by a 1.47 Mach shock wave. Protrusions can be seen on the surface of the sample in Fig. 4.6e. Using a fiducial ruler positioned in the field of view right before the shot was performed (Fig. 4.6a), digital image data-postprocessing indicates that the distance between two adjacent protrusions (which visually form crests and troughs) ranges between 2.5 mm to 5.0 mm, a range similar in value to the RTI characteristic wavelength (i.e., maximum growth rate wavelength) predicted by theory of $\lambda_{\text{characteristic}} = 2.10 \,\text{mm}$. Figure 4.6g shows a theoretical plot of the growth rate as a function of the perturbation wavelength obtained using Eq. (2.2) with $G = 27 \,\mathrm{kPa}$ and $\rho = 1070 \,\mathrm{kg/m^3}$. It is thus suspected that the protrusions seen on the surface of the 1.7-mm-thick samples are a consequence of the emergence of the Rayleigh-Taylor characteristic wavelength of these samples. Figure 4.6f also compares the velocity history experimental data of this sample to the velocity history predicted by the numerical integration of Eq. (2.13)—the same parameters used to compute the Rayleigh-Taylor characteristic wavelength of this sample were used to compute this theoretical velocity curve. Although the theoretical and experimental velocity histories appear to agree at the onset of the experiment, following the $t = 200 \,\mu s$ mark significant discrepancy between the two curves is observed. As the experimental velocity curve indicates a slower sample than the one predicted by theory, the discrepancy between theory and experiment is here suspected to be caused by the fact that the edges of the solid samples were not confined during their acceleration, causing the accelerating gases to vent around the edges of the samples into the environment thereby reducing the final acceleration of the samples.



(g) Theoretical Growth Rate as a Function of Perturbation Wavelength

Figure 4.6: Shock loading of a flat (i.e., no imposed perturbations) 1.7-mm-thick Ecoflex 00-30 sample: (a) shows the fiducial ruler used to allow for the calibration of the image pixels; (b)–(e) show snapshots of the experiment at labeled times; (f) plots the theoretical 1D velocity history of this sample alongside the experimental velocity history of the sample obtained via PDV; and (g) shows the theoretical growth rate of the sample as a function of perturbation wavelength—the wavelength for which theory predicts a maximum growth rate is equal to 2.10 mm.

Figures 4.7 shows the results of shock loading a representative 3.8-mm-thick flat sample using a 1.47 Mach shock wave. While Figs. 4.7c-d show some ripples forming at the top edge of the 3.8-mm-thick flat sample, no surface protrusions where observed. Figure 4.7e shows a comparison between the experimental and theoretical velocity history of this sample. Once more the experimental velocity history displays a sample that does not accelerate as fast as was predicted by theory with a velocity plateau starting to form towards the end of the experiment duration.

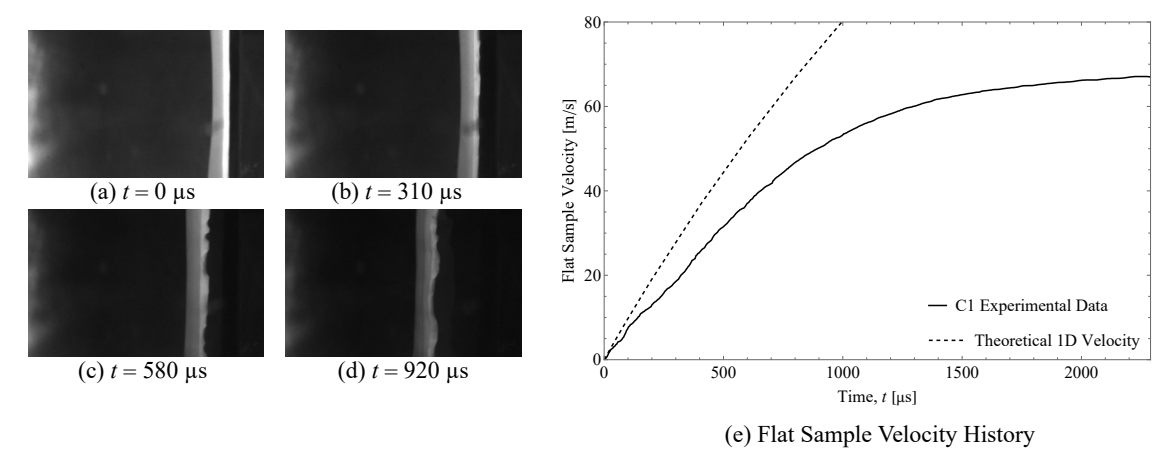


Figure 4.7: Shock loading of a flat (i.e., no imposed perturbations) 3.8-mm-thick Ecoflex 00-30 sample: (a)–(d) show snapshots of the experiment at labeled times and (e) plots the theoretical 1D velocity history of this sample alongside the experimental velocity history of the sample obtained via PDV

A representative 6.8-mm-thick flat sample loaded using a 1.44 Mach shock wave is shown in Fig. 4.8. As with the 3.8-mm-thick Ecoflex 00-30 sample, no surface protrusions were observed although some ripples did form on the top edge of this thicker sample (see Fig. 4.8c-d). Fig. 4.8e shows significant agreement between the theoretical and experimental velocity histories of this 6.8-mm-thick flat sample until the $t=500\,\mu s$ mark. After $t=500\,\mu s$, the experimental velocity curve once more falls below the velocity curve predicted by 1D theory.

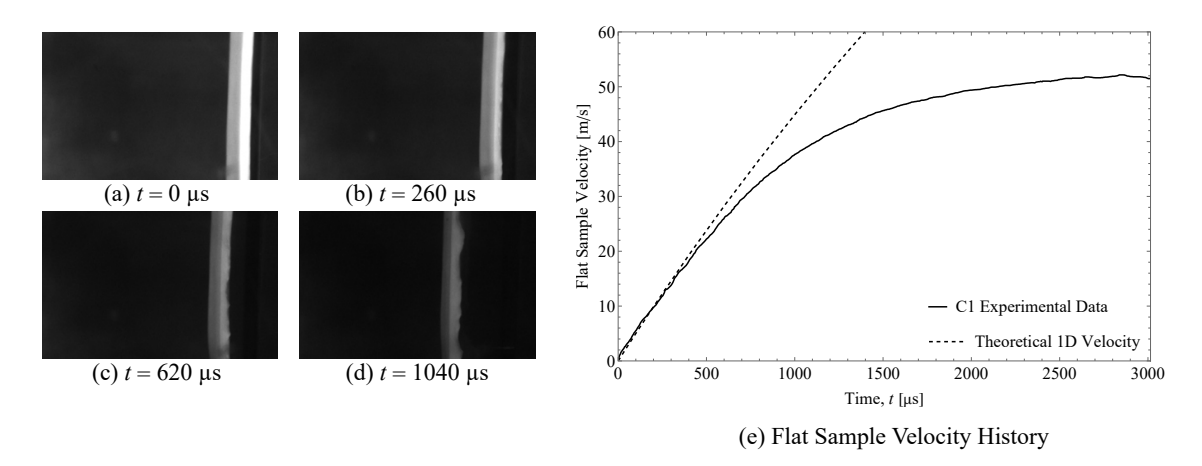


Figure 4.8: Shock loading of a flat (i.e., no imposed perturbations) 6.8-mm-thick Ecoflex 00-30 sample: (a)–(d) show snapshots of the experiment at labeled times and (e) plots the theoretical 1D velocity history of this sample alongside the experimental velocity history of the sample obtained via PDV

4.4 Shock Loading Sinusoidally Perturbed Stiff Samples

The sinusoidally perturbed samples discussed so far all displayed significant perturbation amplitude growth. This indicates that the Ecoflex 00-30 sinusoidally perturbed samples described above display interfacial instability. In an attempt to record sinusoidally perturbed samples that display interfacial stability, several 6.0-mm-thick samples were cast using materials significantly stiffer than Ecoflex 00-30. This section describes experiments performed using three such materials, each cast into a sinusoidally perturbed solid sample with $\lambda = 12 \,\mathrm{mm}$ and $\xi_0 = 0.10\lambda$. Of note is that the RTI dispersion relation (2.2) predicts purely imaginary γ values for RTI stable configurations. That γ is purely imaginary in the stable regime indicates that the RTI stable elastic solids should see their initial perturbation amplitude oscillate such that what originally were interfacial crests would eventually turn into interfacial troughs. To more readily observe such RTI stable oscillations, the stiffer samples were perturbed with an initial wavelength $\lambda = 12 \,\mathrm{mm}$ as it was found through the repeated numerical solving of Eq. (2.2) that RTI predicts stable samples with a smaller initial perturbation wavelength to display larger amplitude frequencies of oscillation. An initial perturbation amplitude $\xi_0 = 0.10\lambda$ was used to more readily allow for the visual observation of the evolution of the sample perturbation amplitude as, owing to the potential of crosstalk between PDV probes when aligned to the smaller $\lambda = 12 \,\mathrm{mm}$ [101], no PDV data acquisition was performed for the following stiff samples. All of the experiments described below were video recorded using a $50\,000$ fps frame rate.

Figures 4.9a–d show snapshots of a 6.2-mm-thick Solaris sample loaded using a 1.47 Mach shock wave. Solaris is another silicone elastomer manufactured by Smooth-On Inc. This silicone elastomer, however, is reported to be nearly four times as stiff as Ecoflex 00-30 with the elastic shear modulus reported in the literature for this material being equal to 120 kPa [94]. While this sample visually appears to display no significant perturbation amplitude growth, no oscillation of the perturbation amplitude was observed. Interestingly, the sample appears to billow midway through the experiment (Figs. 4.9c–d)

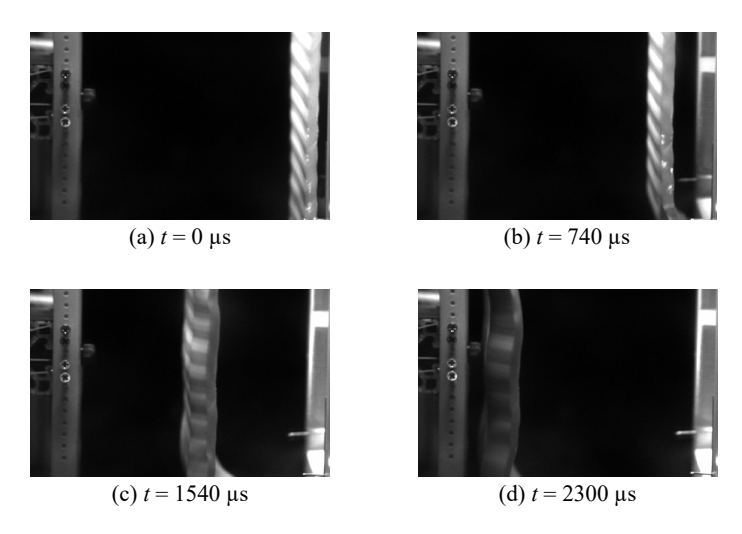


Figure 4.9: Shock loading of a 6.2-mm-thick Solaris sample with $\lambda = 12$ mm and $\xi_0 = 0.10\lambda$: (a)–(d) show snapshots of the experiment at labeled times.

The loading of a 6.3-mm-thick Sylgard 184 sample with a 1.57 Mach shock wave is shown in Figures 4.10a–d. The Sylgard 184 material, manufactured by Dow Corning, is even stiffer than the Solaris material with a reported elastic shear modulus equal to 620 kPa hence the use of a stronger loading shock wave. As for the 6.2-mm-thick Solaris sample, this 6.3-mm-thick Sylgard 184 sample visually displayed no significant perturbation amplitude growth and no apparent oscillation of the perturbation amplitude was observed. The Sylgard 184 sample also billowed during the later part of the experiment as shown in Figs. 4.10c–d.

Finally, the shock loading of a 6.4-mm-thick sample produced using the material Vytaflex 60 is shown in Figures 4.11a–d. This sample was loaded using a 1.59 Mach shock wave. Vytaflex 60 is a urethane material manufactured by Smooth-On Inc. Although no direct

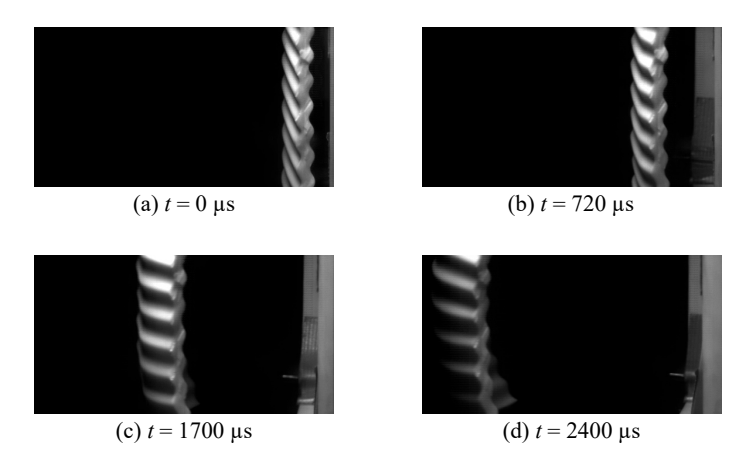


Figure 4.10: Shock loading of a 6.3-mm-thick Sylgard 184 sample with $\lambda = 12 \,\text{mm}$ and $\xi_0 = 0.10\lambda$: (a)–(d) show snapshots of the experiment at labeled times.

measurements of the elastic shear modulus of Vytaflex 60 was found in the literature, Li et al. have reported the Young's modulus of Vytaflex 60 to be equal to $2.068\,\mathrm{MPa}$. Because the shear modulus and the Young's modulus in a Hookean material are related via G=E/3, the shear modulus of Vytaflex 60 can be taken as $G=2.068\,\mathrm{MPa/3}=689\,\mathrm{kPa}$ when the material is in its linear elastic regime. This Vytaflex 60 sample also visually showed no significant perturbation amplitude growth following its shock loading while displaying no oscillations of its perturbation amplitude. Figures 4.11c–d show that this 6.4-mm-thick Vytaflex 60 sample also started billowing during the later parts of the experiment.

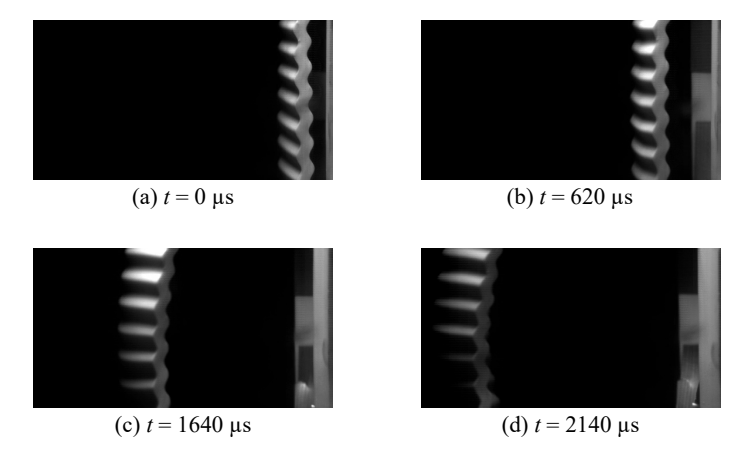


Figure 4.11: Shock loading of a 6.4-mm-thick Vytaflex60 sample with $\lambda = 12 \, \text{mm}$ and $\xi_0 = 0.10\lambda$: (a)–(d) show snapshots of the experiment at labeled times.

4.5 Discussion

The experiments examining the shock loading of sinusoidally perturbed solid samples described in this thesis are positioned on their respective RTI theoretical stability map in Fig. 4.12. All of the sinusoidally perturbed Ecoflex 00-30 samples displayed both qualitative (from video recordings) and quantitative (from PDV recorded amplitude growth data) unstable interfacial behavior as was shown in Figs. 4.1–4.4, as predicted by RTI theory. In the absence of PDV recordings, the sinusoidally perturbed samples manufactured from the stiffer Solaris, Sylgard 184, and Vytaflex 60 materials all displayed at least quantitative interfacial stability as no significant visual perturbation amplitude growth was observed (Figs. 4.9–4.11). Figs. 4.12b–d show that the samples manufactured using stiffer materials all lie in the stable region of their respective RTI map. This indicates that the experimental setup employed throughout this thesis is at least capable of qualitatively reproducing RTI behavior in elastic solids.

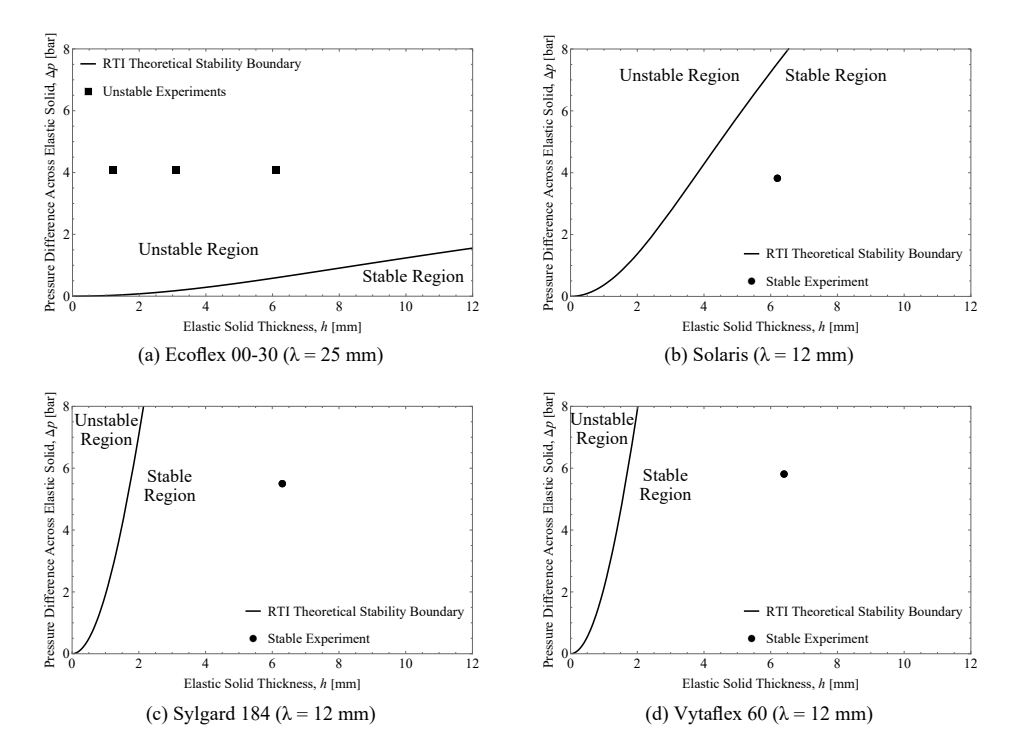


Figure 4.12: Plot of the experimental data points described in this thesis on their corresponding RTI stability map in the Δp -h space: (a) plot of the Ecoflex 00-30 data points; (b) plot of the Solaris data point; (c) plot of the Sylgard 184 data point; and (d) plot of the Vytaflex 60 data point.

Of important note, however, is the cusping of the Ecoflex 00-30 samples with the larger initial perturbation amplitude of $\xi_0 = 0.10\lambda$ (Figs. 4.2 and 4.4). The linear RTI for elastic solids does not provide much information on the influence of the amplitude size upon the behavior of the perturbed solid/fluid interface. As previously discussed, it is here believed that as the initial perturbation amplitude grows in size, the troughs of the elastic solids start acting as imploding cylinders following the shock loading of the solid, thereby generating additional modes of buckling failure. In a previous work by the author, an analytical stability boundary for a sinusoidally perturbed thin solid subjected to radiation pressure loads was derived via buckling theory [103]. Adapting the analytical treatment performed in the Theoretical Considerations Section of Ref. [103] to the scenario of a linear elastic, sinusoidally perturbed thin solid accelerated by a pressure difference of an arbitrary source generates the following buckling stability boundary:

$$\Delta p = \frac{2\pi^2 h^3}{\lambda^3} \frac{G}{\eta} \tag{4.1}$$

where $\eta = \xi_0/\lambda$ represents the ratio of the initial perturbation amplitude to the initial perturbation wavelength.

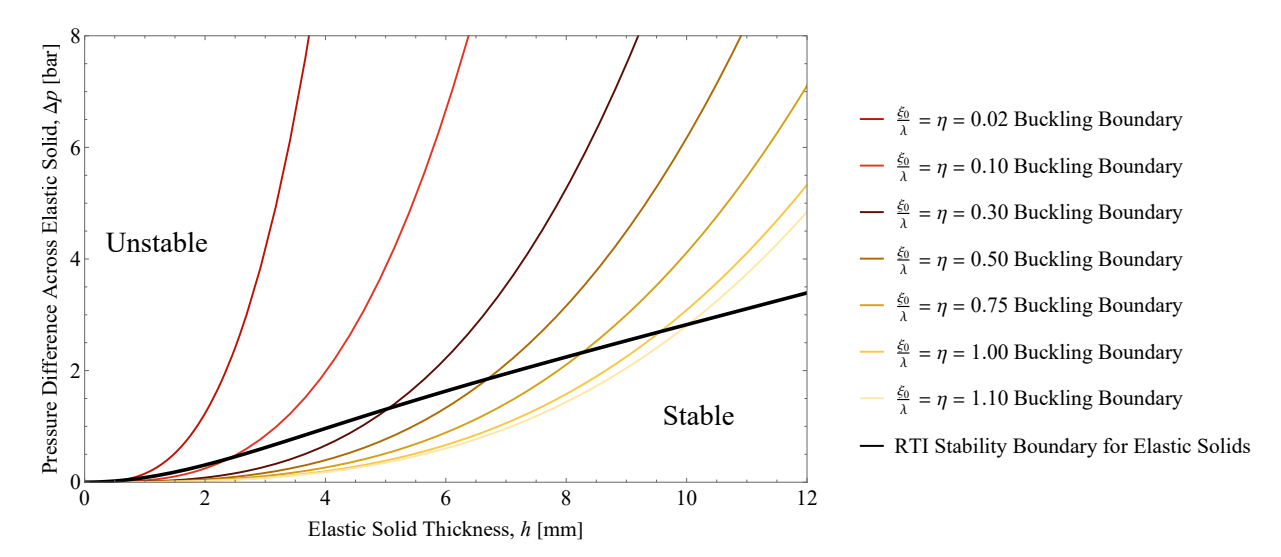


Figure 4.13: Buckling stability boundaries (adapted from [103]) plotted using different $\eta = \xi_0/\lambda$ values alongside the RTI stability boundary for Ecoflex 00-30 with $\lambda = 12$ mm.

Equation (4.1) is plotted in Fig. 4.13 using different values of η for Ecoflex 00-30 ($G=27\,\mathrm{kPa}$) with $\lambda=12\,\mathrm{mm}$ alongside the RTI stability boundary of the same elastic solid in the Δp -h space—stability lies to the left of each plotted boundary and vice versa. Figure 4.13 displays regions where, for a given value of η , an overlap between the unstable (stable) buckling region and stable (unstable) RTI region exists, predicting the possibility of scenarios where an accelerated elastic solid with a sinusoidally perturbed surface may be RTI stable and buckling unstable or vice versa. Figure 4.13 may act as a guideline for the development of experiments that may help further investigate the interplay between RTI theory and buckling theory. The author further notes that the emergence of buckling phenomena has also been noted within the literature studying the RTI behavior of confined soft gels subjected to their own gravity [86, 89, 104].

While, in general, the thicker sinusoidally perturbed Ecoflex 00-30 samples displayed slower growth rates than the relatively thinner perturbed samples, what is of note is the rapid ramp up in amplitude growth of the 6.1-mm-thick Ecoflex 00-30 sample with an initial perturbation amplitude $\xi_0 = 0.10\lambda$ towards the end of its acceleration phase (Fig. 4.4e). Given the prominent cusping of the troughs of this 6.1-mm-thick sample, it is unclear exactly what surface velocity the PDV probes are measuring. Following the onset of trough cusping, are the PDV probes initially aligned with the sample troughs measuring the velocity of the trough center, or are the PDV probes measuring the velocity of the sample material being dragged by the cusping troughs? To allow for a quantitative comparison between the video recordings and the PDV data, the author recommends that future experiments employ digital image correlation (DIC) to extract strain and strain rate data from the digital images produced by the video recordings. DIC would allow to verify the PDV experimental velocity histories against the high-speed videography data.

It was also noted in Section 4.4 that PDV data acquisition was not performed during the shock loading of the $\lambda=12\,\mathrm{mm}$ samples owing to the potential of crosstalk between the PDV probes when aligned to this relatively smaller λ . However, discussions with Dolan [105] indicates that there is theoretically no reason for the positioning of multiple, frequency shifted PDV probes next to each other in a fashion akin to line VISAR¹ not to provide an accurate means of velocity data acquisition. Ensuring that the input laser wavelength differs by more than a 0.5 nm between closely adjacent probes should avoid the occurrence of

¹VISAR, the precursor to PDV, stands for velocity interferometer system for any reflector [98].

crosstalk [101]. Upgrading the PDV apparatus described in Section 3.3 by adding frequency multiplexing photonic components in each of the four PDV channels should allow for the construction of a robust line PDV setup. To the best of the author's knowledge, this would provide the shock community with a first pilot study on the effectiveness of line PDV for acquiring velocity data along a single line of a shock accelerated free surface.

The velocity data acquired via PDV during the shock loading of the flat samples described in Section 4.3 indicates that the acceleration rates of the solids investigated throughout this thesis were slower than the ones predicted by the 1D theory described in Section 2.2.2 of this thesis. It is suspected that the acceleration rate of the shock loaded solids can be increased by modifying the sample holder flange positioned at the open end of the shock tube to allow for the confinement of the edges of the elastic solid during the acceleration phase. This edge confinement should stop the accelerating gases from seeping away from the sample surface, thereby increasing the acceleration rates of the solid samples.

On a final note, the elastic shear moduli values used throughout this thesis for the silicone elastomers were obtained in the literature via low-frequency rheometer techniques. To help further increase the accuracy of quantitative data reported in this thesis, the author also recommends the construction of a method for the direct measurement of the elastic shear modulus during high material strain rates. This is because soft materials such as Sylgard 184 are known to stiffen when undergoing high-strain rate deformations [106].

Chapter 5

Conclusions

5.1 Summary

A novel method for the experimental investigation of Rayleigh-Taylor instability in an elastic solid using a benchtop shock tube has been developed. Current findings indicate the formation of buckling modes of failure at the troughs of unstable samples with relatively large initial perturbation amplitude ($\xi_0=0.1\lambda$). The experimental growth rate of thinner samples also appears significantly greater than the experimental growth rate of thicker samples. Data post-processing and curve fitting indicates agreement between the experimentally observed growth rates of samples with a small initial perturbation amplitude ($\xi_0=0.02\lambda$) and the growth rates predicted by Rayleigh-Taylor theory. The relatively thinner, 1.7-mm-thick samples that did not have an initial perturbation also appear to exhibit the emergence of their characteristic RTI wavelength on their surface in the form of protrusions following their shock loading. Sinusoidally perturbed solid samples cast using the relatively stiffer materials were also shock loaded and the video recordings of these samples indicated no significant perturbation amplitude growth as predicted by RTI theory. The stiffer, stable samples, however, did not display the oscillations of their perturbation amplitude that RTI theory also predicts.

5 Conclusions 46

5.2 Future Work

To help improve the quantitative RTI analysis provided by the experimental methods described in this thesis, the following future implementations, discussed in greater detail in Section 4.5, are recommended:

- Digital image correlation should be performed to obtain strain and strain rate data from the high-speed videography data. This will allow for a more quantitative comparison between the video recordings and the PDV velocity data.
- The PDV apparatus should be upgraded with frequency multiplexing photonic component to create a line PDV setup. This will help employ PDV data acquisition during the shock loading of samples with smaller initial perturbation wavelengths without the occurrence of crosstalk between adjacent PDV probes.
- The solid sample holder attached to the open-end of the shock tube should be modified to allow for the confinement of the solid sample edges thereby increasing the acceleration rates of the shock loaded elastic solids.
- A method for the direct measurement of the elastic shear modulus of the materials used throughout this thesis during high strain rates should be developed.

Implementation of the above suggestions will permit a more robust quantitative experimental investigation of RTI theory in elastic solids.

- [1] John William Strutt. Investigation of the Character of the Equilibrium of an Incompressible Heavy Fluid of Variable Density. *Proceedings of the London Mathematical Society*, s1-14(1):170–177, 1882. doi:10.1112/plms/s1-14.1.170.
- [2] Sir Horace Lamb. *Hydrodynamics*. Dover Publications, 1932. URL: https://store.doverpublications.com/0486602567.html.
- [3] Geoffrey Ingram Taylor. The instability of liquid surfaces when accelerated in a direction perpendicular to their planes. I. *Proceedings of the Royal Society of London. Series A. Mathematical and Physical Sciences*, 201(1065):192–196, March 1950. Publisher: Royal Society. doi:10.1098/rspa.1950.0052.
- [4] D. J. Lewis and Geoffrey Ingram Taylor. The instability of liquid surfaces when accelerated in a direction perpendicular to their planes. II. *Proceedings of the Royal Society of London. Series A. Mathematical and Physical Sciences*, 202(1068):81–96, June 1950. Publisher: Royal Society. doi:10.1098/rspa.1950.0086.
- [5] W. J. Harrison. The Influence of Viscosity on the Oscillations of Superposed Fluids. *Proceedings of the London Mathematical Society*, s2-6(1):396–405, 1908. doi:10.1112/plms/s2-6.1.396.
- [6] Richard Bellman and Ralph H. Pennington. Effects of surface tension and viscosity on Taylor instability. Quarterly of Applied Mathematics, 12(2):151–162, 1954. doi: 10.1090/qam/63198.
- [7] R. Menikoff, R. C. Mjolsness, D. H. Sharp, and C. Zemach. Unstable normal mode for Rayleigh–Taylor instability in viscous fluids. *The Physics of Fluids*, 20(12):2000–2004, December 1977. doi:10.1063/1.861831.

[8] R. Menikoff, R. C. Mjolsness, D. H. Sharp, C. Zemach, and B. J. Doyle. Initial value problem for Rayleigh–Taylor instability of viscous fluids. *The Physics of Fluids*, 21(10):1674–1687, October 1978. doi:10.1063/1.862107.

- [9] M. Mitchner and R. K. M. Landshoff. Rayleigh-Taylor Instability for Compressible Fluids. *The Physics of Fluids*, 7(6):862–866, June 1964. doi:10.1063/1.1711297.
- [10] Milton S. Plesset and Din-Yu Hsieh. General Analysis of the Stability of Superposed Fluids. *The Physics of Fluids*, 7(8):1099–1108, August 1964. doi:10.1063/1.1711348.
- [11] G. H. Wolf. The dynamic stabilization of the Rayleigh-Taylor instability and the corresponding dynamic equilibrium. *Zeitschrift für Physik A Hadrons and nuclei*, 227(3):291–300, June 1969. doi:10.1007/BF01397662.
- [12] C. T. Chang. Dynamic Instability of Accelerated Fluids. *The Physics of Fluids*, 2(6):656–663, November 1959. doi:10.1063/1.1705969.
- [13] Martin David Kruskal, Martin Schwarzschild, and Subrahmanyan Chandrasekhar. Some instabilities of a completely ionized plasma. *Proceedings of the Royal Society of London. Series A. Mathematical and Physical Sciences*, 223(1154):348–360, 1954. doi:10.1098/rspa.1954.0120.
- [14] N K Gupta and S V Lawande. Effects of density gradients on Rayleigh-Taylor instability in an ablatively accelerated inertial confinement fusion target. *Plasma Physics and Controlled Fusion*, 28(1B):267–278, January 1986. doi:10.1088/0741-3335/28/1B/003.
- [15] Garrett Birkhoff. Note on Taylor instability. Quarterly of Applied Mathematics, 12(3):306–309, 1954. doi:10.1090/qam/65316.
- [16] Garrett Birkhoff. Stability of Spherical Bubbles. Quarterly of Applied Mathematics, 13(4):451–453, 1956. Publisher: Brown University. URL: https://www.jstor.org/stable/43634279.
- [17] M. S. Plesset. On the Stability of Fluid Flows with Spherical Symmetry. *Journal of Applied Physics*, 25(1):96–98, January 1954. doi:10.1063/1.1721529.

[18] Karnig O. Mikaelian. Normal Modes and Symmetries of the Rayleigh-Taylor Instability in Stratified Fluids. *Physical Review Letters*, 48(19):1365–1368, May 1982. Publisher: American Physical Society. doi:10.1103/PhysRevLett.48.1365.

- [19] Karnig O. Mikaelian. Rayleigh-Taylor instabilities in stratified fluids. *Physical Review A*, 26(4):2140–2158, October 1982. Publisher: American Physical Society. doi:10.1103/PhysRevA.26.2140.
- [20] Karnig O. Mikaelian. Time evolution of density perturbations in accelerating stratified fluids. *Physical Review A*, 28(3):1637–1646, September 1983. Publisher: American Physical Society. doi:10.1103/PhysRevA.28.1637.
- [21] Karnig O. Mikaelian. Rayleigh-Taylor and Richtmyer-Meshkov instabilities in multilayer fluids with surface tension. *Physical Review A*, 42(12):7211–7225, December 1990. Publisher: American Physical Society. doi:10.1103/PhysRevA.42.7211.
- [22] Karnig O. Mikaelian. Rayleigh-Taylor instability in finite-thickness fluids with viscosity and surface tension. *Physical Review E*, 54(4):3676–3680, October 1996. Publisher: American Physical Society. doi:10.1103/PhysRevE.54.3676.
- [23] S. Chandrasekhar. *Hydrodynamic and Hydromagnetic Stability*. Dover Publications, 1961. URL: https://store.doverpublications.com/048664071x.html.
- [24] G. Birkhoff. Taylor instability and laminar mixing. Technical Report LA-1862, Los Alamos National Lab. (LANL), Los Alamos, NM (United States), December 1954. doi:10.2172/4372366.
- [25] Robert L. Kiang. Nonlinear Theory of Inviscid Taylor Instability Near the Cutoff Wavenumber. *The Physics of Fluids*, 12(7):1333–1339, July 1969. doi:10.1063/1.1692672.
- [26] N. R. Rajappa. Non-Linear Theory of Taylor Instability of Superposed Fluids. *Journal of the Physical Society of Japan*, 28(1):219–224, 1970. doi:10.1143/JPSJ.28.219.
- [27] Ali Hasan Nayfeh. On the non-linear Lamb-Taylor instability. *Journal of Fluid Mechanics*, 38(3):619–631, September 1969. Publisher: Cambridge University Press. doi:10.1017/S0022112069000371.

[28] Edward Ott. Nonlinear Evolution of the Rayleigh-Taylor Instability of a Thin Layer. Physical Review Letters, 29(21):1429–1432, November 1972. Publisher: American Physical Society. doi:10.1103/PhysRevLett.29.1429.

- [29] E. Fermi and J. von Neumann. Taylor instability of incompressible liquids. Technical Report AECU-2979, Los Alamos National Laboratory (LANL), Los Alamos, NM (United States), August 1953. doi:10.2172/4373391.
- [30] W. P. Crowley. An empirical theory for large amplitude Rayleigh-Taylor instability. Technical Report UCRL-72650, California Univ., Livermore. Lawrence Radiation Lab., January 1970. URL: https://www.osti.gov/biblio/4603027.
- [31] L. Baker and J. R. Freeman. Heuristic model of the nonlinear Rayleigh-Taylor instability. *Journal of Applied Physics*, 52(2):655–663, February 1981. doi:10.1063/1.328793.
- [32] R. M. Davies and Geoffrey Ingram Taylor. The mechanics of large bubbles rising through extended liquids and through liquids in tubes. *Proceedings of the Royal Society of London. Series A. Mathematical and Physical Sciences*, 200(1062):375–390, February 1950. Publisher: Royal Society. doi:10.1098/rspa.1950.0023.
- [33] David Layzer. On the Instability of Superposed Fluids in a Gravitational Field. *The Astrophysical Journal*, 122:1, July 1955. doi:10.1086/146048.
- [34] Garrett Birkhoff and David Carter. Rising Plane Bubbles. *Journal of Mathematics and Mechanics*, 6(6):769–779, 1957. Publisher: Indiana University Mathematics Department. URL: https://www.jstor.org/stable/24900621.
- [35] P. R. Garabedian and Geoffrey Ingram Taylor. On steady-state bubbles generated by Taylor instability. *Proceedings of the Royal Society of London. Series A. Mathematical and Physical Sciences*, 241(1226):423–431, August 1957. Publisher: Royal Society. doi:10.1098/rspa.1957.0137.
- [36] D. H. Sharp. An overview of Rayleigh-Taylor instability. *Physica D: Nonlinear Phenomena*, 12(1):3–18, July 1984. doi:10.1016/0167-2789(84)90510-4.

[37] H. J. Kull. Theory of the Rayleigh-Taylor instability. *Physics Reports*, 206(5):197–325, August 1991. doi:10.1016/0370-1573(91)90153-D.

- [38] Ye Zhou. Rayleigh-Taylor and Richtmyer-Meshkov instability induced flow, turbulence, and mixing. I. *Physics Reports*, 720-722:1-136, December 2017. URL: https://www.sciencedirect.com/science/article/pii/S0370157317302028, doi:10.1016/j.physrep.2017.07.005.
- [39] Ye Zhou. Rayleigh-Taylor and Richtmyer-Meshkov instability induced flow, turbulence, and mixing. II. *Physics Reports*, 723-725:1–160, December 2017. doi: 10.1016/j.physrep.2017.07.008.
- [40] J. W. Miles. Taylor instability of a flat plate. Technical report, August 1966. Section: Technical Reports. URL: https://apps.dtic.mil/sti/citations/AD0643161.
- [41] Gregory N. White. A One-Degree-of-Freedom Model for the Taylor Instability of an Ideally Plastic Metal Plate. 1973. URL: https://www.osti.gov/servlets/purl/4479084.
- [42] Daniel C. Drucker. Iii "Taylor instability" of the surface of an elastic-plastic plate. In *Mechanics Today*, pages 37–47. Pergamon, 1980. doi:10.1016/B978-0-08-024249-1. 50013-3.
- [43] D. C. Drucker. A further look at Rayleigh-Taylor and other surface instabilities in solids. *Ingenieur-Archiv*, 49(5):361–367, August 1980. doi:10.1007/BF02426914.
- [44] John K. Dienes. Method of generalized coordinates and an application to Rayleigh–Taylor instability. *The Physics of Fluids*, 21(5):736–744, May 1978. doi: 10.1063/1.862291.
- [45] J. W. Swegle and Allen C. Robinson. Acceleration instability in elastic-plastic solids. I. Numerical simulations of plate acceleration. *Journal of Applied Physics*, 66(7):2838–2858, October 1989. doi:10.1063/1.344190.
- [46] Allen C. Robinson and J. W. Swegle. Acceleration instability in elastic-plastic solids. II. Analytical techniques. *Journal of Applied Physics*, 66(7):2859–2872, October 1989. doi:10.1063/1.344191.

[47] E. L. Ruden and D. E. Bell. Rayleigh—Taylor stability criteria for elastic-plastic solid plates and shells. *Journal of Applied Physics*, 82(1):163–170, July 1997. doi:10.1063/1.365795.

- [48] Guillermo Terrones. Fastest growing linear Rayleigh-Taylor modes at solid-fluid and solid-solid interfaces. *Physical Review E*, 71(3):036306, March 2005. Publisher: American Physical Society. doi:10.1103/PhysRevE.71.036306.
- [49] A. R. Piriz, J. J. López Cela, O. D. Cortázar, N. A. Tahir, and D. H. H. Hoffmann. Rayleigh-Taylor instability in elastic solids. *Physical Review E*, 72(5):056313, November 2005. Publisher: American Physical Society. doi:10.1103/PhysRevE.72.056313.
- [50] A. R. Piriz, J. J. López Cela, and N. A. Tahir. Linear analysis of incompressible Rayleigh-Taylor instability in solids. *Physical Review E*, 80(4):046305, October 2009. Publisher: American Physical Society. doi:10.1103/PhysRevE.80.046305.
- [51] A. R. Piriz, J. J. López Cela, and N. A. Tahir. Rayleigh-Taylor instability in elastic-plastic solids. *Journal of Applied Physics*, 105(11):116101, June 2009. doi:10.1063/1.3139267.
- [52] A. R. Piriz, Y. B. Sun, and N. A. Tahir. Rayleigh-Taylor stability boundary at solid-liquid interfaces. *Physical Review E*, 88(2):023026, August 2013. Publisher: American Physical Society. doi:10.1103/PhysRevE.88.023026.
- [53] A. R. Piriz, Y. B. Sun, and N. A. Tahir. Rayleigh-Taylor linear growth at an interface between an elastoplastic solid and a viscous liquid. *Physical Review E*, 89(6):063022, June 2014. Publisher: American Physical Society. doi:10.1103/PhysRevE.89. 063022.
- [54] Y. B. Sun and A. R. Piriz. Magneto-Rayleigh-Taylor instability in solid media. *Physics of Plasmas*, 21(7):072708, July 2014. doi:10.1063/1.4890569.
- [55] A. R. Piriz, Y. B. Sun, and N. A. Tahir. Hydrodynamic instability of elastic-plastic solid plates at the early stage of acceleration. *Physical Review E*, 91(3):033007, March 2015. Publisher: American Physical Society. doi:10.1103/PhysRevE.91.033007.

[56] A. R. Piriz, Y. B. Sun, and N. A. Tahir. Rayleigh-Taylor instability in accelerated solid media. European Journal of Physics, 38(1):015003, November 2016. Publisher: IOP Publishing. doi:10.1088/0143-0807/38/1/015003.

- [57] S. A. Piriz, A. R. Piriz, N. A. Tahir, S. Richter, and M. Bestehorn. Rayleigh-Taylor instability in elastic-plastic solid slabs bounded by a rigid wall. *Physical Review E*, 103(2):023105, February 2021. Publisher: American Physical Society. URL: https://link.aps.org/doi/10.1103/PhysRevE.103.023105, doi:10.1103/PhysRevE.103.023105.
- [58] A. R. Piriz, S. A. Piriz, and N. A. Tahir. Formation of spikes and bubbles in the linear phase of Rayleigh-Taylor instability in elastic-plastic media. *Physical Review* E, 107(3):035105, March 2023. Publisher: American Physical Society. doi:10.1103/ PhysRevE.107.035105.
- [59] Y. B. Sun, R. H. Zeng, and J. J. Tao. Elastic Rayleigh–Taylor and Richtmyer–Meshkov instabilities in spherical geometry. *Physics of Fluids*, 32(12):124101, December 2020. doi:10.1063/5.0027909.
- [60] Y. B. Sun, R. H. Zeng, and J. J. Tao. Effects of viscosity and elasticity on Rayleigh–Taylor instability in a cylindrical geometry. *Physics of Plasmas*, 28(6):062701, June 2021. doi:10.1063/5.0050629.
- [61] J. N. Gou, W. T. Zan, Y. B. Sun, and C. Wang. Linear analysis of Rayleigh-Taylor instability in viscoelastic materials. *Physical Review E*, 104(2):025110, August 2021. Publisher: American Physical Society. doi:10.1103/PhysRevE.104.025110.
- [62] Siyi An and Yongjun Jian. Rayleigh–Taylor instability of viscoelastic self-rewetting film flowing down a temperature-controlled inclined substrate. *Chinese Physics B*, 32(6):064701, June 2023. Publisher: Chinese Physical Society and IOP Publishing Ltd. doi:10.1088/1674-1056/acc78b.
- [63] Boris J. P. Kaus and Thorsten W. Becker. Effects of elasticity on the Rayleigh–Taylor instability: Implications for large-scale geodynamics. *Geophysical Journal International*, 168(2):843–862, February 2007. doi:10.1111/j.1365-246X.2006.03201.x.

[64] E. B. Burov and P. Molnar. Small and large-amplitude gravitational instability of an elastically compressible viscoelastic Maxwell solid overlying an inviscid incompressible fluid: Dependence of growth rates on wave number and elastic constants at low Deborah numbers. Earth and Planetary Science Letters, 275(3):370–381, November 2008. doi:10.1016/j.epsl.2008.08.032.

- [65] Weronika Gorczyk, Bruce Hobbs, and Taras Gerya. Initiation of Rayleigh-Taylor instabilities in intra-cratonic settings. *Tectonophysics*, 514-517:146-155, January 2012. doi:10.1016/j.tecto.2011.10.016.
- [66] Weronika Gorczyk and Katharina Vogt. Tectonics and melting in intra-continental settings. Gondwana Research, 27(1):196–208, January 2015. doi:10.1016/j.gr.2013. 09.021.
- [67] O. Blaes, R. Blandford, P. Madau, and S. Koonin. Slowly Accreting Neutron Stars and the Origin of Gamma-Ray Bursts. *The Astrophysical Journal*, 363:612, November 1990. ADS Bibcode: 1990ApJ...363..612B. doi:10.1086/169371.
- [68] O. M. Blaes, R. D. Blandford, P. Madau, and L. Yan. On the Evolution of Slowly Accreting Neutron Stars. The Astrophysical Journal, 399:634, November 1992. ADS Bibcode: 1992ApJ...399..634B. doi:10.1086/171955.
- [69] L. Suleiman, J. L. Zdunik, P. Haensel, and M. Fortin. Partially accreted crusts of neutron stars. *Astronomy & Astrophysics*, 662:A63, June 2022. Publisher: EDP Sciences. doi:10.1051/0004-6361/202243040.
- [70] John F. Barnes, Patrick J. Blewett, Robert G. McQueen, Kenneth A. Meyer, and Douglas Venable. Taylor instability in solids. *Journal of Applied Physics*, 45(2):727–732, 02 1974. doi:10.1063/1.1663310.
- [71] John F. Barnes, D. H. Janney, Roger K. London, Kenneth A. Meyer, and David H. Sharp. Further experimentation on Taylor instability in solids. *Journal of Applied Physics*, 51(9):4678–4679, 09 1980. doi:10.1063/1.328339.
- [72] S M Bakhrakh, O B Drennov, and N P Kovalev. Hydrodynamic instability in strong media. (10.2172/515973), 03 1997. doi:UCRL-CR-126710.

[73] Guy Dimonte, Robert Gore, and Marilyn Schneider. Rayleigh-Taylor instability in elastic-plastic materials. *Phys. Rev. Lett.*, 80:1212–1215, Feb 1998. doi:10.1103/PhysRevLett.80.1212.

- [74] Rinosh Polavarapu, Pamela Roach, and Arindam Banerjee. Rayleigh-Taylor-instability experiments with elastic-plastic materials. *Phys. Rev. E*, 99:053104, May 2019. doi: 10.1103/PhysRevE.99.053104.
- [75] D. H. Kalantar, B. A. Remington, J. D. Colvin, K. O. Mikaelian, S. V. Weber, L. G. Wiley, J. S. Wark, A. Loveridge, A. M. Allen, A. A. Hauer, and M. A. Meyers. Solid-state experiments at high pressure and strain rate. *Physics of Plasmas*, 7(5):1999–2006, May 2000. doi:10.1063/1.874021.
- [76] Xinbo Bai, Tao Wang, Yuxuan Zhu, and Guoqiang Luo. Expansion of Linear Analysis of Rayleigh-Taylor Interface Instability of Metal Materials. World Journal of Mechanics, 8(4):94–106, May 2018. Number: 4 Publisher: Scientific Research Publishing. doi:10.4236/wjm.2018.84008.
- [77] B. A. Remington, P. Allen, E. M. Bringa, J. Hawreliak, D. Ho, K. T. Lorenz, H. Lorenzana, J. M. McNaney, M. A. Meyers, S. W. Pollaine, K. Rosolankova, B. Sadik, M. S. Schneider, D. Swift, J. Wark, and B. Yaakobi. Material dynamics under extreme conditions of pressure and strain rate. *Materials Science and Technology*, 22(4):474–488, April 2006. doi:10.1179/174328406X91069.
- [78] Jonathan L Belof, R. M. Cavallo, Russel T. Olson, Robert S. King, George Thompson Gray III, David Holtkamp, Shuh-Rong Chen, R. E. Rudd, Nathan Barton, Athanasios Arsenlis, B. Remington, Hye-Sook Park, S. T. Prisbrey, Peter Vitello, Grant Bazan, Karnig O. Mikaelian, A. J. Comley, Brian Maddox, and M. J. May. Rayleigh-Taylor strength experiments of the pressure-induced phase transition in iron. AIP Conference Proceedings, 1426(1):1521–1524, March 2012. doi:10.1063/1.3686572.
- [79] Hye-Sook Park, K. T. Lorenz, R. M. Cavallo, S. M. Pollaine, S. T. Prisbrey, R. E. Rudd, R. C. Becker, J. V. Bernier, and B. A. Remington. Viscous Rayleigh-Taylor Instability Experiments at High Pressure and Strain Rate. *Physical Review Letters*, 104(13):135504, April 2010. Publisher: American Physical Society. doi:10.1103/PhysRevLett.104.135504.

[80] Hye-Sook Park, B. A. Remington, R. C. Becker, J. V. Bernier, R. M. Cavallo, K. T. Lorenz, S. M. Pollaine, S. T. Prisbrey, R. E. Rudd, and N. R. Barton. Strong stabilization of the Rayleigh-Taylor instability by material strength at megabar pressuresa). Physics of Plasmas, 17(5):056314, May 2010. doi:10.1063/1.3363170.

- [81] A. R. Piriz, J. J. López Cela, and N. A. Tahir. Comment on "Viscous Rayleigh-Taylor Instability Experiments at High Pressure and Strain Rate". *Physical Review Letters*, 105(17):179601, October 2010. Publisher: American Physical Society. doi: 10.1103/PhysRevLett.105.179601.
- [82] Hye-Sook Park, Nathan Barton, Jonathan L Belof, K. J. M. Blobaum, R. M. Cavallo, A. J. Comley, Brian Maddox, M. J. May, S. M. Pollaine, S. T. Prisbrey, B. Remington, R. E. Rudd, D. W. Swift, R. J. Wallace, M. J. Wilson, A. Nikroo, and E. Giraldez. Experimental results of tantalum material strength at high pressure and high strain rate. AIP Conference Proceedings, 1426(1):1371–1374, 03 2012. doi:10.1063/1.3686536.
- [83] Bruce A. Remington, Hye-Sook Park, Daniel T. Casey, Robert M. Cavallo, Daniel S. Clark, Channing M. Huntington, Dan H. Kalantar, Carolyn C. Kuranz, Aaron R. Miles, Sabrina R. Nagel, Kumar S. Raman, Christoper E. Wehrenberg, and Vladimir A. Smalyuk. Rayleigh—Taylor instabilities in high-energy density settings on the National Ignition Facility. *Proceedings of the National Academy of Sciences*, 116(37):18233—18238, September 2019. Publisher: Proceedings of the National Academy of Sciences. doi:10.1073/pnas.1717236115.
- [84] Serge Mora, Ty Phou, Jean-Marc Fromental, and Yves Pomeau. Gravity Driven Instability in Elastic Solid Layers. *Physical Review Letters*, 113(17):178301, October 2014. Publisher: American Physical Society. doi:10.1103/PhysRevLett.113.178301.
- [85] D. Riccobelli and P. Ciarletta. Rayleigh-Taylor instability in soft elastic layers. Philosophical Transactions of the Royal Society A: Mathematical, Physical and Engineering Sciences, 375(2093):20160421, April 2017. Publisher: Royal Society. doi: 10.1098/rsta.2016.0421.
- [86] Aditi Chakrabarti, Serge Mora, Franck Richard, Ty Phou, Jean-Marc Fromental, Yves Pomeau, and Basile Audoly. Selection of hexagonal buckling patterns by the elastic

- Rayleigh-Taylor instability. *Journal of the Mechanics and Physics of Solids*, 121:234–257, December 2018. doi:10.1016/j.jmps.2018.07.024.
- [87] Yue Zheng, Yang Lai, Yuhang Hu, and Shengqiang Cai. Rayleigh—Taylor instability in a confined elastic soft cylinder. *Journal of the Mechanics and Physics of Solids*, 131:221–229, October 2019. doi:10.1016/j.jmps.2019.07.006.
- [88] Saiful Islam Tamim and Joshua B. Bostwick. A dynamic analysis of the Rayleigh-Taylor instability in soft solids. *Extreme Mechanics Letters*, 40:100940, October 2020. doi:10.1016/j.eml.2020.100940.
- [89] Kecheng Li, Guodong Zhuo, Yinnan Zhang, Congshan Liu, Weiqiu Chen, and Chaofeng Lü. Hypergravitational Rayleigh-Taylor instability in solids. Extreme Mechanics Letters, 55:101809, Aug 2022. doi:10.1016/j.eml.2022.101809.
- [90] B. J. Plohr and D. H. Sharp. Instability of accelerated elastic metal plates. Zeitschrift für angewandte Mathematik und Physik ZAMP, 49(5):786–804, Sep 1998. doi:10.1007/s000330050121.
- [91] S. A. Piriz, A. R. Piriz, and N. A. Tahir. Finite-thickness effects on the Rayleigh-Taylor instability in accelerated elastic solids. *Phys. Rev. E*, 95:053108, May 2017. doi:10.1103/PhysRevE.95.053108.
- [92] S. A. Piriz, A. R. Piriz, and N. A. Tahir. Rayleigh-Taylor instability in accelerated elastic-solid slabs. *Phys. Rev. E*, 96:063115, Dec 2017. doi:10.1103/PhysRevE.96.063115.
- [93] A. R. Piriz, O. D. Cortázar, J. J. López Cela, and N. A. Tahir. The Rayleigh-Taylor instability. American Journal of Physics, 74(12):1095–1098, December 2006. doi: 10.1119/1.2358158.
- [94] Daniel R. Darby, Zhuoyun Cai, Christopher R. Mason, and Jonathan T. Pham. Modulus and adhesion of Sylgard 184, Solaris, and Ecoflex 00-30 silicone elastomers with varied mixing ratios. *Journal of Applied Polymer Science*, 139(25):e52412, 2022. doi:10.1002/app.52412.

[95] Michio Nishida. Chapter 4.1 - Shock Tubes. In Gabi Ben-Dor, Ozer Igra, and Tov Eelperin, editors, *Handbook of Shock Waves*, pages 553–585. Academic Press, Burlington, 2001. doi:10.1016/B978-012086430-0/50012-9.

- [96] Andrew J. Higgins. A comparison of distributed injection hypervelocity accelerators. In 33rd Joint Propulsion Conference and Exhibit. AIAA, July 1997. doi:10.2514/6. 1997-2897.
- [97] Smooth-On Inc. Ecoflex[™] 00-30. Available at https://www.smooth-on.com/products/ecoflex-00-30/ (2023/11/10).
- [98] O. T. Strand, D. R. Goosman, C. Martinez, T. L. Whitworth, and W. W. Kuhlow. Compact system for high-speed velocimetry using heterodyne techniques. *Review of Scientific Instruments*, 77(8):083108, August 2006. doi:10.1063/1.2336749.
- [99] Michalis N. Zervas and Christophe A. Codemard. High power fiber lasers: A review. IEEE Journal of Selected Topics in Quantum Electronics, 20(5):219–241, April 2014. doi:10.1109/JSTQE.2014.2321279.
- [100] D. H. Dolan and T. Ao. SIRHEN: a data reduction program for photonic Doppler velocimetry measurements. Technical Report SAND2010-3628, Sandia National Laboratories (SNL), Albuquerque, NM, and Livermore, CA (United States), June 2010. doi:10.2172/989357.
- [101] D. H. Dolan. Extreme measurements with Photonic Doppler Velocimetry (PDV). Review of Scientific Instruments, 91(5):051501, 05 2020. doi:10.1063/5.0004363.
- [102] O. T. Strand. Handbook for the Photonic Doppler Velocimeter, second edition. Technical Report DOE/NV/03624-0820, Nevada National Security Site/Mission Support and Test Services LLC; Las Vegas, NV (United States), July 2020. URL: https://www.osti.gov/biblio/1722894.
- [103] Dan-Cornelius Savu and Andrew J. Higgins. Structural stability of a lightsail for laser-driven interstellar flight. *Acta Astronautica*, 201:376–393, 2022. doi:10.1016/j.actaastro.2022.09.003.

[104] Serge Mora and Franck Richard. Buckling of a compliant hollow cylinder attached to a rotating rigid shaft. *International Journal of Solids and Structures*, 167:142–155, 2019. doi:10.1016/j.ijsolstr.2019.03.010.

- [105] D. H. Dolan, Sandia National Laboratory. Private communication, June 2023.
- [106] Khalil Khanafer, Ambroise Duprey, Marty Schlicht, and Ramon Berguer. Effects of strain rate, mixing ratio, and stress–strain definition on the mechanical behavior of the polydimethylsiloxane (PDMS) material as related to its biological applications. *Biomedical Microdevices*, 11(2):503–508, Apr 2009. doi:10.1007/s10544-008-9256-6.

Appendix A

Derivation of Key Theoretical Expressions

This appendix contains derivations of important theoretical results. The first section provides a brief derivation of the dispersion relation of RTI in an elastic solid with a free surface. The second section derives the shock tube relations used throughout this thesis.

A.1 Derivation of the Dispersion Relation for RTI in an Elastic Solid

What follows is a brief derivation of the dispersion relation relating the linear perturbation growth rate to the properties of an isothermal, isotropic, elastic, that is, Hookean solid. The derivation here presented is a shortening and paraphrasing of the derivation presented by Piriz and Piriz in the second section of Ref. [92]. A similar derivation is also presented in the appendix section of an earlier paper by the same authors [91]. Plohr and Sharp also performed a similar derivation for the particular case of a unitary Atwood number using a slightly different Laplace Transform method [90].

Consider an elastic solid of finite thickness h, shear modulus G, and material density ρ_2 surrounded by a fluid of relatively lighter density $\rho_1 < \rho_2$ on one side and by vacuum, $\rho_3 = 0$, on its other side. Referring once more to Fig. 1.2, the elastic solid initially occupies the region $-h \le y \le 0$ prior to its perturbation. The acceleration ultimately driving the RT instability, g, can be viewed as either gravity acting downwards on a system where the

solid rests atop the fluid (Fig. 1.2a) or it can be viewed as arising from the lighter fluid accelerating the elastic solid (Fig. 1.2b). Both views are equivalent with the latter being the one most explicitly experimentally studied in this thesis. The momentum and continuity equations for either systems are, respectively,

$$\rho \frac{\mathrm{d}\mathbf{v}}{\mathrm{d}t} = -\nabla p + \rho \mathbf{g} + \nabla \cdot \overleftarrow{\boldsymbol{\sigma}}', \text{ and}$$
(A.1)

$$\frac{\mathrm{d}\rho}{\mathrm{d}t} + \rho \nabla \cdot \mathbf{v} = 0,\tag{A.2}$$

with \mathbf{v} , ρ , and p being the continuum velocity, density, and pressure. The acceleration is directed along the y-axis, $\mathbf{g} = g\hat{\mathbf{e}}_y$. Further, $\overrightarrow{\boldsymbol{\sigma}}'$ stands for the deviatoric part of the stress tensor $\sigma_{ik} = -p\delta_{ik} + \sigma'_{ik}$ where δ_{ik} is the Kronecker delta and index notation is used to express the tensors in a Cartesian setting such that the indices i=1,2,3 label, respectively, the spatial coordinates x,y,z. Vector and tensor notation will be used interchangeably throughout this chapter based on which notation is deemed most appropriate for presentation. The deviatoric part of the stress tensor for a Hookean solid is

$$\frac{\partial \sigma'_{ik}}{\partial t} = G\left(\frac{\partial v_i}{\partial x_k} + \frac{\partial v_k}{\partial x_i}\right). \tag{A.3}$$

Examining only the linear RTI problem, the above governing equations are linearized using a first-order perturbation approach where the all of the variables of interest $N(\mathbf{v}, \rho, p, \overleftarrow{\boldsymbol{\sigma}}')$ are displaced from their equilibrium position N_0 by a small amount δN such that $N = N_0 + \delta N$. Assuming incompressibility ($\delta \rho = 0$), from this perturbation expansion, Eqs. (A.1)-(A.3) become

$$\rho_2 \frac{\partial (\delta \mathbf{v}_2)}{\partial t} = -\nabla (p_2 + \rho_2 \delta \varphi_2) + \nabla \cdot \stackrel{\longleftrightarrow}{\mathbf{S}}$$
(A.4)

$$\nabla \cdot (\delta \mathbf{v}_2) = 0 \tag{A.5}$$

where the subindex 2 denotes the physical quantities of the elastic solid and \overrightarrow{S} denotes the deviatoric perturbation ($S_{ik} \equiv \delta \sigma'_{ik}$).

To circumvent the vectorial nature of the problem, the perturbed velocity field is expressed in terms of scalar functions using Helmholtz decomposition, writing the velocity as

a sum of an irrotational and rotational part:

$$\delta \mathbf{v}_2 = \boldsymbol{\nabla} \phi_2 + \boldsymbol{\nabla} \times (\psi_2 \hat{\mathbf{e}}_z) \tag{A.6}$$

Substituting the above Eq. (A.6) into Eq. (A.5) yields the Laplace equation

$$\nabla^2 \phi_2 = 0. \tag{A.7}$$

Substitution of Eq. (A.6) into the linearized momentum equation (Eq. (A.4)) while assuming that the velocity potential functions take the form

$$\phi_2 \propto e^{(\gamma t + qy)} \sin kx, \quad \psi_2 \propto e^{(\gamma t + q'y)} \cos kx$$
 (A.8)

further yields

$$\nabla \left(\gamma \phi_2 + \frac{\delta p_2}{\rho_2} + \delta \varphi_2 \right) + \nabla \times \left[\left(\gamma \psi_2 - \frac{G}{\gamma \rho_2} \nabla^2 \psi_2 \right) \hat{\mathbf{e}}_z \right] = 0. \tag{A.9}$$

Using the so-called Bernoulli gauge, it can be shown that, for the LHS of the above equation to equal zero, the terms in parentheses must each equal zero implying that

$$\gamma \phi_2 + \frac{\delta p_2}{\rho_2} + \delta \varphi_2 = 0 \tag{A.10}$$

$$\gamma^2 \psi_2 = \frac{G}{\rho_2} \nabla^2 \psi_2. \tag{A.11}$$

Substituting the assumed form of the velocity potentials displayed by Eq. (A.8) into Eqs. (A.7) and (A.11) one obtains the following equations describing the potentials in terms of the constants of integration a_2 , b_2 , c_2 , and d_2 :

$$\phi_2 = \frac{a_2 \cosh ky + b_2 \cosh k(h+y)}{\sinh kh} e^{\gamma t} \sin kx, \tag{A.12}$$

$$\psi_2 = \frac{c_2 \sinh \lambda y + d_2 \sinh \lambda (h+y)}{\sinh \lambda h} e^{\gamma t} \cos kx, \tag{A.13}$$

A similar procedure can be employed to obtain an expression for the perturbed velocity in the lighter fluid medium $(y \ge 0)$:

$$\phi_1 = a_1 e^{-ky} e^{\gamma t} \sin kx, \quad \delta v_{1y} = \frac{\partial \phi_1}{\partial y}, \quad \delta v_{1x} = \frac{\partial \phi_1}{\partial x}$$
 (A.14)

where the subscript 1 indicates physical quantities of the fluid.

The dispersion relation can be obtained by solving for the constants a_1 , a_2 , b_2 , c_2 , and d_2 using the boundary conditions on the surfaces y = 0 and y = -h.

Imposing continuity of the normal velocity at the y=0 interface yields

$$a_1 = -(b_2 + d_2). (A.15)$$

Imposing continuity of the tangential stress S_{xy} at the y = 0 and y = -h interfaces further yields

$$d_2 = -\frac{2k^2}{\lambda^2 + k^2}b_2, \quad c_2 = -\frac{2k^2}{\lambda^2 + k^2}a_2. \tag{A.16}$$

From the continuity of the normal stress, $-\delta p + S_{yy} = -\delta p + (G/\gamma)\partial(\delta v_y)/\partial y$, the following equation is obtained at y = 0

$$\gamma \left(b_2 \coth kh + \frac{a_2}{\sinh kh} \right) + \frac{2kG}{\gamma \rho_2} \left[k \left(b_2 \coth kh + \frac{a_2}{\sinh kh} \right) + \lambda \left(d_2 \coth \lambda h + \frac{c_2}{\sinh \lambda h} \right) \right] - \frac{kg}{\gamma} (b_2 + d_2)$$

$$= \frac{\rho_1}{\rho_2} \left(\gamma + \frac{kg}{\gamma} \right) a_1.$$
(A.17)

and at y = -h

$$\gamma \left(a_2 \coth kh + \frac{b_2}{\sinh kh} \right) + \frac{2kG}{\gamma \rho_2} \left[k \left(a_2 \coth kh + \frac{b_2}{\sinh kh} \right) + \lambda \left(c_2 \coth \lambda h + \frac{d_2}{\sinh \lambda h} \right) \right] + \frac{kg}{\gamma} (a_2 + c_2) = 0.$$
(A.18)

Equations (A.15) to (A.18) can be rewritten as the following system of equations:

$$a_2(C+B) + b_2 A = 0, (A.19)$$

$$a_2 A + b_2 \left[C - B + \frac{\rho_1}{\rho_2} \left(B + \frac{\gamma^2 \rho_2}{G} \right) \right] = 0,$$
 (A.20)

where the constants A, B, and C are

$$A = \frac{(\lambda^2 + k^2)^2 \operatorname{csch} kh - 4k^3 \lambda \operatorname{csch} \lambda h}{\lambda^2 - k^2},$$
(A.21)

$$B = \rho_2 kg/G, \tag{A.22}$$

$$C = \frac{(\lambda^2 + k^2)^2 \coth kh - 4k^3 \lambda \coth \lambda h}{\lambda^2 - k^2}.$$
 (A.23)

Using the fact the determinant of this system must equal zero, the dispersion relation may finally be obtained:

$$C^{2} - A^{2} = B^{2} - \frac{\rho_{1}}{\rho_{2}}(C+B)\left(B + \frac{\gamma^{2}\rho_{2}}{G}\right). \tag{A.24}$$

Substituting in the expressions for A, B, and C in the above Eq. (A.24) while taking the Atwood number equal to unity (i.e., while letting At = 1 which also lets $\rho_2 = \rho$), the dispersion relation becomes Eq. (2.2):

$$\left(\frac{G}{\rho g}\right)^{8} \left\{ \left(\frac{8\pi^{2}}{\lambda^{2}} + \frac{\rho \gamma^{2}}{G}\right)^{4} + \frac{1024\pi^{6}}{\lambda^{6}} \left(\frac{4\pi^{2}}{\lambda^{2}} + \frac{\rho \gamma^{2}}{G}\right) - \left(\frac{4\pi}{\lambda}\right)^{3} \sqrt{\frac{4\pi^{2}}{\lambda^{2}} + \frac{\rho \gamma^{2}}{G}} \left(\frac{8\pi^{2}}{\lambda^{2}} + \frac{\rho \gamma^{2}}{G}\right)^{2} \left[\coth\left(\frac{2\pi h}{\lambda}\right) \coth\left(\sqrt{\frac{4\pi^{2}}{\lambda^{2}} + \frac{\rho \gamma^{2}}{G}}h\right) - \operatorname{csch}\left(\frac{2\pi h}{\lambda}\right) \operatorname{csch}\left(\sqrt{\frac{4\pi^{2}}{\lambda^{2}} + \frac{\rho \gamma^{2}}{G}}h\right) \right] \right\} - \left(\frac{2\pi G^{2} \gamma^{2}}{\lambda \rho^{2} g^{3}}\right)^{2} = 0.$$

A.2 Derivation of the Relevant Shock Tube Relations

The following section offers a more thorough introduction to the working principles of a shock tube of uniform cross-section. Below is a summary of the more detailed derivations found in Chapter 4.1 of the *Handbook of Shock Waves* by Nishida [95] with a focus on the relationship between the static pressures observed in the regions created by the propagation of a shock wave in a shock tube.

A.2.1 The Shock Jump Relations

As its name implies, a shock tube is a device used to generate a shock wave in a laboratory setting. To appreciate the gasdynamics of such a device, the dynamics of a shock wave must thus first be understood. Consider a gas flowing supersonically at speed u_1 with initial pressure p_1 , initial density ρ_1 , and initial temperature T_1 encountering a normal shock wave (Fig. A.1). Upon encountering the shock wave, the properties of the gas flow undergo a sudden jump or discontinuity to the new values of u_2 , p_2 , ρ_2 , and T_2 .

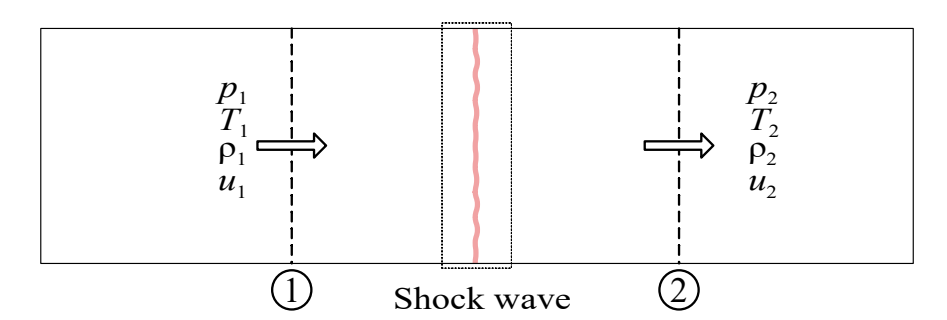


Figure A.1: Schematic of a normal shock wave.

To relate the new state of the gas to its initial state prior to encountering the discontinuity, the fundamental conservation equations of 1D steady-state, inviscid flow are employed. In such a scenario, the conservation of mass and momentum equations, respectively, read

$$\rho_1 u_1 = \rho_2 u_2, \tag{A.25}$$

$$\rho_1 u_1^2 + p_1 = \rho_2 u_2^2 + p_2. \tag{A.26}$$

Assuming throughout the remainder of this thesis that the gases of interest are calorically perfect (i.e., ideal gases whose specific heats do not depend on temperature), the conservation of energy equation reads as

$$c_p T_1 + \frac{u_1^2}{2} = c_p T_1 + \frac{u_1^2}{2}. (A.27)$$

with c_p being the specific heat at constant pressure of the gas. Combining the mass (A.25) and the energy (A.27) conservation equations, the ratio of pressures across the shock wave can be written purely in terms of the specific heat ratio of the gas, $\kappa = c_p/c_v$, and of the density ratio across the shock wave:

$$\frac{p_2}{p_1} = \frac{\frac{\kappa + 1}{\kappa - 1} \frac{\rho_2}{\rho_1} - 1}{\frac{\kappa + 1}{\kappa - 1} - \frac{\rho_2}{\rho_1}}.$$
(A.28)

The density ratio can also be isolated in the above equation:

$$\frac{\rho_2}{\rho_1} = \frac{u_1}{u_2} = \frac{1 + \frac{\kappa + 1}{\kappa - 1} \frac{p_2}{p_1}}{\frac{\kappa + 1}{\kappa - 1} + \frac{p_2}{p_1}}.$$
(A.29)

The above two equations can also be expressed in terms of the Mach number of to flow into the shock wave, as viewed from the reference frame of the shock, $M_1 \equiv u_1/c_1$, where c_1 is the speed of sound in the pre-shocked gas:

$$\frac{\rho_2}{\rho_1} = \frac{u_1}{u_2} = \frac{(\kappa + 1)M_1^2}{2 + (\kappa - 1)M_1^2},\tag{A.30}$$

$$\frac{p_2}{p_1} = 1 + \frac{2\kappa}{\kappa + 1} \left(M_1^2 - 1 \right). \tag{A.31}$$

The temperature ratio across the shock wave can also be found directly from the energy equation:

$$\frac{T_2}{T_1} = 1 + \frac{2(\kappa - 1)}{(\kappa + 1)^2} \frac{\kappa M_1^2 + 1}{M_1^2} \left(M_1^2 - 1 \right), \tag{A.32}$$

and the difference between the post-shock and pre-shock flow velocities, $u_2 - u_1$, can be obtained from the momentum equation

$$\frac{u_2 - u_1}{c_1} = \frac{-2}{\kappa + 1} \left(M_1 - \frac{1}{M_1} \right). \tag{A.33}$$

Finally, the above two equations (A.32) and (A.33) can also be expressed only in terms of the specific heat ratio and pressure density ratio as

$$\frac{T_2}{T_1} = \frac{p_2}{p_1} \frac{\zeta + \frac{p_2}{p_1}}{1 + \zeta \frac{p_2}{p_1}},\tag{A.34}$$

and

$$\frac{u_2 - u_1}{c_1} = -\frac{(\zeta - 1)\left(\frac{p_2}{p_1} - 1\right)}{\sqrt{(1 + \zeta)\left(1 + \zeta\frac{p_2}{p_1}\right)}},\tag{A.35}$$

where $\zeta = (\kappa + 1)/(\kappa - 1)$. Equations (A.28), (A.29), (A.34), and (A.35) are often called the Rankine-Hugoniot relations as they relate the post-shock and pre-shock gas states only in terms of thermodynamic variables.

A.2.2 The Shock Tube Relations

With the shock jump relations derived, the gasdynamics of a shock tube can now be analyzed. What follows is a derivation of the shock tube Eqs (2.6)–(2.8) by considering the physical relationships between the various gas regions depicted in Fig. 2.4.

Relations between Regions 1 and 2 The shock jump relations were derived in a reference frame with respect to which the shock was not moving. Considering a shock wave propagating at speed U_{s1} following diaphragm rupture, the shock jump relations can be used in a reference frame moving at the constant speed U_{s1} . From here onward, the relations (A.28)–(A.35) are employed by replacing the pre-shock Mach number, M_1 , by the shock wave Mach number, $M_{s1} \equiv U_{s1}/c_1$. Also, from this coordinate transformation, the new pre- and post-shock flow velocities, u'_1 and u'_2 , respectively, are related to the laboratory reference frame by $u'_1 = -U_{s1}$ and $u'_2 = u_2 - U_{s1} = u_2 - u'_1$ (see Fig. A.2). Consequently, equation (A.30) becomes

$$\frac{\rho_2}{\rho_1} = \frac{u_1'}{u_2'} = \frac{U_{\text{s1}}}{U_{\text{s1}} - u_2} = \frac{(\kappa_1 + 1) M_{\text{s1}}^2}{2 + (\kappa_1 - 1) M_{\text{s1}}^2}.$$
(A.36)

The post-shock velocity in the laboratory-fixed reference frame, u_2 , can be isolated in the above Eq. (A.36) such that

$$u_2 = \frac{2c_1}{\kappa_1 + 1} \left(M_{\rm s1} - \frac{1}{M_{\rm s1}} \right) \tag{A.37}$$

Also, the pressure ratio between the gases in Region 1 and Region 2 is, using Eq. (A.31),

$$\frac{p_2}{p_1} = 1 + \frac{2\kappa_1}{\kappa_1 + 1} \left(M_{\rm s1}^2 - 1 \right).$$
(A.38)

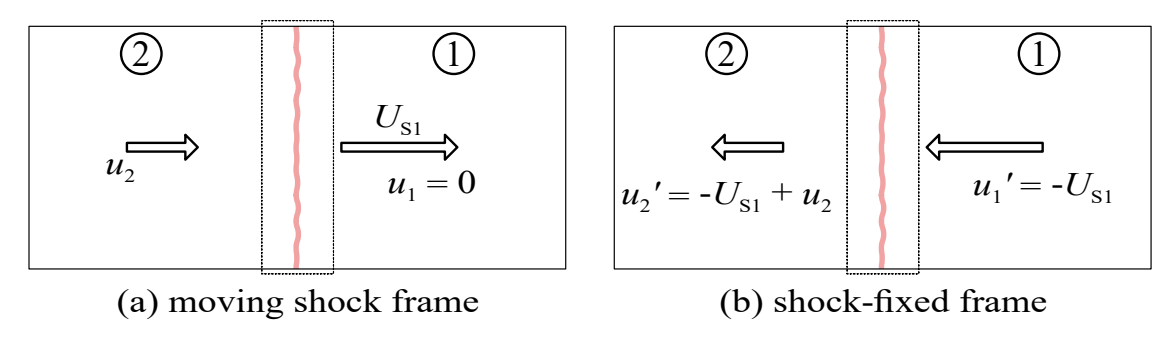


Figure A.2: A normal shock wave in a laboratory-fixed reference frame (a) and in a shock-fixed frame (b).

Relations between Regions 2 and 3 Because Regions 2 and 3 are the regions immediately after and before the contact surface, the velocities and pressures of the gases in these regions must be equal such that

$$u_3 = u_2, \tag{A.39}$$

and

$$p_3 = p_2, \tag{A.40}$$

albeit the densities and temperatures across the contact surface may be different. As a reminder, note that the lack of primes on the velocities u_3 and u_2 indicates that the velocities are measured in a laboratory-fixed frame.

Relations between Regions 3 and 4 Since the expansion of the high-pressure gas from region 4 into region 3 is an isentropic process, the pressures between region 4 and 3 can be

related via an isentropic equation:

$$\frac{p_4}{p_3} = \left(\frac{c_4}{c_3}\right)^{\frac{2\kappa_4}{\kappa_4 - 1}}.$$
 (A.41)

Note that because regions 3 and 4 are occupied by the same substance, it can be assumed that $\kappa_3 = \kappa_4$. The expansion wavefront initiated by the diaphragm rupture first propagates upstream (towards the left in Fig. 2.4) until its component expansion waves are reflected by the shock tube end wall, causing them to propagate downstream. The Riemann invariant along the forward propagating expansion remains constant from region 3 through 4, and so, recalling the expression for the Riemann invariant along a forward moving wavefront while also noting that the gas in region 4 is at rest (i.e., $u_4 = 0$) yields the following equality:

$$\frac{2}{\kappa_4 - 1}c_4 = u_3 + \frac{2}{\kappa_3 - 1}c_3. \tag{A.42}$$

Substituting Eq. (A.42) into Eq. (A.41) to express the ratio p_4/p_3 in terms of κ_4 and u_3 while combining the result with Eqs. (A.37), (A.38), (A.39), and (A.40), one obtains

$$\frac{p_4}{p_1} = \left[1 + \frac{2\kappa_1}{\kappa_1 + 1} \left(M_{\text{s1}}^2 - 1\right)\right] \left[\frac{1}{1 - \frac{\kappa_4 - 1}{\kappa_1 + 1} \frac{c_1}{c_4} \left(M_{\text{s1}} - \frac{1}{M_{\text{s1}}}\right)}\right]^{\frac{2\kappa_4}{\kappa_4 - 1}}, \tag{A.43}$$

the pressure ratio between the gases in region 1 and region 4 expressed only in terms of $M_{\rm s1}$, κ_1 , κ_4 , and c_1/c_4 .

Relations between Regions 1 and 5 Immediately following the shock reflection off the elastic solid surface, the shock wave reverts direction, traveling into the gas in region 2 with a new velocity U_{s2} , while leaving behind a gas at rest in the laboratory-fixed frame such that $u_5 = 0$. Denoting the velocity of the flow in region 2 and region 5 with respect to the reflected shock as u_2'' and u_5'' , respectively, note that $u_5'' - u_2'' = -u_2$ as shown in Fig. A.3.

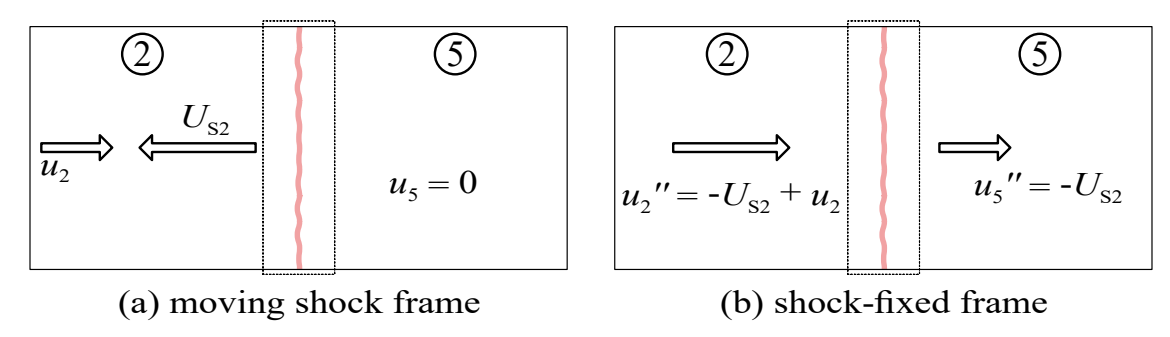


Figure A.3: A reflected shock wave in a laboratory-fixed reference frame (a) and in a shock-fixed frame (b).

Since, recalling the first coordinate transformation from the laboratory frame to a frame moving with the initial shock velocity, U_{s1} , $u'_2 - u'_1 = u_2$, then from Eq. (A.35) one obtains that

$$u_{2} = \frac{\left(\zeta_{1} - 1\right)\left(\frac{p_{5}}{p_{2}} - 1\right)}{\sqrt{\left(1 + \zeta_{1}\right)\left(1 + \zeta_{1}\frac{p_{5}}{p_{2}}\right)}}c_{2} = \frac{\left(\zeta_{1} - 1\right)\left(\frac{p_{2}}{p_{1}} - 1\right)}{\sqrt{\left(1 + \zeta_{1}\right)\left(1 + \zeta_{1}\frac{p_{2}}{p_{1}}\right)}}c_{1},\tag{A.44}$$

where $\zeta_1 = (\kappa_1 + 1)/(\kappa_1 - 1)$. Further, since the regions 1 and 2 are occupied by the same substance, which is treated as an ideal gas, $c_2/c_1 = (T_2/T_1)^{1/2}$ and so Eq. (A.34) yields

$$\frac{c_2}{c_1} = \sqrt{\frac{p_2}{p_1} \frac{\zeta_1 + \frac{p_2}{p_1}}{1 + \zeta_1 \frac{p_2}{p_1}}}.$$
(A.45)

Combining Eq. (A.44) together with Eq. (A.45), an expression for the pressure ratio across regions 2 and 5 can be obtained

$$\frac{p_5}{p_2} = \frac{\frac{p_2}{p_1} \left(\zeta_1 + 2\right) - 1}{\zeta_1 + \frac{p_2}{p_1}}.$$
(A.46)

Substituting in the above the expression for p_2/p_1 from Eq. (A.38) and rearranging terms, the pressure ratio p_5/p_2 may be written in terms of $M_{\rm s1}$ and κ_1 instead as

$$\frac{p_5}{p_2} = \frac{-2(\kappa_1 - 1) + M_{s1}^2(3\kappa_1 - 1)}{2 + M_{s1}^2(\kappa_1 - 1)}.$$
(A.47)

Finally, combining Eqs. (A.38) and (A.47), the pressure ratio between regions 1 and 5 can be expressed as a function of $M_{\rm s1}$ and $\kappa_{\rm 1}$:

$$\frac{p_5}{p_1} = \left[\frac{2\kappa_1 M_{\rm s1}^2 - (\kappa_1 - 1)}{\kappa_1 + 1} \right] \left[\frac{-2(\kappa_1 - 1) + M_{\rm s1}^2(3\kappa_1 - 1)}{2 + M_{\rm s1}^2(\kappa_1 - 1)} \right].$$
(A.48)

Although more relations between the various regions of interest can be derived using the shock jump relations applied in appropriate reference frames, this concludes the catalogue of shock tube theoretical relations that will be used in the main text of this thesis.

Appendix B

Additional Detailing of the Experimental Methods

This appendix contains additional details pertaining to the experimental methods and devices used throughout this thesis.

B.1 Procedure for the Casting of Elastic Solid Samples

After repeated consultation with the Smooth-On technical staff and with the technicians of Sial Canada, and after a considerable number of in-laboratory systematic trial-and-error attempts, a robust, standardized procedure for the casting of the elastic solid samples was obtained. The author is indebted to his laboratory assistant, Léa Bernard, for developing the casting procedure which is described below:

- 1. Prepare the mold by inserting the keys into the male part, ensuring the textured sides faces the exterior. The male part is the block with a base platform on top of which the female part is to sit.
- 2. Carefully join the male and female parts of the mold, making sure the keys are tightly pressed between them to achieve a uniform thickness.
- 3. Clamp the assembled mold securely at the four corners, focusing on the keys rather than the middle to maintain uniformity (clamping the middle will leave the central area of the cast solid thinner than its edges).

- 4. To prevent leakage, seal the crack between the male and female parts of the mold securely by using hot glue. Smooth the glue out with a popsicle stick to make sure there is no leakage. (Note: When working with newly 3D printed molds, it is important to be cautious with using hot glue as it can adhere firmly to the mold and become difficult to remove later. To mitigate this issue, the usage of duct tape to securely fasten the mold during its initial use is recommended. While duct taping might be slightly less efficient compared to hot glue, it offers the advantage of easy removal and saves significant time when trying to detach the mold after the molding process.)
- 5. Set the mold aside for further processing.
- 6. Place a 100 mL weighing dish on a balance and press tare to zero the balance.
- 7. Use a paint stirring stick to stir Part A of the Ecoflex-30 for 20 seconds.
- 8. Remove excess Part A Ecoflex-30 from the stirring stick in the weighing dish using a popsicle stick.
- 9. Pour the required amount of Part A into the weighing dish (e.g., 50 mL for cast of 3 mm thickness).
- 10. If a colored specimen is desired, add about a teaspoon of silicone coloring to Part A and stir the mixture for 2 minutes or until the color is completely incorporated.
- 11. Repeat steps 8 to 10 with a new set of paint stirring stick and popsicle stick for Part B, ensuring the same amount of Part A and Part B is used (the recommended mixing ratio for the curing of Ecoflex 00-30 is 1:1 of Parts A and B).
- 12. Stir the contents of the weighing dish thoroughly with a popsicle stick for 3 minutes.
- 13. Degas the mixture in a vacuum chamber for 4–5 minutes or until the bubbles have significantly reduced and dispersed and are slower.
- 14. Slowly pour the mixture into the mold to minimize bubble production during the pouring process. For thinner specimens, consider slightly opening the mold to allow faster pouring. Pour in the middle in a continuous stream, then reclamp the mold to push excess mixture out for better results. For thicker samples (e.g., 6 mm), pouring speed becomes less critical.

- 15. Ensure the clamps are tight and the keys are positioned flush within their corresponding slot cavities to maintain a consistent thickness throughout the specimen.
- 16. Allow the mold to sit undisturbed for 4 hours before proceeding with the unmolding.
- 17. When it is time to unmold, begin by carefully removing the clamps and any excess silicone on the exterior of the mold.
- 18. Next, if hot glue was used, gently peel it off in a single strip, provided it was applied uniformly. If duct tape was used, slowly and carefully peel off the tape from the mold in order to avoid the tape damaging the plastic material from which the mold is made.
- 19. To separate the mold, use two flat-headed screwdrivers to pry open the top section by gently pushing against the mold walls adjacent to the keys. Be cautious during this step to avoid damaging the mold or the keys.
- 20. To cut the specimen, carefully use a scalpel. For the sides with the keys, make a straight cut against the keys and then gently remove the keys. For the two remaining sides, use one of the keys as a ruler to guide the scalpel and make precise straight cuts.

Although not necessary, the use of protective equipment including vinyl gloves and a lab coat is recommended as the casting process can be messy and the stains are not always easy to remove from garments. The use of latex or nitrile gloves should be avoided as these materials may inhibit the curing process if they come in contact with the silicone elastomer. In a similar vein, using aluminum foils to cover workbench surfaces and the walls of the vacuum chamber helps make accidental spills easier to clean.

B.2 The PDV Heterodyne Principle

A photonic doppler velocimeter uses the interference of two optical signals of different frequency to measure the velocity of a target surface. This is achieved in practice by transporting light from a laser to a probe using optical fibers. The probe then focuses the laser light onto the surface of the moving target of interest. Because the target is moving with respect to the probe, the reflected light that the probe captures has a Doppler shifted frequency, f_d , that is different from the original, reference laser light frequency, f_0 . The two signals are

then mixed together (the so-called heterodyning of the signals) and their superposition is finally sent to a photodetector. Figure B.1 shows a high-level depiction of the process.

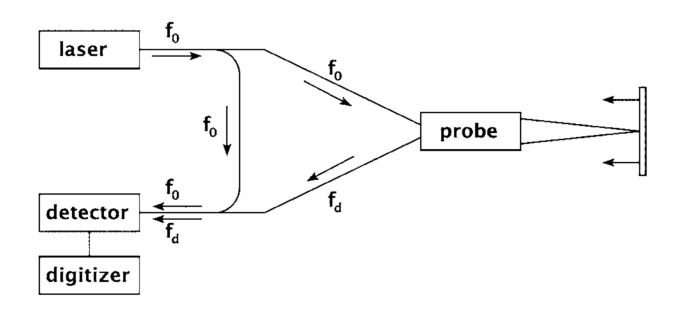


Figure B.1: The basic PDV heterodyne principle. Image taken from [98] with permission.

The Doppler shifting of the original laser signal by the target occurs in a two-step process. First, the probe acts as a source of light having the reference frequency f_0 while the target surface acts as a receiver. Because the target surface is moving with respect to the probe, the moving target encounters a Doppler-shifted light with frequency f_t in accordance to the Doppler formula¹:

$$f_{\rm t} = \frac{c^* + v_{\rm t}}{c^*} f_0 \tag{B.1}$$

where v_t is the velocity of the moving target (positive if the target is moving towards the probe and negative if the target is moving away from the probe). The moving target then partially reflects the f_t frequency light, acting as the second source of light and thereby initiating a second Doppler shifting process. The probe now acts as a receiver and the final frequency that it captures, f_d , is the Doppler-shifted frequency of the target emitted (reflected, really) light, f_t :

$$f_{\rm d} = \frac{c^*}{c^* - v_{\rm t}} f_{\rm t}.$$
 (B.2)

The reference and Doppler-shifted frequencies are on the order of 10^{14} Hz for reference signals in the C-band, and photodetectors and digitizers typically cannot measure such high frequencies. The so-called beat frequency, $f_{\rm b}$, arising from the mixing (heterodyning) of the reference and Doppler-shifted signals, is on the order of a few GHz which can be measured.

Note that, given how small the $\frac{v_t^2}{c^{*2}}$ term is in shock physics experiments, the relativistic time dilation contribution to the Doppler effect, $\sqrt{\frac{1}{1-\frac{v_t^2}{c^{*2}}}}$, is ignored throughout this thesis.

The beat frequency is the absolute difference between reference frequency and the (twice) Doppler-shifted signal frequency, that is, $f_b \equiv |f_d - f_0|$. Expanding this absolute value using Eqs. (B.1) and (B.2) allows for the beat frequency to be explicitly related to the moving target velocity:

$$f_{b} \equiv |f_{d} - f_{0}| = \left| \frac{c^{*} + v_{t}}{c^{*} - v_{t}} - 1 \right| f_{0}$$

$$\therefore f_{b} = 2 \left| \frac{v_{t}}{c^{*} - v_{t}} \right| f_{0} \approx \frac{2}{c^{*}} |v_{t}| f_{0}, \tag{B.3}$$

where the denominator of Eq. (B.3) was simplified by noting that $V_t \ll c^*$ in shock physics experiments. The presence of the absolute value operator in Eq. (B.3) means that the beat frequency measurement is insensitive to direction and cannot tell whether the target is moving towards or away from the probe—although certain unconventional PDV configurations can be made sensitive to the moving target direction.

The beat frequency is responsible for the modulation of the light intensity signal captured by the photodetector. To see how this modulation arises, first recall that the intensity of an electromagnetic wave is proportional to the amplitude of the electric field squared, that is, $I \propto |E|^2$. As is often done in the literature, the remainder of this thesis will assume that the amplitudes of its electric fields being studied are normalized such that $I = |E|^2$. The photodetector captures a light signal made up of the superposition of two signals, the reference signal and the Doppler-shifted signal. Assuming the two signals to be linearly polarized and propagating in the x-direction, that is, assuming $\mathbf{E_0} = (0, 0, E_0)$ and $\mathbf{E_d} = (0, 0, E_d)$, then the two signals may be expressed as

$$E_0 = E_{00}(t) e^{i(\omega_0 t - k_0 x + \delta_0)} = E_{00}(t) e^{i\phi_0}, \quad E_d = E_{0d}(t) e^{i(\omega_d t - k_d x + \delta_d)} = E_{0d}(t) e^{i\phi_d}, \quad (B.4)$$

where ω_i , k_i , and δ_i are the angular frequency, angular wavenumber, and phase constant of their corresponding light signal, respectively. The total intensity of the superposition of the two signals then is²

$$I_{\text{tot}} = |E_{\text{d}} + E_{0}|^{2} = \left(E_{0\text{d}}(t) e^{i\phi_{\text{d}}} + E_{00}(t) e^{i\phi_{0}}\right) \overline{\left(E_{0\text{d}}(t) e^{i\phi_{\text{d}}} + E_{00}(t) e^{i\phi_{0}}\right)}$$

²The $\overline{(\bullet)}$ symbol denotes the complex conjugate operator.

$$\implies I_{\text{tot}} = E_{00}^2 + E_{0d}^2 + 2E_{00}E_{0d}\cos(\phi_d - \phi_0)$$

$$\therefore I_{\text{tot}} = I_0(t) + I_d(t) + 2\sqrt{I_0I_d}\cos\left(\frac{f_b}{2\pi}t + \phi\right). \tag{B.5}$$

The interference term $2\sqrt{I_0I_d}\cos\left(\frac{f_b}{2\pi}t + \phi\right)$ is the predominant reason for the variation of the signal intensity. The additional phase of the beat waveform, $\phi = (k_0 - k_d)x + (\delta_d - \delta_0)$, does not vary much during a shock experiment by comparison to the beat frequency term, and so the time variation of the intensity signal is driven by the variation of the beat frequency with target velocity as described in Eq. (B.3).

Table B.1 computes the beat frequency for various target velocities using two different reference laser wavelengths with the first wavelength set to $\lambda_{\rm red} = 750\,\rm nm$ (visible red laser) and the second wavelength set to $\lambda_{\rm IR} = 1550\,\rm nm$ (standard C-band wavelength). Beyond the low attenuation of silica fibers at the 1550 nm wavelength, setting the laser wavelength in the C-band offers an additional advantage in the case of photon Doppler velocimetry: the larger reference wavelength translates into a lower beat frequency for a given target velocity thereby increasing the maximum possible target velocity for a given PDV system bandwidth.

Table B.1: Target velocities and beat frequencies for different reference laser wavelengths.

Target Velocity [m/s]	Visible Red Laser [750 nm]	IR Laser [1550 nm]
1	$f_{ m b}=2.7{ m MHz}$	$f_{\rm b}=1.3{\rm MHz}$
100	$f_{ m b}=270{ m MHz}$	$f_{\rm b}=130{\rm MHz}$
1000	$f_{ m b}=2.7{ m GHz}$	$f_{\rm b}=1.3{\rm GHz}$
5000	$f_{\rm b}=13{\rm GHz}$	$f_{\rm b}=6.5{\rm GHz}$

B.3 The Detailed Schematic of the PDV Box

Figure B.2 below displays a detailed labeling of components contained in the PDV box.

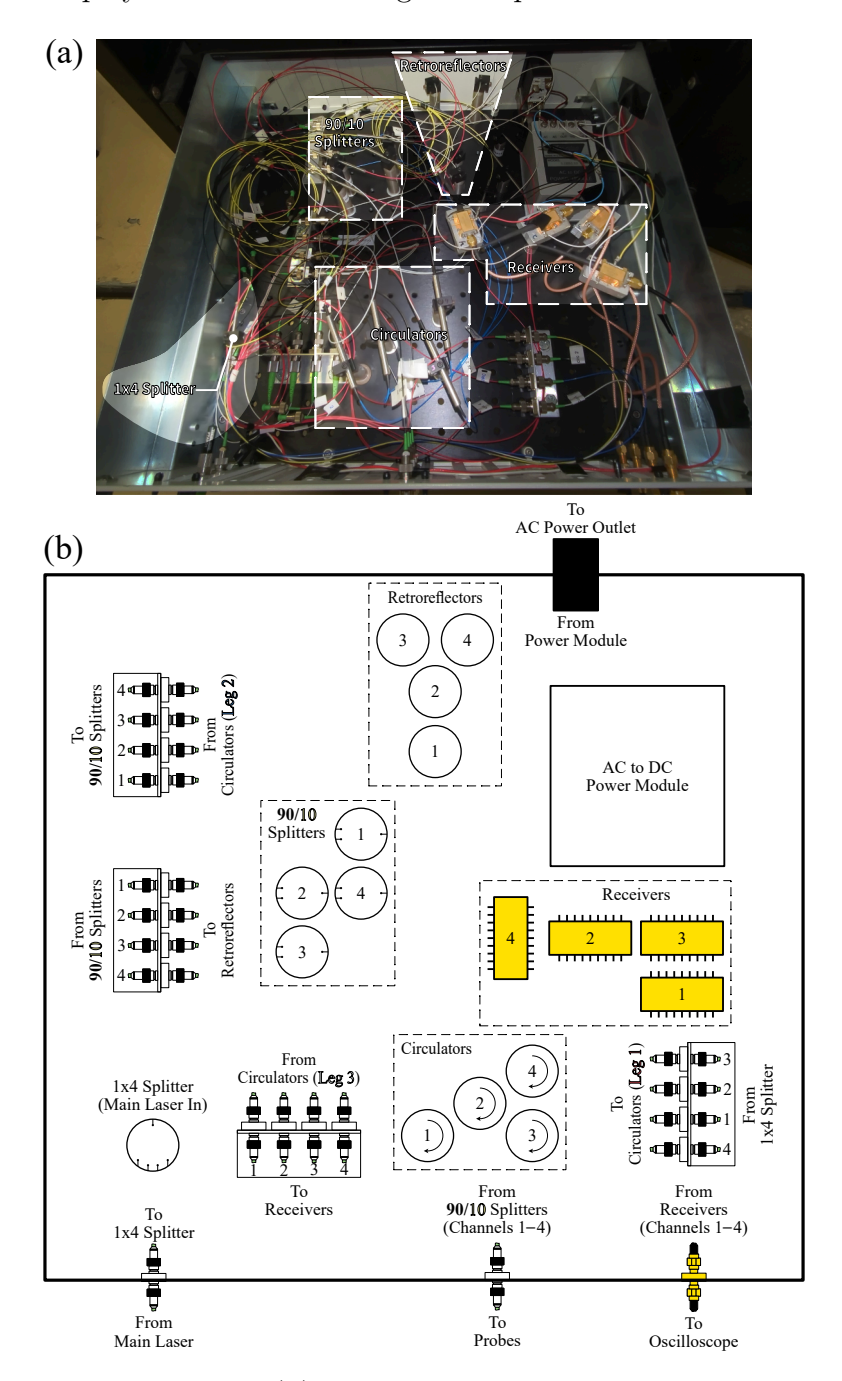


Figure B.2: A detailed schematic (b) of the layout of the photonic components found within the McGill PDV box (a).